Ph.D. Dissertation

Systematic Design of Antioxidant Hybrid Biocatalysts Based on Inorganic Nanozymes and Polystyrene Latex Beads

Nizar B. Alsharif

SUPERVISOR

Dr. István Szilágyi

Associate Professor

Doctoral School of Chemistry

MTA-SZTE „Lendület” Biocolloids Research Group

Department of Physical Chemistry & Materials Science

University of Szeged

Szeged

2022

Table of Contents

List of Abbreviations

Abbreviation	Definition
MOFs	Metal-organic frameworks
CAT	Catalase
SOD	Superoxide dismutase
HRP	Horseradish peroxidase
PZC	Point of zero charge
IEP	Isoelectric point
ROS	Reactive oxygen species
ATP	Adenosine triphosphate
DNA	Deoxyribonucleic acid
NADPH	Nicotinamide adenine dinucleotide phosphate
RNA	Ribonucleic acid
v_{max}	Maximum possible reaction rate
K_{m}	Michaelis constant
vdW	van der Waals forces
EDL	Electrical double layer
OHP	Outer Helmholtz plane
PBE	Poisson–Boltzmann equation
DH	Debye-Hückel
DLVO	Derjaguin, Landau, Verwey, and Overbeek
CCC	Critical coagulation concentration
$\mathrm{T}_{1/2}$	Aggregation half-time
W	Stability ratio
DLS	Dynamic light scattering
ELS	Electrophoretic light scattering
R_{h}	Hydrodynamic radius
k_{app}	Apparent aggregation rate constant
AL	Amidine-functionalized polystyrene latex
SL	Sulfate-functionalized polystyrene latex

DPPH	2,2-diphenyl-1-picrylhydrazyl
PDADMAC	Poly(diallyldimethylammonium chloride)
TMB	3,3',5,5'-Tetramethylbenzidine
TRIS	Tris(hydroxymethyl)aminomethane
NBT	Nitro blue tetrazolium chloride
XPS	X-ray photoelectron spectroscopy
XRD	X-ray diffraction
JCPDS	Joint committee on powder diffraction standards
SEM	Scanning electron microscopy
TEM	Transmission electron microscopy
AFM	Atomic force microscopy
PB NPs	Prussian blue nanoparticles
MnO_2 MFs	Manganese (IV) oxide microflakes
CeO_2 NPs	Cerium (IV) oxide nanoparticles
PVP	Poly(vinylpyrrolidone)
PMn	PDADMAC-functionalized MnO_2 MFs
PCe	PDADMAC-functionalized CeO_2 NPs
AL-PB	Amidine-functionalized polystyrene latex-Prussian blue
SPMn	SL-(PDADMAC-MnO_2 MFs)
SPCe	SL-(PDADMAC-CeO_2 NPs)
I	Inhibition
IC_{50}	Half maximal inhibitory concentration
DMSO	Dimethyl sulfoxide
ε	Molar extinction coefficient
DPPH%	Proportion of unreacted DPPH
EC_{50}	Effective concentration
HR-TEM	High-resolution TEM
FFT	Fast Fourier transform
PDI	Polydispersity index
ASP	Adsorption saturation plateau

List of Figures

potential at the slipping plane is the electrokinetic or zeta (ζ) potential.

Figure 10. The total interaction potential (V_T) or the DLVO force profile as a function of the separation distance. The magnitude of V_T depends on the sum of the repulsive EDL and the attractive vdW forces. The dashed line refers to short-ranged non-DLVO repulsion, known as “Born repulsion”.

Figure 11. (a) The various phases of the aggregation process. The early-stage aggregation statistically involves the formation of dimers and mostly occurs in diluted systems. The late-stage aggregation, on the other hand, involves the formation of higher-rank aggregates and occurs in concentrated systems. At given pH and ionic strength, the change in the particle size over time is used to probe the different aggregation phases at various particle concentrations. (b) In the early-stage aggregation, the aggregation rate is affected by the salt level in the system. At low salt levels, the system is stable or very slowly dimerizes (slow aggregation regime), while at high salt levels, the dimer formation proceeds rapidly (rapid aggregation regime). The system transitions between the two regimes at a characteristic salt concentration, called the critical coagulation concentration (CCC).

Figure 12. A Schematic illustration of heteroaggregation of particles of various sizes and shapes, where the aggregation of different particles is initiated by careful manipulation of the experimental conditions, and thus, the variation of the interparticle forces.

Figure 13. The SOD assay for the determination of the SOD-like activity. The $\bullet O_2^-$, generated via the oxidation of xanthine to uric acid by xanthine oxidase, can reduce the yellow NBT into a purple product, called formazan, which possesses a characteristic absorption peak at 565 nm. The SOD enzyme, nevertheless, effectively converts $\bullet O_2^-$ to H_2O_2, which leaves the NBT unchanged or partially reduced, resulting in the inhibition of the radical-NBT reaction. The extent of inhibition is studied via the UV-Vis spectrophotometry by probing the emergence of the formazan absorption peak at 565 nm over time. The inhibition curve of the radical-NBT is constructed as a function of nanozyme concentration using equation (39).

Figure 14. The TMB assay for the HRP-like activity. The colorless TMB is oxidized in the presence of H_2O_2 and HRP (or its mimetic nanozyme). The oxidized TMB, in the form of a diamine/diimine complex, is characterized by a blue color as well as a strong absorption peak at 652 nm. The increase in the absorbance of the blue complex over time at 652 nm is probed via the UV-Vis spectrophotometry. The molar absorption coefficient, ε, of oxidized TMB is 39.0 mM^{-1} cm^{-1}.

Figure 15. The Guaiacol assay for the determination of the HRP-like activity. In the presence of HRP-mimicking nanozymes and H_2O_2, the colorless guaiacol is oxidized to a brown product, called tetraguaiacol which is characterized by a strong absorption peak at 470 nm. The UV-Vis spectrophotometry is utilized to probe the emergence of such an absorption peak over time. The ε of tetraguaiacol is 26.6 mM^{-1} cm^{-1}.

Figure 16. The catalase assay for the determination of the CAT-like activity. The CAT enzyme breaks down H_2O_2 into water and O_2. The H_2O_2 has an absorption peak at 240 nm. By monitoring the decrease in absorbance of H_2O_2 at 240 nm over time, the CAT-like activity can be assessed. The ε of H_2O_2 is 39.4 M^{-1} cm^{-1}.

Figure 17. The DPPH assay for the assessment of the antioxidant potential. The deep violet DPPH radical has a strong absorption peak at 517 nm. The reduced DPPH, however, has no such absorption peak. The disappearance of such peak over time in the presence of some material is a measure of the antioxidant potential of the material.

Figure 18. (a) UV-Vis absorption spectrum of PB NPs at pH 4, the TEM image of PB NPs is

List of Tables

1 Introduction

Antioxidant enzymes have numerous key functions within living systems including cell protection against oxidative stress. The highly intricate chemical structure of the comprising proteins brings about unparalleled catalytic potential, specificity, and selectivity. These attributes have led to wide use in numerous fields such as pharmaceuticals, cosmetics, and the food industry. Yet, the applicability of these biocatalysts is often hindered due to several inherent flaws that are detrimental to their catalytic potential. For instance, enzymes suffer from extreme sensitivity to such conditions in their microenvironment as pH, temperature, solvent, and the presence of inhibitors. Undesignated conditions, therefore, lead to irreversible structural alternations and subsequent permanent loss of catalytic activity. Thus, the extraction and purification processes of enzymes are highly complex and time-consuming rendering them particularly expensive materials.

These drawbacks have unavoidably given rise to an ever-growing demand for versatile enzyme alternatives with indistinguishable antioxidant potential. Among the earliest reported artificial enzymes were to include cyclodextrins, coordination compounds, and polymeric substances. However, the discovery of the enzyme mimicry of nanostructures, also called nanozymes, presented a promising alternative to antioxidant enzymes since the biocatalytic potential is expected to be maintained at pH and temperature conditions, where the mimicked enzymes are inactivated. In addition, nanomaterials have highly tunable physicochemical properties as well as scalable, straightforward, and low-cost production processes. These advantages have led to the discovery of numerous nanozymes with highly varying structures and compositions including (bi)metallic particles, nanostructured carbon materials, metal oxides/chalcogenides, and metal-organic frameworks (MOFs). Such materials were proven to possess the mimetic potential of several essential antioxidant enzymes including catalase (CAT), superoxide dismutase (SOD), and horseradish peroxidase (HRP) that play pivotal roles in living systems and are widely used in many industrial fields.

However, due to the tendency to minimize the high surface Gibb’s energy, numerous nanostructured materials are prone to aggregation when introduced into fluid media, and the extent of aggregations is often maximized under certain conditions including solvents of different polarity, high ionic strength, a characteristic point of zero charge (PZC) or an isoelectric point (IEP), and presence of surfactants or polyelectrolytes. Moreover, particle aggregation is expected to adversely affect the catalytic potential since the catalytic action takes place on the particle surface. Therefore, the prevention of particle aggregation is a vital step for the efficient use of nanomaterials as effective artificial enzymes. One of the common approaches to prevent particle aggregation is the immobilization of the catalytic nanoparticles onto larger support materials such as clays, graphene oxide, and latex particles. The formulation of such support-nanozyme composite prevents aggregation of nanozymes, enables separation of the composites after the catalytic cycle, and preserves the particles' large surface area; hence, preserves their biocatalytic potential. These composites are, therefore, expected to be robust antioxidants with superb enzyme-like catalytic potential as well as sustained catalytic surface, and thus, are foreseen to be highly beneficial in industries involving the mimicked enzymes.

In the work pertaining to this dissertation, potential nanozymes including organometallics (Prussian blue) and metal oxides (MnO_2 and CeO_2) were synthesized as potential nanozymes and were further formulated into composites under controlled heteroaggregation with polystyrene latex beads. Prior to heteroaggregation, the surface and colloid properties of both the nanozymes and the latex were carefully examined under various experimental conditions and the formulation of the composites was carried out under the optimal conditions to maximize the interaction between the nanozyme and the latex, and hence, obtain latex-nanozyme composite with high structural and functional stability.

2 Literature Review

2.1 Oxidative stress

The oxidative stress phenomenon is the state of serious imbalance between the production of reactive oxygen species (ROS) and the ability of biological systems to restore proper ROS levels resulting in their accumulation in cells and tissues. ROS include various radical, neutral, and ionic oxygen species such as hydroxyl radical ($\bullet OH$), peroxyl radical ($\bullet O_2R$), superoxide ($\bullet O_2^-$), alkoxyl radical ($\bullet OR$), hydrogen peroxide (H_2O_2), singlet oxygen ($^1O_2$), ozone (O_3), hypochlorous acid (HOCl), and organic peroxides (ROOR’).[1, 2]

These highly active species are mostly acquired through aerobic metabolic pathways that exclusively or collaterally result in ROS production. In mitochondria, for instance, $\bullet O_2^-$ is generated as a by-product during the ATP production process, where O_2 is normally reduced to water through a series of electron transfer processes. However, a small proportion (1-3%) of O_2 molecules acquires an additional electron, resulting in the formation of $\bullet O_2^-$.[2, 3] Similarly, cytochrome P450 enzymes, a family of heme monooxygenases located in liver cells, have vital roles in the biotransformation of drugs such as acetaminophen; uncoupling of their enzymatic cycle leads to the formation of ROS including $\bullet O_2^-$ and H_2O_2.[4]

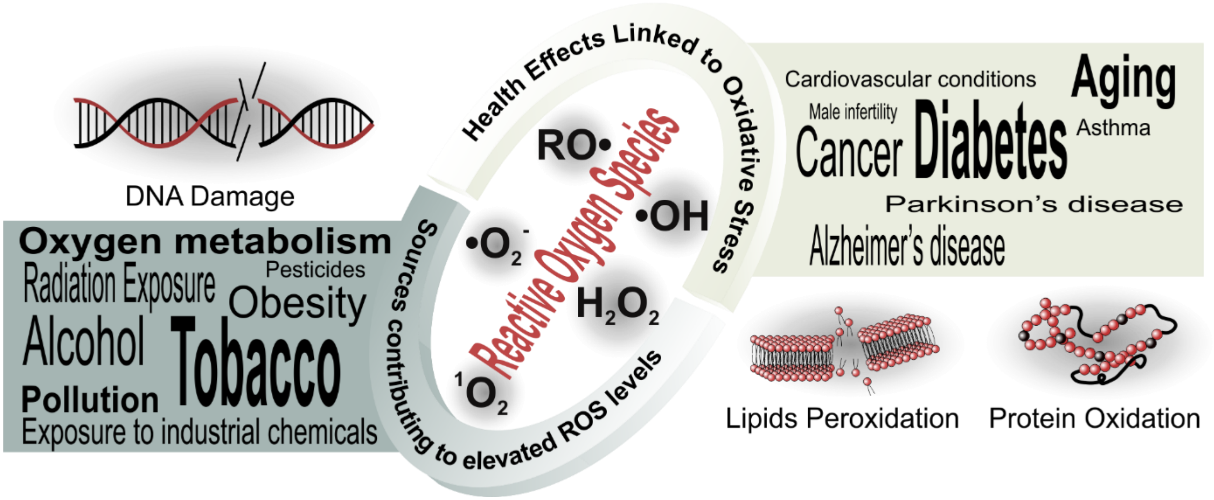

Figure 1. Endogenous and exogenous sources as well as the health-related effects of oxidative stress. ROS are capable of inflicting severe and non-specific damage to cellular components such as membrane lipids, proteins, and DNA.

In addition, during an immune response, phagocytic cells such as macrophages and neutrophils trigger a respiratory burst, during which phagocytic NADPH oxidases generate $\bullet O_2^-$ that takes part in the elimination of invading pathogens. The NADPH oxidases are a family of membrane-bound enzymes whose primary function is the catalysis of $\bullet O_2^-$ production.[5, 6]

Besides, peroxisomes are organelles that are present in the cytoplasm of eukaryotic cells, these oxidative organelles host a variety of enzymes that play vital roles in the metabolism of lipids as well as the generation and detoxification of ROS including •OH, H_2O_2, and $•O_2^-$. Peroxisomal enzymes include urate oxidase, nitric oxide synthase, xanthine oxidase, CAT, and SOD.[6, 7] ROS can also be produced during the metabolism of certain substances such as arachidonic acid by lipoxygenases and cyclooxygenases.[8] While ROS are unavoidably formed under normal conditions, certain exogenous influences can greatly contribute to elevated ROS levels as well, as shown in **Figure 1**. Cigarette smoke, for example, is a significant source of free radicals such as superoxide and nitric oxide.[2] Other external contributors to elevated levels of ROS include pesticides, pollutants, hypoxia, heavy metals, and exposure to ionizing radiation and ozone.[2, 9, 10]

At normal levels, ROS are essential to numerous physiological processes. As mentioned earlier, superoxide, produced during phagocytosis, is heavily involved in eliminating invading pathogens.[9] In fact, a defective NADPH oxidase system compromises the ability of phagocytes to produce superoxide giving rise to granulomatous disease, where the resulting immunodeficiency renders diagnosed individuals prone to multiple and persistent infections.[11] ROS are also essential in cross-linking of the extracellular matrix and in the hardening of the fertilization envelope after egg-sperm fusion.[11] They also play a major part in biosynthetic reactions as well as various cellular redox-signaling pathways.[12] In fact, ROS such as H_2O_2 play a major role as a redox signaling agent in many biological functions such as DNA repair, transcription, protein folding, and genome integrity.[13] Excess or non-regulated accumulation of ROS, however, is associated with several serious health-related issues.[14] ROS may adversely interact with proteins and vital components of cell structures resulting in protein denaturation, lipids peroxidation as well as damage and fragmentation of nucleic acids (DNA and RNA).[2, 15] Often, these interactions result in mutations and irreversible alterations in signal transduction leading to altered cell proliferation and ultimately trigger cell death.[16] As **Figure 1** shows, these non-specific damages may develop and express into countless complications and health-related issues such as aging, atherosclerosis, cancer, cardiovascular diseases, diabetes, and neurodegenerative disorders such as Parkinson's and Alzheimer's diseases.[17, 18]

2.2 Antioxidants

2.2.1 Classification of antioxidants

To combat oxidative stress and preserve cell health, biological systems employ several defense mechanisms against ROS including prevention, scavenging, and repair mechanisms using a vast array of antioxidants, which are highly effective in the regulation and elimination of excess ROS and are, therefore, essential to the well-being of a living system.[12, 19] Antioxidants are classified according to different criteria such as structure, source, and mode of action. Structurally, antioxidants can be enzymatic (complex proteins) or non-enzymatic (simple organic molecules or metal ions such as selenium and manganese).[2, 20] On the other hand, non-enzymatic antioxidants can be endogenous (e.g., glutathione) or exogenous, i.e., obtained from dietary sources (e.g., carotenoids, α-Tocopherol, and vitamin C).[2]

In addition, the defense mechanism of antioxidants depends on the way, in which the oxidative damage is inhibited. Like any free-radical chain reaction, the autoxidation of cellular substrates such as membrane lipids, proteins, or DNA involves initiation, propagation, and termination phases. Various pathways lead to the formation of *initiating radicals*, which can trigger the propagation of the free-radical chain oxidation of substrates. For example, the Fenton reaction leads to the formation of •OH as initiating radicals. *Preventive* antioxidants prevent the formation of initiating radicals by the conversion of their mother ROS into harmless chemical species. For example, the SOD/CAT enzyme cascade catalyzes the conversion of superoxide ($\bullet O_2^-$) into O_2 and water, and thus, prevents the formation of •OH via the Fenton reaction.[4] On the other hand, *chain-breaking* antioxidants (e.g., glutathione and vitamin E) act by competing with the substrate for the *intermediate radicals*, generated during chain propagation. Thus, chain-breaking antioxidants terminate free-radical chain reactions through the elimination (scavenging) of radical intermediates through electron donation. Naturally, these antioxidants are converted to new radicals during their antioxidation action, but the newly formed radicals are largely less harmful.[4, 21] Also, repair systems play maintenance roles by repairing the oxidative damage already caused to biomolecules such as DNA.[21]

2.2.2 Applications of antioxidants

Apart from oxidative stress prevention, antioxidants are widely applied in numerous fields such as pharmaceutical, cosmetic, textile, food, fuel, lubricants, plastic, and rubber industries, as shown in **Figure 2**.[22, 23] In pharmaceuticals, for example, antioxidants are added to prevent degradation and improve the stability of therapeutic agents that are prone to oxidation.[22] In addition, lanthanides, lycopene, glutathione, and flavonoids are antioxidants that are reported to have potential as anticancerous agents. Antioxidants are also used as additives in commercial cosmetic products.[24] For example, vitamin A derivatives, phenolic compounds, and carotenoids are added to commercial skin care products as anti-aging agents to prevent inflammation, premature aging, and pigmentation disorders.[25, 26] Vitamin B5 (panthenol) is used in haircare products to improve hair elasticity, while retinaldehyde (vitamin A derivative) can also serve as a stabilizer to prevent lipid rancidity.[26] In addition, the combination of vitamins C and E in recently-manufactured cosmetics is expected to provide enhanced skin protection against UV radiation as well as photooxidation.[27]

In the food industry, antioxidants are widely used in food processing and food packaging materials.[28, 29] They have the potential to slow down the autoxidation process of biological molecules such as lipids and proteins that can lead to rancidity, reduced shelf-life as well as the development of undesirable taste and fragrance, resulting in the deterioration of texture and quality of nutrient substances.[30] Examples of antioxidants used in the food industry include propyl gallate, tertiary butyl hydroquinone, and butylated hydroxytoluene.[10] Thus, the prevention of oxidation of biological molecules in food products can effectively extend the shelf-life and preserve the texture, color, freshness, fragrance, and quality of nutrient substances.

Figure 2. Various established industrial applications of enzymatic and molecular antioxidants.

Moreover, antioxidants are also frequently used as additives and stabilizers in numerous other industrial applications. For instance, antioxidants prevent the oxidation of fuels and polymerization of gasoline, which leads to the formation of engine-fouling residues.[31] Also, they prevent photooxidative degradation as well as the loss of strength and flexibility in polymeric materials such as rubber and polyolefins especially polyethylene.[32]

On the other hand, antioxidant enzymes are heavily used in industrial applications as well.[33] For example, peroxidase enzymes are used in food manufacturing to improve food quality, as well as produce flavor, color, and texture. They are also used in biosensors, polymer synthesis, management of environmental pollutants, treating phenolic effluents from industries, and antimicrobial products.[33, 34] The CAT enzyme, on the other hand, is used in the textile industry to remove excess H_2O_2 from fabric. In the food industry, the glucose oxidase/CAT combination is used during milk processing, and for the elimination of O_2 from wine prior to bottling. In the baking industry, the CAT enzyme is also added to remove H_2O_2 from milk, as well as glucose from egg white. In addition, the CAT enzyme is also incorporated in food wrappers to prevent oxidation and control the quality of food.[34] In the textile industry, the peroxidase and CAT enzymes are used for the removal of excess dye and bleach termination, respectively.[33] The SOD enzyme is used as an anti-aging additive in cosmetic products to reduce free-radical damage to the skin, and thus, to eliminate signs of aging such as wrinkles and hyperpigmentation. The SOD enzyme also exhibited potential in preventing hair graying, promoting hair growth, wound healing, protection against UV rays, and suppressing fibrosis after radiation treatment.[35] In addition, the SOD enzyme is frequently applied in medical treatments due to its anticancerous, antioxidant, and anti-inflammatory effects.[36, 37]

2.2.3 Enzyme kinetics

Generally, enzymes primarily consist of highly complex protein structures with one or more active sites, where the enzymatic reaction takes place. The structure of the active site is highly specific to the substrate (the substance on which the enzyme acts such as ROS), where the binding is enabled through a unique combination of hydrogen bonding, electrostatic forces, and van der Waals interactions among the various functional groups on the substrate and the active site.[38-40] The complexity of enzymatic structures, and thus, the binding interactions have rendered many enzyme-catalyzed reactions stereoselective and stereospecific such as hydrolysis reactions catalyzed by C. cylindracea lipase, acylase, pig liver esterase.[39]

The substrate-active site binding is believed to occur in several binding mechanisms, shown in **Figure 3**. In the *lock-and-key model,* proposed by German chemist Emil Fischer (1852–1919) in the 1890s, the active site and substrate have complementary 3D structures and docking occurs without the need for major structural changes. However, the experimental evidence on the flexibility of proteins in solution and the distortion in the conformation of the transition state upon biding suggests the *induced-fit mechanism* and *conformational selection* mechanisms. In the former, the binding of the substrate induces a conformational change in the active site, resulting in the ideal fit, after which the enzymatic reaction takes place. In the conformational selection mechanism, on the other hand, the active site undergoes a conformational change prior to the binding of the substrate.[41]

The kinetics of enzyme-catalyzed reactions is among the most studied aspects of biocatalysis, for it provides critical information on the mechanism of biocatalysis. Studies on enzyme kinetic typically involve monitoring the *initial* rate of product formation at very low enzyme concentration, since significant acceleration may be observed, even when their concentration is more than three orders of magnitude lower than that of the substrate.

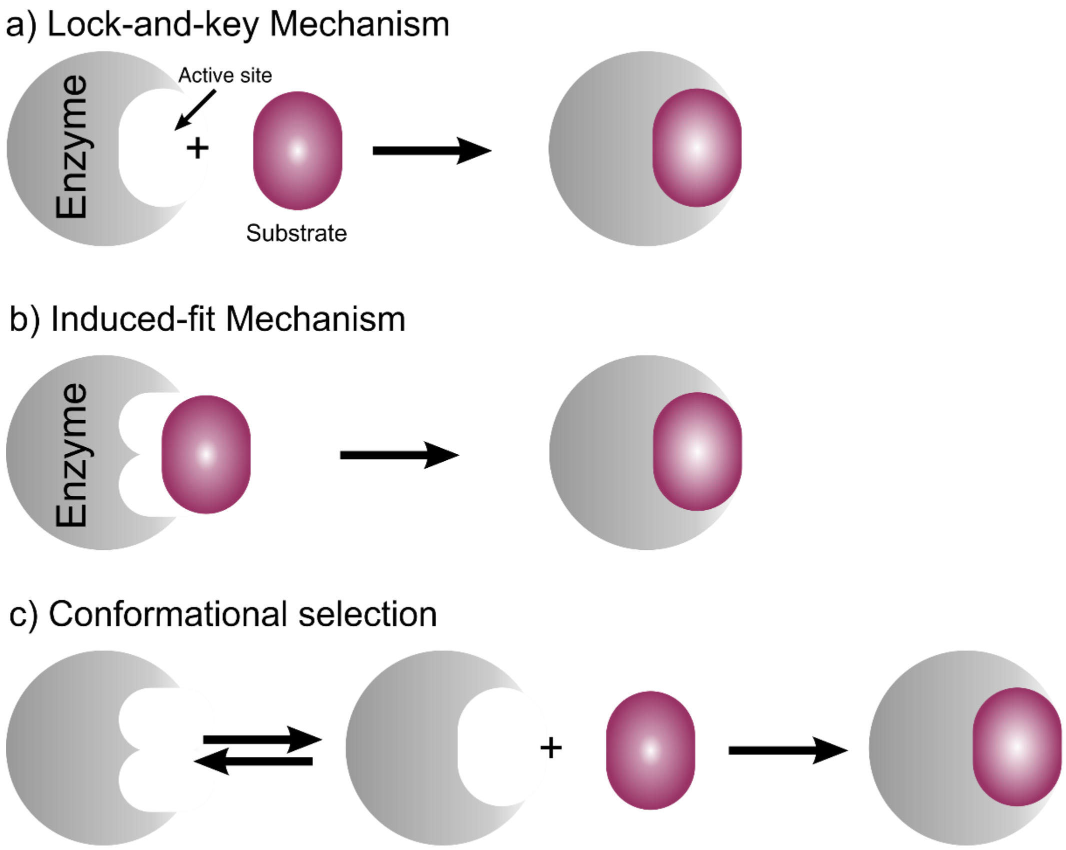

Figure 3. Schematic representation of substrate-active site binding mechanisms: (a) lock-and-key, (b) induced-fit, (c) conformational selection. For simplicity, enzymatic and substrate structures are represented as rigid blocks.

Experimental studies on enzyme kinetics revealed several observations:[42]

1. The *initial* rate of product formation, v, is proportional to the total enzyme concentration, $[E]_o$ (for a given *initial* substrate concentration, $[S]$).
2. Conversely, for a given *initial* enzyme concentration, $[E]$; v is proportional to $[S]$ (at low $[S]$) and independent of $[S]$ (at high $[S]$). In the latter case, all enzyme molecules are bound to the substrate molecules, and the rate becomes zero-order in $[S]$.

Based on these observations, a mathematical analysis shows that the relationship between v and $[S]$ can be represented by the equation of a rectangular hyperbola:

$$v = \frac{a[S]}{b + [S]} \qquad (1)$$

where a and b are constants. To account for these observations, German biochemist Leonor Michaelis (1875–1949) and Canadian biochemist Maud L. Menten (1879–1960) proposed a mechanism in 1913 to explain the dependence of the initial rate of enzyme-catalyzed reactions on the concentration by assuming that enzyme and substrate are in thermodynamic equilibrium with the enzyme-substrate complex, *ES*, that can separate back into substrate and enzyme or proceed to product, *P*, formation. Later in 1925, British biologists George Briggs (1893–1978) and John Haldane (1892–1964) alternatively used the steady-state approximation to obtain the *Michaelis-Menten equation* of enzyme kinetics:[41]

$$v = \frac{v_{max}[S]}{K_{\mathrm{m}} + [S]} \tag{2}$$

The derivation of the Michaelis-Menten equation based on both assumptions is fully described in **Appendix A**. The v_{max} represents the maximum possible reaction rate, where the total enzyme concentration equals that of the enzyme-substrate complex, i.e., all the enzyme molecules are bound with the substrate as *ES*. On the other hand, K_{m} is the *Michaelis constant* and represents the $[S]$, at which the initial rate is half that of $v_{max,}$ or the $[S]$ at which half the enzyme active sites are occupied by substrate molecules. The K_{m} is different for each enzyme and depends on the substrate, it is a measure of the affinity between the enzyme and the substrate, where lower K_{m} values indicate higher affinity between the enzyme and the substrate, and vice versa. Hence, the v_{max} and K_{m} of the Michaelis-Menten model are the commonly reported kinetic constants characterizing enzyme-catalyzed reactions including those catalyzing ROS scavenging.

2.2.4 Artificial enzymes

Despite their flawless catalytic performance, antioxidant enzymes possess several inherent drawbacks such as high sensitivity to operational conditions including pH and temperature.[43] When subject to undesignated conditions, the vital structures of the comprising proteins gradually denature leading to a permanent loss of enzymatic activity.[44] For example, the optimal operating temperatures of SOD and CAT enzymes were reported to be around 30 °C, where their activities rapidly deteriorate when the operation temperature is significantly different from 30 °C. The SOD lost 90% and 100% of its activity when the operating temperature was 10 °C and 70 °C, respectively. Also, the CAT enzyme undergoes an 80% reduction in activity when the operating temperature is either 70 °C or 10 °C.[45] On the other hand, the optimal operational pH of SOD and CAT enzymes are 6-7 and 6.5-7, respectively. Like the operational temperature, the activities of both enzymes significantly deteriorate when the pH is substantially different from the optimal pH range. The SOD becomes inactive when the pH is reduced to 3.0 and undergoes around 60% loss of activity when the pH is 9. The CAT enzyme, on the other hand, loses around 95% of its activity at pH 3, and 80% at pH 9.[45] In addition, the thermal stability of the SOD enzyme is reported to be highly affected by incubation temperature. In fact, the SOD enzyme underwent a total loss of activity when incubated at 80 °C for 60 min.[46] For the horseradish peroxidase (HRP) enzyme, the optimal operation pH was reported to be around 4.8, and the activity rapidly deteriorates when the pH is altered, the HRP loses activity as the pH approaches 3 or 5.5, leaving a small window of operation. In addition, the optimal operating temperature of HRP is 35 °C. Similar to SOD and CAT, the activity of HRP is significantly affected by the change in temperature, where a total loss of activity was observed at 60 °C.[47]

Thus, with such high sensitivity to experimental conditions, the enzyme production and purification processes are considerably complicated, expensive, and time-consuming.[43, 44, 48, 49] These limitations have paved the way for the exploration and subsequent discovery of artificial enzymes, which are non-enzymatic substances with enzyme-like biocatalytic potential. These enzyme mimics are foreseen to have low sensitivity to experimental conditions and yet deliver equally effective enzyme-like catalytic potential. In fact, the investigation of the enzyme-like catalysis of cyclodextrin inclusion compounds in 1965 is among the earliest reports on artificial enzymes.[50] Later, other structures of artificial enzymes were slowly emerging such as polymers with enzyme-like potential in 1971, catalytic antibodies in 1986, catalytic RNA in 1992, catalytic DNA in 1994, and SOD mimicry and DNA-cleavage potential of fullerene derivatives.[50-52] Further works revealed enzyme mimics of diverse structures including metal complexes, polymers, and dendrimers.[53-56]

However, since the reports on peroxidase mimicry of Fe_3O_4 nanoparticles in 2007, extensive research has been devoted to the exploration of the enzyme-like antioxidant potential of nanomaterials, which revealed immense potential in mimicking a vast array of enzymes including antioxidant ones such as CAT, HRP, and SOD.[50, 57] These nanostructures include metallic nanoparticles such as Ag,[58] Au,[59] Pt,[60] and Pd;[61] metal oxides such as Co_3O_4,[62] CeO_2,[63] and CuO nanospheres[64], as well as V_2O_5 nanowires;[65] metal chalcogenides such as FeS,[66] MoS_2,[67] and WS_2 nanosheets;[68] carbon derivatives as fullerenes, carbon nanotubes, nanodots; and MOFs.[57, 69, 70] Unlike natural antioxidants, enzymatically active nanomaterials (nanozymes) have low-cost and often simple synthesis processes, as well as robust structural and functional stability in wide pH and temperature ranges, typically well outside the operational range of the mimicked enzymes. Most importantly, many nanozymes are biocompatible and biodegradable materials with highly tunable physicochemical properties. Thus, nanozymes are expected to possess outstanding antioxidant potential in various biomedical and industrial applications, as well as in conditions where the native enzymes are inactive.[71, 72] Nanozymes with antioxidant potential have indeed been applied in numerous biomedical applications such as tumor therapy, bioanalysis, disease diagnosis, biosensors, and cytoprotection.[40, 73, 74] For instance, Fe_3O_4-PtFe composites exhibited antitumor potential while boron oxynitride showed potential in breast cancer therapy.[75, 76] In addition, the peroxidase activity of nanozymes has been heavily explored in the clinical diagnosis of numerous target molecules such as As^{5+} (ACP/hemin@Zn-MOF), chloramphenicol (Co_3O_4), and MiRNA-141 (Co_3O_4-Au polyhedron), as well as in the removal of a large variety of pollutants in water including phenols (Zr-MOF), atrazine (Fe_3O_4-TiO_2/rGO), methyl blue (Au@cuxs/ZnO), and natural organic matter (Carbon-doped Fe_3O_4).[77] A summary of the advantages, scope, and potential applications of nanozymes is shown in **Figure 4**.

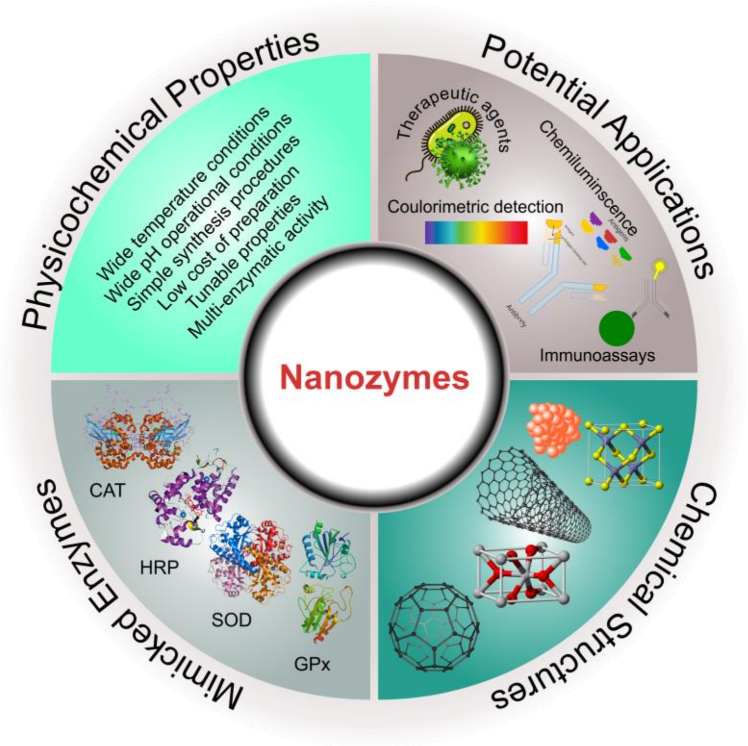

Figure 4. Structures, physicochemical properties, and potential applications of enzyme-mimicking nanomaterials (nanozymes) as alternatives to many natural enzymes of diverse catalytic roles.

As seen above, nanozymes are often applied in composite form rather than bare materials. Hence, the formulation of such composites via the *ex-situ* method, for example, requires a thorough understanding of the colloidal behavior of nanoparticles and the interparticle interactions governing the colloidal behavior, since numerous industrial and biomedical applications require their introduction into fluid, typically aqueous, media.

2.3 Colloidal systems

Colloids are heterogeneous mixtures in which one component, the dispersed phase, is suspended throughout another, called the dispersion medium. Both constituents can be solid, liquid, or gas; and the nature of the system is largely dependent on the state of both phases. For instance, gaseous dispersed phases result in foams, while gaseous dispersion media give rise to aerosols. In colloids of condensed phases, on the other hand, dispersed liquid phases result in emulsions, while solid dispersed phases form sols.[78, 79] The various classifications of colloidal systems along with examples are listed in **Table 1**.

Table 1: Classification of colloidal systems.

Colloid	Dispersed phase	Dispersion medium	Examples
Aerosol	Liquid	Gas	Fog
Solid aerosol	Solid	Gas	Smoke
Foam	Gas	Liquid	Soap
Solid foam	Gas	Solid	Lava
Sol	Solid	Liquid	Colloidal gold
Solid sol	Solid	Solid	Ruby glass
Emulsion	Liquid	Liquid	Milk
Solid Emulsion	Liquid	Solid	Opal

In such mixtures, however, the dispersed phase is not present as individual ions or molecules as the case with true solutions; rather, it occurs as gas bubbles, liquid droplets, or solid particles. To be classified as a colloid, the dispersed phase must have at least one dimension in the range of 1-1,000 nm.[78] Hence, colloidal systems have observable properties that are intermediate between those of true solutions and suspensions (characterized by micron-sized dispersed particles). In stable sols, for example, solid particles do not spontaneously settle down under the influence of gravity but remain well suspended in the liquid medium under constant thermal motion, called the Brownian motion.[80] Colloidal systems also exhibit the Tyndall effect, i.e., the scattering of lights by colloidal particles, as evidenced by visible light path upon shining a beam of light through the system.

2.3.1 Applications of colloidal systems

Colloids occur frequently in nature such as blood, mud, river deltas, fog, clouds, smoke, and dust. Also, natural phenomena such as haze and red sunset are attributed to the colloidal nature of the earth's atmosphere. Colloids are also central in biology, the environment, and numerous other fields such as pharmaceuticals and the food industry, where many items such as milk, ice cream, and butter are colloidal in nature.[81] As shown in **Figure 5**, stable colloids also occur in many commercial products such as cosmetics, paints, inks, plastics, pigments, and paper.[81-83]

On the other hand, many essential industries and engineered processes are based on the manipulation of existing colloidal systems to achieve the desired purpose. The induction of artificial rain or cloud seeding, for example, is attained by spraying clouds with charged particles such as silver iodide or dry ice, these can neutralize the charge on water droplets leading to the coalescence of and induction of rain.[84] Besides, in water purification, suspended impurities are removed via coagulation, i.e., by the introduction of salts of iron or aluminum, which leads to sedimentation.[85] Similarly, rubber is obtained via coagulation of latex colloidal systems, whereas the process of tanning (obtaining leather by treatment of animal skin) involves the addition of negatively charged particles to the colloidal animal skin containing positively charged components, leading to coagulation and skin hardening.[86, 87]

Figure 5. Industrial applications involving colloidal systems. These include the preparation of stable colloidal systems or bringing about destabilization of already existing ones.

2.3.2 *Nanocolloids*

Nanocolloids are a subclass of colloidal systems comprising particles of at least one dimension within the nanoscale (1-100 nm) dispersed in fluid, usually aqueous, media. The comprising nanostructures encompass a vast array of highly functional materials with various shapes, sizes, and chemical compositions including metallic and polymeric particles, (transition) metal oxides, metal chalcogenides, coordination compounds, MOFs, carbon materials, and cluster compounds.[88-91] As shown in **Figure 6**, which shows the colloidal domain and the nanoscale, biological structures such as proteins, DNA, and microorganisms such as viruses also have dimensions within the nanoscale.

Nanomaterials exhibit unique physicochemical properties that are intermediate between those of individual atoms/molecules and bulk materials. In fact, as the particle size approaches the nanoscale, significant changes are observed in numerous physicochemical properties such as electrical conductivity, magnetic properties, heat conductivity, mechanical properties such as strength and flexibility, chemical reactivity, catalytic potential, color, and melting point.[92] Such changes are generally attributed to four major phenomena: 1) the enormous increase in the surface area, 2) the subsequent high surface energy, 3) the quantum confinement, and 4) the reduced imperfections.

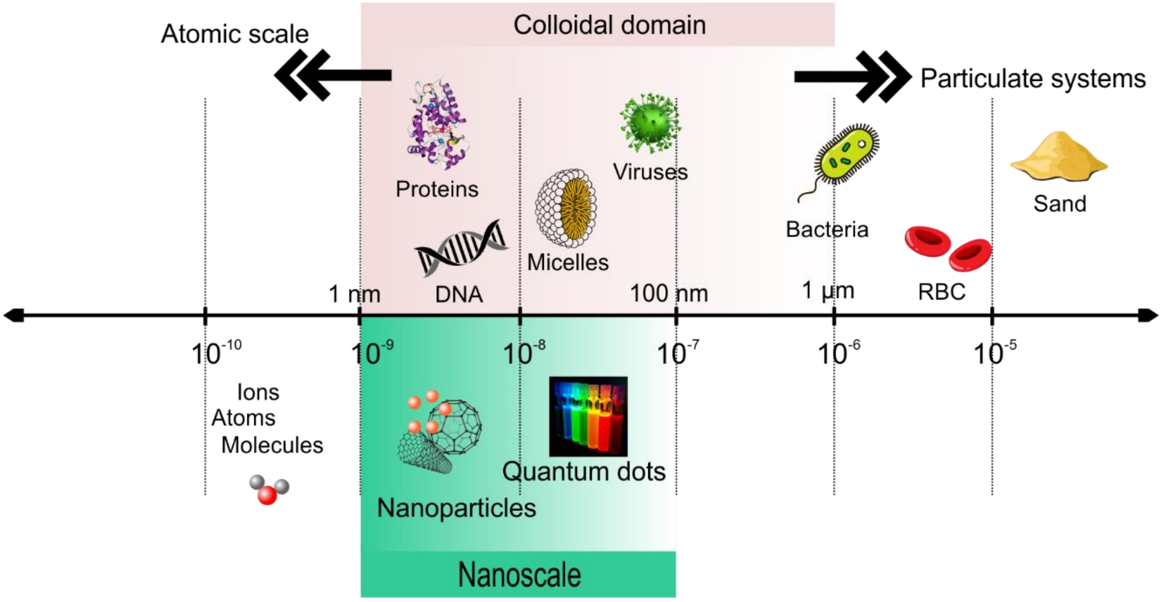

Figure 6. The nanoscale and the colloidal domain. Both scales include not only inorganic nanostructures but also biomolecules such as proteins as well as biological systems such as viruses. Beyond the colloidal domain lies particulate systems, which are characterized by micron-sized components.

Figure 7 illustrates the dramatic increase in the surface area as the particles approach the nanoscale. A solid cube, with a 1.0-cm side length, has a surface area of 6.0 cm^2; however, when that same 1.0-cm^3 cube is divided into 1.0 nm^3-sized cubes, the resulting 10^{21} cubes have a total surface area of 6,000 m^2, which is comparable to the area of a soccer field! The creation of more surfaces results in higher surface free energy and increased chemical reactivity including the emergence of catalytic potential. For example, metallic Au NPs are active enzyme-mimicking materials, whereas nanoclusters of transition metals such as Pd exhibit catalytic potential toward various reactions such as oxidative acetoxylation of ethylene.[93, 94] In addition, the reduction of particle size to the nanoscale brings about quantum effects such as the quantum confinement of electrons. As shown in **Figure 7**, the change in the size and shape of nanomaterials gives rise to significant changes in the density of charge carriers and the structure of the energy band, which, in turn, will modify the electronic and optical properties of the materials by altering the energies of electronic transitions.[95] For example, semiconductor 2.3-nm CdSe NPs have blue color that turns into red when the particle size increases to 5.5 nm while nanosized Au can appear red or purple depending on the particle size.[92] Also, the melting point of bulk Au (1,064 °C) becomes lower than the boiling point of water when the particle size is reduced to 2.0 nm.[92] Magnetic properties are also prone to change when the particle size is reduced. For example, diamagnetic bulk Au becomes magnetic at the nanoscale, while ferromagnetic metals such as bulk Co and Ni become superparamagnetic at the nanoscale, as the nanoparticles comprise a single magnetic domain if the particle size drops below a critical value.[92] On the other hand, nanosized particles exhibit improvement in mechanical properties such as toughness, hardness, and elasticity, compared to their bulk counterpart.[88]

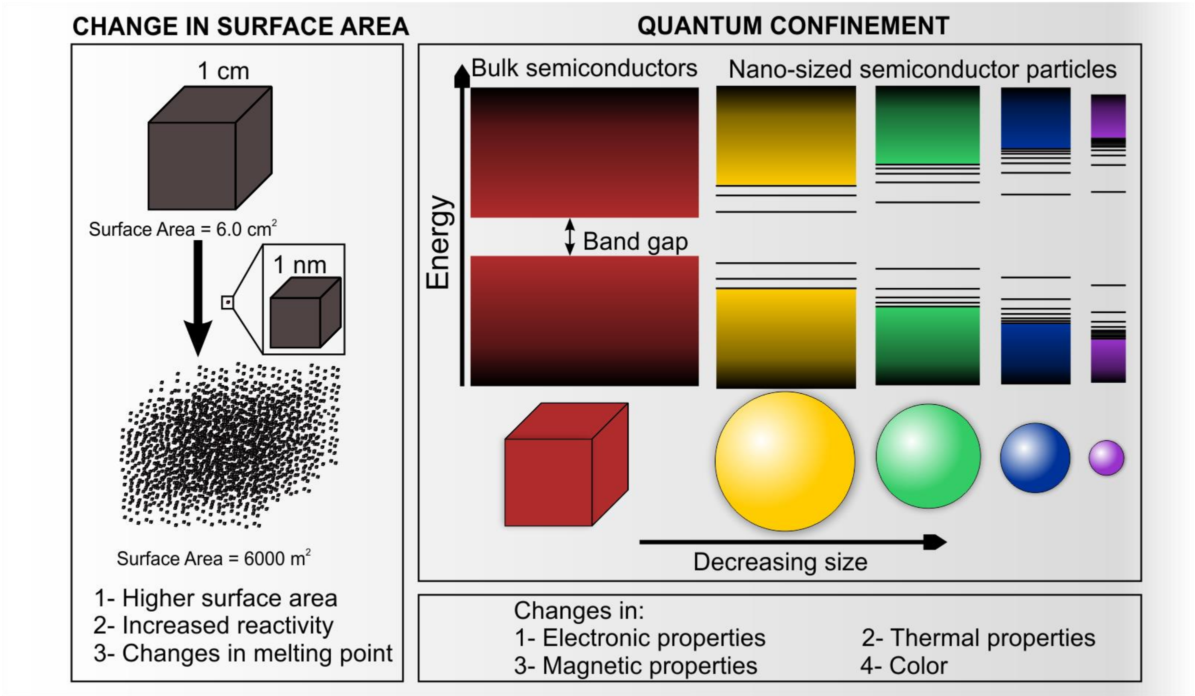

Figure 7. The emergence of nanoscale phenomena and their effects on the physicochemical properties of materials as the particle size approaches the nanoscale.

The gradual change in physicochemical properties has given rise to the concept of tunability of properties, which allows the preparation of nanomaterials with desired properties by manipulating the size and shape of the particles through the systematic alternation of synthesis conditions. This has enabled the use of nanostructured materials in countless applications and fields including electronics, energy storage and conversion, catalysis, environmental remediation, and biomedical applications.[88, 96] They are also used in several industries including cosmetics, food processing, construction materials, and aerospace.[97, 98] In biomedical applications, biocompatible nanomaterials are commonly utilized in drug delivery, diagnosis, imaging, and therapy, and often exhibit potential as anticancerous, antibacterial, and anti-inflammatory agents.[99-103] The state of nanomaterials during a certain application, however, is highly dependent on the nature of the materials as well as the application itself. For example, nanomaterials may be suspended in gaseous or liquid media, or they are immobilized or embedded in a solid matrix. For instance, in supercapacitors, the anode and cathode materials are typically embedded into a solid substrate,[104] while during heterogeneous catalysis (e.g., ROS scavenging) or drug delivery, the material is dispersed in aqueous or physiological media.[105] Therefore, a thorough understanding of the physicochemical properties of nanomaterials in colloidal systems is crucial for their effective use in various applications.

2.3.3 *Colloidal stability*

As seen earlier, the applications of colloids involve either the formation of stable and highly functional systems or a systematic manipulation of existing ones and thus, a versatile utilization of colloidal systems warrants a solid understanding of colloidal stability as well as the interactions governing colloidal behavior. Hence, it is no surprise that extensive research, theoretical and experimental, has been devoted to understanding the interparticle interactions in colloidal systems.

2.3.3.1 *Interactions in colloidal systems*

In colloidal systems, the introduction of solid phases into fluid media brings about different interaction regimes including intraparticle, interparticle, and particle-medium interactions and the overall physicochemical properties of the resulting system are dependent on the magnitude of these forces and the interplay among the different interaction regimes. In addition, while some of these interparticle forces are inherent to the nature of the dispersed materials, others are largely affected by experimental conditions such as temperature, ionic strength, pH, nature of the dispersion medium, particle size, particle shape, surface modification, and presence of polymeric materials or surfactants, which render colloidal systems susceptible to a number of dynamic processes such as sedimentation, coagulation, flocculation, dissolution, or chemical alterations.

While ion-ion interactions are long-ranged (as evident by the dependence on the separation distance of force in Coulomb’s inverse-square law), all interaction forces among atoms and molecules are *short-ranged* (effective at distances up to 1 nm) but are *electrostatic* in nature as well, which means that Coulomb’s inverse-square law can theoretically still be used to obtain the force of interaction upon obtaining the spatial distribution of electron clouds using Schrödinger equation.[106] However, since exact solutions are difficult to obtain, even for the simplest cases, these forces are divided into different categories, even though they are all electrostatic in origin and thus, emerge the concepts of dipole-dipole forces, hydrogen bonding, solvation forces, and so on. For interactions between *macroscopic* particles and surfaces, on the other hand, interactions are *long-ranged* (< 100 nm) but can be *electrostatic* in origin (e.g., van der Waals forces) or *entropically* driven (e.g., electrostatic and steric forces).[106] The different types of interparticle forces in colloidal systems are summarized in **Figure 8**.

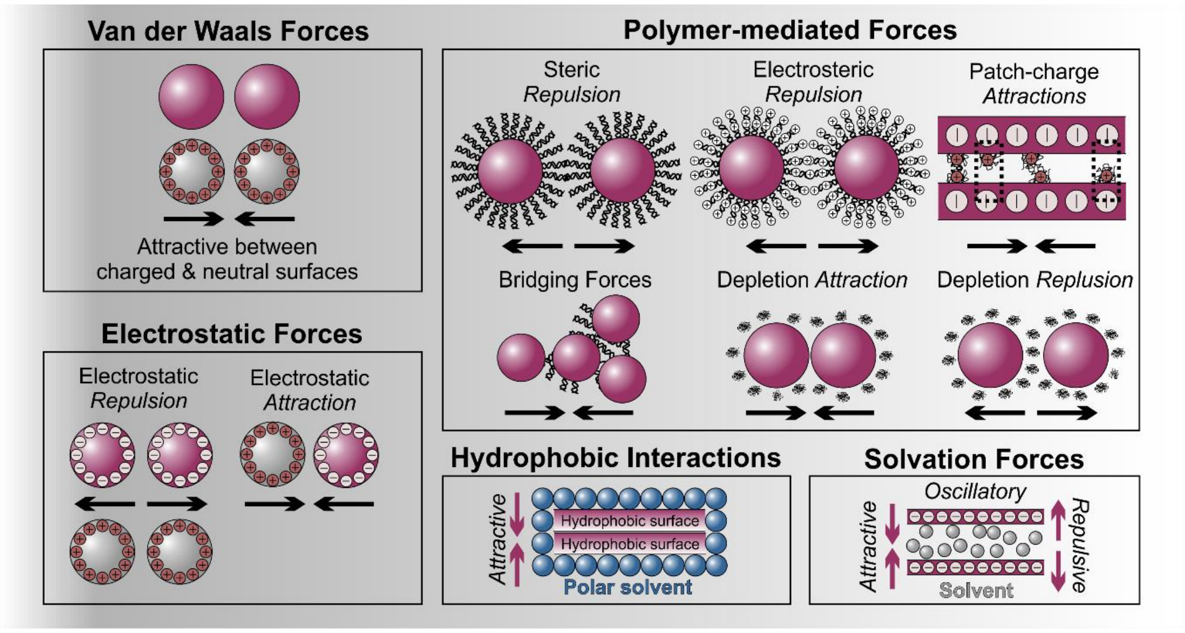

Figure 8. Interparticle forces that occur within colloidal systems. The *van der Waals* forces always exist among charged and neutral species and are always attractive among similar particles (unless the refractive index of the particles matches that of the medium). The *electrostatic* forces play a significant role among the charged particles. The presence of polymeric chains (neutral or charged) within colloidal systems brings about several other regimes of interaction forces. The *steric repulsion* occurs because of repulsion among extended neutral polymeric chains adsorbed on interacting particles, while charged macromolecules (polyelectrolytes) bring about *electrosteric repulsion*. The *patch-charge attractions* occur between a charged surface and patches of oppositely charged polyelectrolyte chains adsorbed on an approaching surface. Bridging of colloidal particles via adsorbed polymeric chains leads to the *flocculation* of particles. *Depletion* interactions occur in the presence of polymeric macromolecules in a free (non-bound) state. *Hydrophobic interactions* are strongly attractive forces that occur among hydrophobic surfaces in polar solvents, and *solvation forces* are oscillatory (repulsive or attractive) forces that occur due to the re-structuring of solvent molecules as two surfaces approach one another.

2.3.3.1.1 The van der Waals forces

The van der Waals (vdW) forces always exist among charged and neutral species and are attractive as long as the refractive index of the particles is different from that of the medium. In addition, these forces comprise three types of interactions depending on the polarity of the interacting species.[106] First, Keesom (1912) or dipole-dipole interactions strictly occur between permanent dipoles of polar molecules. In the gas or liquid phase, dipoles are in constant rotatory motion but a favored interaction results in the alignment of dipoles that leads to electrostatic attraction. Second, the dipole-induced dipole or Debye (1920) interactions are brought about when a polar molecule alters the electron cloud distribution, i.e., induces a dipole, in nearby non-polar molecules, which leads to favored alignment of dipoles and induced dipoles, as in Keesom interactions. Third, instantaneous dipole-induced dipole or London (1930) forces, also called dispersion forces, occur between all types of molecules and are quantum mechanical in origin, as opposed to the electrostatic nature of Keesom and Debye forces. For any molecule (polar or non-polar), the electron cloud can be unevenly distributed at any arbitrary moment, which gives rise to an instantaneous dipole that alters the electron cloud of any nearby molecules, resulting in an induced dipole that interacts with the former via electrostatic attractive forces. These three forces (Keesom, Debye, and London) are collectively called the vdW forces, each characterized by short-ranged (6th inverse power separation dependence) and attractive (negative) interaction potential, $V(r)$:

$$V(r) \propto -\frac{1}{r^6} \tag{3}$$

where r is the center-to-center distance between the two interacting molecules. The total potential energy of vdW interactions is the sum of the contributions of the three forces:[106, 107]

$$V(r)_{vdW} = V(r)_{Keesom} + V(r)_{Debye} + V(r)_{London} \tag{4}$$

Obtaining the interaction potential of vdW forces between two macroscopic surfaces or particles requires the assumption of pairwise additivity and non-retardation of vdW interactions. The pairwise addition is achieved by summing the interaction energies of all atoms/molecules in one body with all atoms/molecules in the other; this approach is called the *Hamaker summation method*.[108] For two surfaces at some surface-to-surface distance, x, from each other, the resulting net two-body vdW interaction potential, $V(x)_{vdW}$, is largely dependent on the geometry of the interacting surfaces.[109]

For two finite planar surfaces of thickness h_1 and h_2:

$$V(x)_{vdW}^{plate} = -\frac{A}{12\pi}\left(\frac{1}{x^2} + \frac{1}{(x + h_1 + h_2)^2} - \frac{1}{(x + h_1)^2} - \frac{1}{(x + h_2)^2}\right) \times area \tag{5}$$

For two spherical surfaces with radii R_1 and R_2:

$$V(x)_{vdW}^{sphere} = -\frac{A}{6}\left(\frac{2R_1R_2}{(2R_1 + 2R_2 + x)x} + \frac{2R_1R_2}{(2R_1 + x)(2R_2 + x)} + ln\frac{(2R_1 + 2R_2 + x)x}{(2R_1 + x)(2R_2 + x)}\right) \tag{6}$$

where A is the Hamaker constant.[106, 110] The above expressions can be simplified for the limiting cases. For example, when planar surfaces have an infinite or semi-infinite thickness or when the separation is much smaller than the radii of the particles ($R \gg x$), equations (5) and (6) simplify to equations (7) and (8), respectively:

$$V(x)_{vdW}^{plate} = -\frac{A}{12\pi x^2} \times area \tag{7}$$

$$V(x)_{vdW}^{sphere} = -\frac{A}{6x}\left(\frac{R_1 R_2}{R_1 + R_2}\right) \tag{8}$$

In addition, at short separations, other interaction potentials have simple expressions. For example, the interaction potentials between two cylinders (side-to-side) with radii R_1 and R_2, and between an infinite planar surface and a spherical with radius R are[106, 110]

$$V(x)_{vdW}^{cyliner} = -\frac{A}{(12\sqrt{2})x^{3/2}}\left(\frac{R_1 R_2}{R_1 + R_2}\right)^{1/2} \times length \tag{9}$$

$$V(x)_{vdW}^{plate/sphere} = -\frac{AR}{6x} \tag{10}$$

Thus, the vdW forces between macroscopic particles depend on the size, geometry, separation distance, the nature of the material, and the physicochemical properties of the medium. The dependence of vdW interactions on the last two factors is manifested in the value of the Hamaker constant. Compared to vdW interactions between molecules and atoms, the interaction potential between macroscopic surfaces decays much slower with the absolute separation distance, as evident by the separation dependence in the vdW expressions, which renders vdW forces a long-ranged force in colloidal systems.[106]

The Hamaker approach is based on numerous assumptions including the disregard for the influence of neighboring atoms on the interaction between any pair and the pairwise additivity of the interactions. Thus, while the effect of neighboring species is minimized in gaseous phases, it cannot be ignored in condensed ones, which questions the validity of pairwise addition. In the *Lifshitz approach*, proposed by Evgeny Mikhailovich Lifshitz (1954) to treat vdW interactions, the chemical structures are neglected as the particles are treated as continuous media. Also, the forces are derived in terms of bulk properties such as dielectric constant and refractive index. Thus, the Lifshitz approach is not based on the assumption of pairwise additivity, and hence, the influence of neighboring molecules is considered. Also, the Lifshitz approach allows the use of the same interaction potential equations for the various geometries since only the Hamaker constant is obtained differently. Thus, the effect of the neighboring species and the presence of a dispersion medium is manifested in the Hamaker constant.[106, 111]

2.3.3.1.2 Electrostatic forces

If vdW forces are solely present among macroscopic particles dispersed in a fluid medium, most colloidal systems would be expected to undergo aggregation and/or sedimentation under the influence of vdW and gravitational forces. In many cases, however, such destabilization does not occur as evident in cosmetic products, milk, emulsion medications, etc. The high colloidal stability of numerous dispersed systems indicates the presence of some repulsive forces, whose magnitude well outweighs that of vdW forces, which explains why numerous colloidal systems are highly stable and remain so for days and often for years. Most substances, when introduced into aqueous media, acquire a surface charge that exerts a repulsive electrostatic effect among like-charged particles, preventing aggregation and system destabilization. Macroscopic particles acquire interfacial charge upon introduction into aqueous media via several charging mechanisms such as[112, 113]

1. Ionization or dissociation of surface functional groups (e.g., acidic/basic groups such as metal oxides).
2. Specific adsorption of ions from solution onto neutral surfaces.
3. Differential ion solubility (e.g., preferential dissolution of Ag^+ over Cl^- from AgCl crystals).
4. Isomorphous substitution of surface ions (e.g., replacement of Si within tetrahedral layers in clays by Al resulting in negative surface charge).

The acquired surface charge gives rise to a distribution of oppositely charged ions, called the *counter ions*, surrounding the charged surface. These two oppositely charged layers of surface charge and counter ions distribution form the *electrical double layer* (EDL) that, although electrically neutral, plays a fundamental role in the electrostatic stabilization of colloids via repulsion among similarly charged surfaces and attraction among oppositely charged ones. The distribution of counter ions close to charged surfaces has been the subject of several models, which are illustrated in **Figure 9** along the potential profile surrounding the particles. In the *Helmholtz model* (1853), the counter ions are firmly bound to the surface and form a fixed plane of opposite charge, called the outer Helmholtz plane (OHP), as shown in **Figure 9(a)**. The potential, Ψ, decreases linearly with the distance between the surface and the OHP. In the *Gouy-Chapman model* (1910-1913), shown in **Figure 9(b)**, the acquired surface charge is balanced by a diffuse atmosphere of counter ions, called the *diffuse layer*, within which Ψ decays exponentially from the surface to the boundary of the diffuse layer. The surface charge and the diffuse layer constitute the EDL.[78, 79]

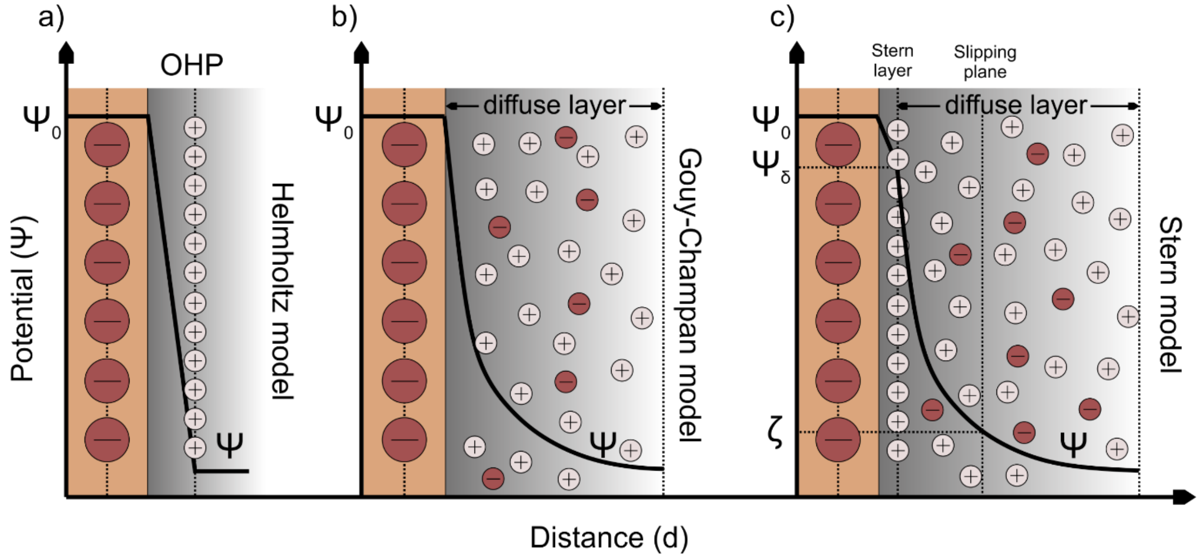

Figure 9. Schematic representations of the various models of the EDL at the solid-liquid interface. a) In the *Helmholtz* model, the counter ions are rigidly fixed at some distance from the surface, forming the outer Helmholtz plane (OHP). The potential varies linearly from the surface potential, Ψ_0, to the potential at the OHP, Ψ. b) In the *Gouy-Chapman* model, the charged surface gives rise to a cloud of diffuse distribution of counter ions, called the diffuse layer, within which the surface potential, Ψ_0, decays exponentially to the potential at the bulk solution, Ψ. c) The *Stern approximation* combines the two models. The Stern layer is the layer of surface-bound counter ions while the diffuse layer consists mostly of counter ions in diffuse and rapid thermal motion. The Stern potential, Ψ_δ, is the potential at the Stern layer. The slipping plane marks the special volume of the solution that is dynamically part of the solid particle (e.g., moves with the particle in Brownian motion and during electrophoresis), and the potential at the slipping plane is the electrokinetic or zeta (ζ) potential.

The *Stern model* (1942) combines the Helmholtz and Gouy-Chapman models, and thus, the counter-ion layer is suggested to comprise two parts: surface-bound counter ions (Stern or Helmholtz layer) and the diffuse atmosphere of ions in rapid thermal motion close to the surface (Gouy-Champan's diffuse layer). As shown in **Figure 9(c)**, the *Stern potential* refers to the potential at the *Stern layer*, the layer of counter ions that are tightly adsorbed onto the surface. Beyond the Stern layer is the diffuse layer of counter ions, within which the effective potential decays exponentially away from the Stern layer. Thus, the maximum potential occurs at the particle surface and reduces to zero at the boundary of the EDL, since it is electrically neutral. The *hydrodynamic sphere* is the volume of the dispersion, within the EDL, that is dynamically part of the particle during its motion. The boundary of the hydrodynamic sphere is marked by the *slipping plane*, and the potential at this plane is called the *electrokinetic* or *zeta potential*.[78] A modified version of the Stern model is the *Grahame model* (1947), where the Stern layer is further divided into two regions. The first region is comprised of specifically bound non-solvated ions, whereas the second region includes nonspecifically bound solvated ions, the latter region extends until the OHP, after which the diffuse layer is located.[114]

For planar surfaces in electrolyte solutions, the change in the electrostatic potential, ψ, away from the surface is quantitatively described by the Poisson-Boltzmann equation (PBE):

$$\nabla^2\psi = -\frac{e}{\varepsilon\varepsilon_o}\sum_i z_i c_i e^{\frac{-z_i e\psi}{k_B T}} \tag{11}$$

where ε_o is the permittivity of vacuum, ε is the dielectric constant of the medium, e is the elementary charge, c_i is the bulk number concentration of ion i, z_i is the valence of ion i, k_B is the Boltzmann constant, T is the absolute temperature.[79] The treatment of the PBE gives rise to several important relations that help to understand electrostatic stabilization in colloidal systems. These relations include the variation of electrostatic potential away from the surface and the relation between surface charge and surface potential. However, because the Poisson-Boltzmann equation is a non-linear second-order differential equation, it can be solved analytically only in certain cases. Thus, numerical solutions are more feasible to obtain. However, they largely depend on the surface geometry, the magnitude of the surface charge, the separation distance, the presence of the solvent, and the nature of the electrolyte. For *planar* surfaces in symmetrical (z:z) electrolytes, the potential at point x away from the surface, ψ_x, is given by:

$$\psi_x = \frac{2k_B T}{ze} log\left[\frac{1+\gamma e^{-\kappa x}}{1-\gamma e^{-\kappa x}}\right] \tag{12}$$

where

$$\gamma = \tanh\left(\frac{ze\psi_0}{4k_B T}\right) \tag{13}$$

$$\kappa^2 = \frac{\sum_i c_{\infty i} e^2 z_i^2}{\varepsilon\varepsilon_0 k_B T} \tag{14}$$

where $c_{\infty i}$ is the bulk number concentration and κ is the Debye parameter.[79, 106] The inverse of the Debye parameter, κ^{-1}, is the Debye length, which is a measure of the thickness of the EDL that solely depends on the properties of the solutions such as the ionic strength, the nature of the solvent, and the temperature. In addition, the PBE can be integrated once to establish a relationship between the surface potential and the surface charge. For instance, for planar geometry at large separation, the relationship between the surface charge density and the surface potential is

$$\sigma_0 = \pm\left[2k_B T\varepsilon\varepsilon_0 \Sigma_i c_i\left(e^{\frac{-z_i e\psi_0}{k_B T}} - 1\right)\right]^{1/2} \tag{15}$$

where ψ_0 is the surface potential.[115] For symmetric, mostly 1:1, electrolytes, the PBE can be solved analytically, and equation (15) reduces to the Grahame relation:[116]

$$\sigma_0 = \frac{2k_B T\varepsilon\varepsilon_0\kappa}{ze}\sinh\left(\frac{ze\psi_0}{2k_B T}\right) \tag{16}$$

As the two surfaces approach one other, their EDL overlaps, similarly charged surfaces will experience electrostatic repulsion whereas oppositely charged surfaces will attract one another. The EDL interaction potential depends on the geometry of particles as well as the experimental conditions. However, analytical solutions for the interaction potential are only possible in limited cases. For example, no simple expression for the EDL interaction potential exists for surfaces in mixed-valence electrolytes (e.g., 2:1, 1:3, etc.), but for z:z electrolytes, the EDL interaction potential energy per unit area, $V(x)_{EDL}$, between two similarly charged identical surfaces (infinite planes or spheres of radius R) is given by:[106]

$$V(x)_{EDL}^{planar} = \frac{64k_B T c_\infty \gamma^2}{\kappa} e^{-\kappa x} \tag{17}$$

$$V(x)_{EDL}^{spherical} = \frac{64\pi k_B T R c_\infty \gamma^2}{\kappa^2} e^{-\kappa x} \tag{18}$$

For surfaces with low surface potential (<25 mV) in 1:1 electrolyte, the PBE can be linearized and simplified to the Debye-Hückel (DH) equation:

$$\nabla^2\psi = \kappa^2\psi \tag{19}$$

The DH approximation enables analytical solutions for 1) the change in ψ_x with distance, 2) the surface charge-surface potential relation, and 3) the EDL interaction potential for spherical and planar geometries.[79, 106] Equations (20-24) show the simplified relations, obtained from the DH model.

$$\psi_x = \frac{R}{x}\psi_0 e^{-\kappa(x-R)} \qquad \text{for spherical surfaces} \tag{20}$$

$$\psi_x = \psi_0 e^{-\kappa x} \qquad \text{for planar surfaces} \tag{21}$$

$$\sigma_0 = \varepsilon\varepsilon_0\kappa\psi_0 \tag{22}$$

$$V(x)_{EDL}^{planar} = 2\varepsilon\varepsilon_0\kappa\psi_0^2 e^{-\kappa x} \qquad \text{valid for all electrolytes} \tag{23}$$

$$V(x)_{EDL}^{spherical} = 2\pi R\varepsilon\varepsilon_0\psi_0^2 e^{-\kappa x} \qquad \text{valid for all electrolytes} \tag{24}$$

The formation of stable colloidal systems of charged particles requires strong electrostatic repulsion forces that outweigh the vdW attraction, the above expressions indicate that experimental conditions such as low salt content, low ion valence, and solvent of high dielectric constant result in strong electrostatic repulsion, as evident by the expression of the Debye parameter. Also, for two similarly charged surfaces, the origin of electrostatic repulsion is *entropic* in nature. Indeed, for systems of no added electrolytes (i.e., counter ions solely originate from the surface), attractive Coulombic forces exist between surface-ionized functional groups and counter ions that can result in their re-association onto the surfaces. On the other hand, the osmotic repulsion among the counter ions results in the increase of their configurational entropy. Such increase maintains the diffuse configuration of the counter ions and keeps them away from the interacting surfaces and one another, giving rise to the diffuse layer. Thus, when two surfaces approach one another, the electrostatic attraction forces the counter ions onto the surface, but the dominant osmotic repulsion results in a net repulsive interaction, resulting in the formation of the EDL as a compromise between the two opposing effects. A similar argument can be extended to surfaces in electrolyte solutions, where, again, an electrostatic force component exists, but the dominant force is the osmotic repulsion among the counter ions, resulting in overall repulsive forces.

2.3.3.1.3 Polymer-mediated forces

The adsorption of polymeric macromolecules onto surfaces gives rise to additional forces that contribute to the (de)stabilization of colloidal systems (**Figure 8**). If the adsorbed polymeric chains on the particles are extended into their EDLs, the aggregation or the approach of two such surfaces is hindered by *steric repulsion* among the extended chains. Charged polymers (polyelectrolytes), on the other hand, result in *electrosteric interactions*, a combination of steric and electrostatic repulsions.[117] In both cases, if enough macromolecules exist on the surface, such polymer-mediated repulsion interactions are sufficient to keep particles separated, rendering vdW forces ineffective to cause particle aggregation. Like the EDL forces, the steric repulsion is *entropic* in origin since compressing the chains between the surfaces of the approaching particles gives rise to a repulsive osmotic force due to unfavorable entropic configurations.[109, 118] On the other hand, the simple adsorption of polyelectrolyte chains in a non-extending fashion results in electrostatic repulsion. However, for heterogeneous adsorption such as low particle coverage, attractive electrostatic interactions, known as *patch-charge interactions*, exist between the charged surface and patches of oppositely charged polyelectrolyte chains on the approaching surface.[119, 120] Also, the simultaneous adsorption of individual polymeric chains by several particles can result in weak and reversible aggregation, called *flocculation*, and gives rise to the *bridging forces*.[121] In addition, when adsorbed macromolecules are depleted from the surface or exist in a free state in the medium, the presence of these non-bound polymeric chains among interacting particles can have both stabilizing and destabilizing effects. When polymeric chains surround individual particles, they prevent their aggregation resulting in increased stability, such stabilization is called *depletion stabilization*. Nevertheless, the depletion zones of two particles can overlap, resulting in attractive depletion forces leading to aggregation, as shown in **Figure 8**.[122, 123]

2.3.3.1.4 Solvation forces

When two surfaces are a few nanometers apart, the long-ranged forces of vdW and EDL cannot fully describe the interaction potential, where the observed short-ranged forces at small separations are larger than either of the two long-ranged vdW and EDL forces.[124] Among the possible forces acting at short separation distances are the solvation forces. These short-ranged forces arise because of the re-structuring of solvent molecules in the gap between two approaching surfaces. Although arising when surfaces are only a few nanometers apart, force measurements indicate that solvation forces are larger than the vdW forces and are oscillatory in nature, i.e., varying between repulsive and attractive as the separation distance varies.[125, 126] Although, the origin of the repulsion in solvation forces is poorly understood, it is believed to occur due to the entropic confinement of mobile ions and the dehydration of the surface and the adsorbed ions.[125]

2.3.3.1.5 Hydrophobic interactions

The hydrophobic interactions refer to the unusually long-range and strong attractive interactions among hydrophobic surfaces in polar media such as water. Compared to vdW forces, hydrophobic interactions are found to be much stronger and of greater range, reported to be two orders of magnitude stronger than vdW for hydrophobic silica.[109, 127] Hydrophobic surfaces are characterized by the absence of polar or ionic groups as well as the inability to form hydrogen bonding. Since water molecules typically tend to form a structured network of clusters, such surfaces have unfavorable interactions with water molecules as they require entropically unfavorable orientations of the solvent molecules. Thus, as two hydrophobic surfaces are brought together, the increased free energy of water forces the molecules out of the gap between surfaces into the bulk, resulting in a strong attractive force among hydrophobic surfaces. Although several attempts were made to account for these interactions, the origin and characteristics of the hydrophobic interactions remain poorly understood.[109]

2.3.3.2 The Derjaguin-Landau-Verwey-Overbeek (DLVO) theory

The DLVO theory, named after scientists who developed it (Derjaguin and Landau, 1941; Overbeek and Verwey, 1948), is one of the earliest attempts to quantitatively describe colloidal stability in terms of interactions between the colloidal particles.[128, 129] According to this theory, the particle interactions and the resulting colloidal stability is largely governed by relative contributions of the vdW and the EDL forces. Thus, the total interaction potential energy, $V(x)_T$, is expressed as

$$V(x)_T = V(x)_{vdW} + V(x)_{EDL} \tag{25}$$

The attractive vdW forces always exist and are largely inherent to the nature and the physicochemical properties of the interacting surfaces whereas the electrostatic forces are highly sensitive to experimental conditions such as the pH, the ionic strength, the surface charge, and the nature of the solvent.[130, 131] Thus, when the overall contribution of the two forces is attractive, such as at high ionic strength or pH at the PZC, the particles undergo aggregation leading to destabilization of the colloidal system. Conversely, when conditions result in an overall repulsive interaction such as at low ionic strength, highly polar media, and high surface charge, e.g., highly (de)protonated inorganic nanoparticles; the colloidal system maintains high colloidal stability characterized by dispersed and well-separated particles. Since various expressions for vdW and EDL, depending on the geometry, potential, etc. as seen earlier; the final expression of $V(x)_T$ can be simply obtained by summing the corresponding individual expressions of vdW and EDL.[130] Thus, in a system of differently sized spherical particles of low potential and where R_1 and $R_2 \gg x$, the total interaction potential is the sum of the individual contributions of vdW and EDL forces, as shown below:

$$V(x)_T^{sphere} = -\frac{A}{6x}\frac{R_1R_2}{R_1+R_2} + 2\pi\frac{R_1R_2}{R_1+R_2}\varepsilon\varepsilon_0\psi_0^2 e^{-\kappa x} \tag{26}$$

Figure 10 shows the typical interaction potential of the vdW and EDL forces and the total interaction (the DLVO profile), as two similar particles approach each other (homoaggregate). The *primary minimum* represents a very strong attractive total interaction and indicates that vdW forces dominate at short separation. At slightly larger distances, on the other hand, the DLVO profile is characterized by the evolution of an energy maximum, called the *energy barrier*, representing a strong repulsive interaction, dominated by the EDL repulsion forces. At larger separation, the DLVO profile is characterized by a shallow attractive *secondary minimum*, which corresponds to interactions leading to weak and reversible aggregation such as flocculation.[132] At very small distances, strong non-DLVO repulsive forces, indicated by the dashed portion of the total interaction, arise due to the interaction among the electron clouds and are known as the Born repulsion.[133]

The height of the energy barrier and the depth of the primary and secondary minima provide insight into the magnitude of the individual forces involved. The total interaction potential of highly charged particles, for instance, is expected to be characterized by a high energy barrier indicating strong and long-ranged repulsion forces. Weakly charged particles, on the other hand, are expected to have a low energy barrier and undergo aggregation more rapidly. When the energy barrier is too high to overcome, the particles remain well-dispersed, even if the aggregation is thermodynamically favorable at the primary minimum. Such systems are referred to as *kinetically stable*.

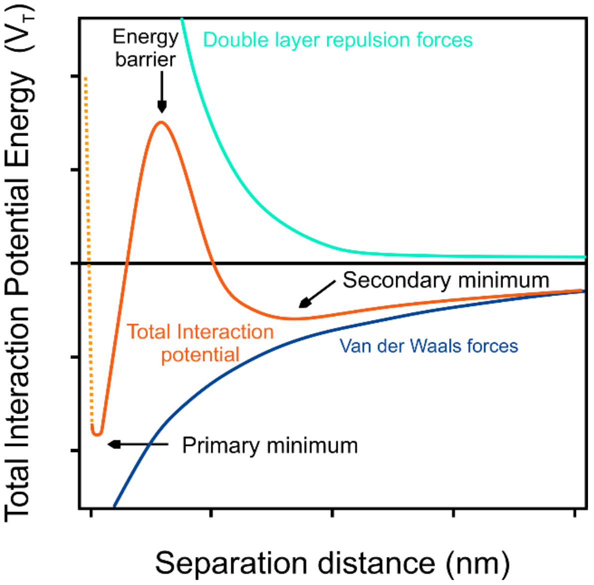

Figure 10. The total interaction potential (V_T) or the DLVO force profile as a function of the separation distance. The magnitude of V_T depends on the sum of the repulsive EDL and the attractive vdW forces. The dashed line refers to short-ranged non-DLVO repulsion, known as “Born repulsion”.

In multi-components colloidal systems, the aggregation among similar and dissimilar particles occurs simultaneously. The vdW interactions generally remain attractive but vary in magnitude since the Hamaker constant is different for dissimilar particles. Also, since dissimilar particles can have different surface charge densities, the interaction energies of EDL forces vary widely. For oppositely charged particles, the EDL forces between particles are always attractive. Hence, the DLVO profile for oppositely charged and dissimilar surfaces has no repulsive energy barrier since both vdW and EDL forces are attractive.[134, 135]

Despite its success, the DLVO theory has significant limitations resulting in discrepancies between theoretical predictions and experimental results. In the DLVO model, the vdW interactions are valid as long as the separation distances between colloidal particles are greater than atomic dimensions, and significant deviations are observed in the measured and predicted electrostatic interactions in systems of divalent electrolytes. In addition, discrepancies can also arise as a result of frequent assumptions involving oversimplification of the properties of real colloids such as smooth surfaces, uniform charge distribution, and ideal geometries. Also, the disregard of non-DLVO forces such as short-range repulsions, hydrogen bonding, hydrogen donor/acceptor reactions, hydration, and (electro)steric interactions can result in significant disagreement between theory and experiment. In some cases, however, various models of extended DLVO theory have been formulated to account for certain limitations such as surface roughness and the involvement of other forces such as steric or hydrophobic interactions.[136, 137]

2.3.4 Particle aggregation kinetics

2.3.4.1 Aggregation of similar particles (homoaggregation)

The DLVO theory enabled the determination of the various regimes of the interparticle forces, at which the colloidal stability of a given system can be qualitatively predicted. Since colloidal systems are constantly susceptible to aggregation, a quantitative description of the aggregation process is of special importance since control over colloidal stability is vital in numerous applications involving colloidal systems. Also, the course and the extent of the aggregation process are largely dependent on whether the net interaction is repulsive or attractive, which is determined by the total interaction potential of the system, as predicted by the DLVO theory.

The aggregation phenomenon can generally be divided into two aggregation phases. Initially stable suspensions are often assumed to be monodisperse in terms of the spatial distribution of primary particles. In the *early-stage* aggregation phase, the aggregation is dominated by the formation of dimers while in the *late-stage* aggregation phase, higher-rank aggregates (trimers, tetramer, etc.) are formed.[138] The occurrence of these two phases is expected to be influenced by the physicochemical properties of particles and the experimental conditions such as the pH, the ionic strength, and the particle concentration.

Figure 11(a) shows the change of the hydrodynamic radius over time when the particle concentration is raised at given pH and ionic strength. Stable systems (white region) exhibit no change in the hydrodynamic radius over time, which typically occurs in highly diluted systems. In addition, colloidal systems are said to exist in the early-stage aggregation if the aggregation statistically results in dimer formation (within a given time frame). For spherical particles, the hydrodynamic radius of the dimers was determined to be 1.38 times that of the comprising monomers, as estimated from the hydrodynamic interactions in fluids of low Reynold numbers.[139] As shown in **Figure 11(a)**, for diluted systems of spherical particles (green region), such a condition is met when the maximum increase in the hydrodynamic radius is around

~38%. The late-stage aggregation (gray region), on the other hand, results in a higher increase in the hydrodynamic radii due to the formation of large aggregates (**Figure 11(a)**). The late-stage aggregation frequently occurs in concentrated systems, in which subsequent phenomena such as sedimentation, creaming, and gel formation can be observed.[140, 141]

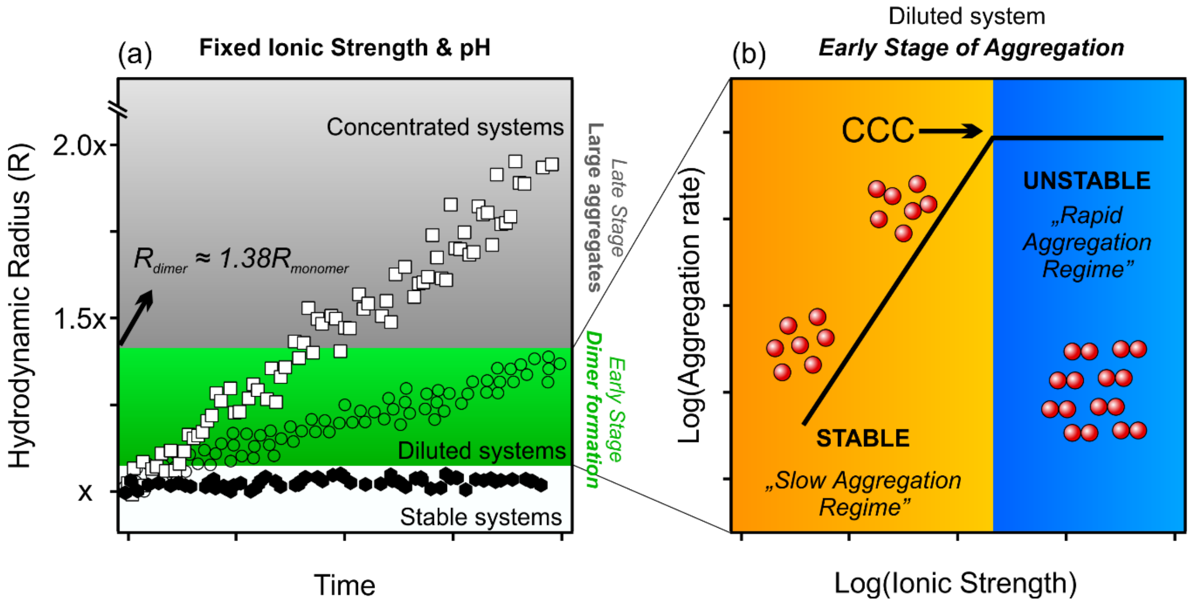

Figure 11. (a) The various phases of the aggregation process. The early-stage aggregation statistically involves the formation of dimers and mostly occurs in diluted systems. The late-stage aggregation, on the other hand, involves the formation of higher-rank aggregates and occurs in concentrated systems. At given pH and ionic strength, the change in the particle size over time is used to probe the different aggregation phases at various particle concentrations. (b) In the early-stage aggregation, the aggregation rate is affected by the salt level in the system. At low salt levels, the system is stable or very slowly dimerizes (slow aggregation regime), while at high salt levels, the dimer formation proceeds rapidly (rapid aggregation regime). The system transitions between the two regimes at a characteristic salt concentration, called the critical coagulation concentration (CCC).

In addition, two aggregation regimes exist within the early-stage aggregation. **Figure 11(b)** illustrates the course of early-stage aggregation (the green region in **Figure 11(a)**) when the salt-induced aggregation is probed by the systematic increase of ionic strength at a given pH and particle concentration. At low salt content, the colloidal system is generally stable or slowly aggregating into dimers. Such systems remain in the *slow aggregation regime* until the salt level reaches a certain value, called the critical coagulation concentration (CCC). When the ionic strength is larger than that at the CCC, the colloidal system transitions to the *rapid aggregation regime* where the dimer formation occurs very rapidly.

In the quantitative treatment of aggregation kinetics, a prime assumption is that the aggregation phenomenon is a second-order process, and thus, particle aggregation is brought about because of binary collisions. Hence, the number of collisions per unit time and volume,

J_{ij}, occurring between i and j particles, is expressed as follows:

$$J_{ij} = k_{ij} N_i N_j \tag{27}$$

where k_{ij} is the collision rate coefficient of primary particles while N_i and N_j refer to the number concentrations of i and j particles, containing i and j primary particles in the formed aggregates. The final form of this expression largely depends on the nature of the interaction forces in the system as well as the particle transport mechanism. When repulsive interactions are absent, the particles approach one another via diffusion. Using the Einstein-Stokes equation, Marian von Smoluchowski (1917) showed that k_{ij} for spherical i and j particles with radii R_i and R_j is

$$k_{ij} = \frac{2k_B \mathrm{T}}{3\eta} \frac{(R_i + R_j)^2}{R_i R_j} \tag{28}$$

where k_B is the Boltzmann constant, T is the absolute temperature, and η is the medium's dynamic viscosity. In the case of similarly sized particles, the collision rate no longer depends on the aggregate size and the k_{ij} becomes the *Smoluchowski rate constant*, k_s:[142] [143, 144]

$$k_s = \frac{8k_B \mathrm{T}}{3\eta} = 1.23 \times 10^{-17}\ m^3 s^{-1} \quad \text{at 25 °C} \tag{29}$$

In addition, Smoluchowski proposed an expression for the rate of change of k-fold aggregated particles:[142]

$$\frac{dN_k}{dt} = \frac{1}{2} \sum_{\substack{i+j \to k \\ i=1}}^{i=k-1} k_{ij} N_i N_j - N_k \sum_{k=1}^{\infty} k_{ik} N_i \tag{30}$$

In the development of this expression, all collisions are assumed to lead to irreversible aggregation. Also, the particles are assumed to be spherical, and the aggregation is a second-order process. The first term represents the rate of formation of aggregates formed as a result of collisions of i and j aggregates such that $i + j = k$, while the second term expresses the loss of k-fold aggregates by collisions with any other aggregates.[142]

In the *early-stage* aggregation, however, the aggregation is limited to the dimer formation of two primary particles in a second-order process, with a net loss of one particle. Hence, the Smoluchowski expression enables the determination of the change in the number concentration of primary particles, N_1, as well as the change in the total number of particles, N_T:

$$\left(\frac{dN_1}{dt}\right)_{t\rightarrow 0} = -k_{11}N_1^2 \tag{31}$$

$$\left(\frac{dN_T}{dt}\right)_{t\rightarrow 0} = -\frac{k_{11}}{2}N_1^2 \;\rightarrow\; \frac{dN_T}{dt} = -\frac{k_{11}}{2}N_T^2 \tag{32}$$

where N_T = N_1 + N_2.[143] By obtaining the integrated second-order rate law, and setting the final number concentration of particles as half of the initial one (N_0 = N_1 + $2N_2$), the expression of the aggregation half-time, $T_{1/2}$, the time required for half of the primary particles to aggregate into dimers, can be obtained:[142, 143]

$$T_{1/2} = \frac{2}{k_{11}N_0} \tag{33}$$

In the absence of an energy barrier, the aggregation is controlled solely by diffusion and the k_{11} is equivalent to the Smoluchowski rate constant, k_s, obtained using equation (29). On the other hand, when both attractive and repulsive interactions are present, only a fraction of collision will lead to aggregation, and thus, the slower aggregation rate is related to particle interactions by the Fuchs stability ratio, W, introduced by Nikolai Fuchs (1934), by treating the problem as particle diffusion in a force field.[108, 110, 145]

$$W = 2\int_0^\infty \frac{e^{\frac{V_T}{k_BT}}}{(2+u)^2}\,du \tag{34}$$

where V_T is the total interaction potential and

$$u = \frac{2x}{R_i + R_j}$$

The magnitude of the stability ratio is directly proportional to the colloidal stability of the corresponding systems. Stable colloidal systems are characterized by very high stability ratio values while unstable and rapidly aggregating colloidal systems have low stability ratio values close to one.

2.3.4.2 *Quantitative assessment of colloidal stability*

Experimentally, the state of colloidal systems is often characterized by dynamic (DLS) and electrophoretic (ELS) light scattering.[142] The DLS technique is used to obtain the hydrodynamic radius, R_h, and the particle size distribution of colloidal particles and polymers in solutions, while ELS is used to obtain the electrophoretic mobility and the electrokinetic (zeta) potential of charged particles. **Appendix B** details the theoretical background and data acquisition of both scattering techniques. Moreover, during the time-resolved DLS, the aggregation rate can be quantitatively determined by monitoring the change in hydrodynamic radii of particles over time. The *apparent aggregation rate constant*, k_{app}, can be obtained from the time-resolved DLS measurements using the following expression:[139]

$$k_{app} = \frac{1}{R_{h(0)}} \cdot \left(\frac{dR_h(t)}{dt}\right)_{t\to 0} \tag{35}$$

where N_0 is number particle concentration (in m^{-3}), $R_{h(0)}$ is the hydrodynamic radius of the monomer particles, and $\frac{dR_h(t)}{dt}$ is the slope of the linear fit of the R_h-time data for the system under study. Then, the stability ratio, W, can be experimentally determined via the time-resolved DLS by obtaining the ratio of the experimentally obtained rate constants.[146]

$$W = \frac{k_{app(fast)}}{k_{app}} \tag{36}$$

The $k_{app(fast)}$ can be measured by determining k_{app} at diffusion-controlled conditions at high ionic strengths where no energy barrier exists, i.e., no repulsive electrostatic forces. Since the magnitude of the stability ratio is directly proportional to the colloidal stability of the system under study, the salt-induced aggregation measurements, where the ionic strength is changed, can be carried out to obtain the CCC from the stability ratio-ionic strength data using the following expression:

$$W = 1 + \left(\frac{CCC}{c_{electrolyte}}\right)^{\beta} \tag{37}$$

where $c_{electrolyte}$ is the bulk electrolyte concentration (in mol/L) and β is obtained from the stability ratio values in the slow aggregation regime as follows:[147]

$$\beta = \frac{dlog(\frac{1}{W})}{dlogc_{electrolyte}} \tag{38}$$

A step-by-step explanation of how to obtain the CCC from experimentally determined stability ratio-ionic strength data is illustrated in **Appendix C**.

2.3.4.3 Aggregation of dissimilar particles (heteroaggregation)

In colloidal systems of two or more components, the aggregation among similar particles (i.e., homoaggregation) can take place in parallel to heteroaggregation, the aggregation among different particles.[148] Since most naturally occurring and industrial colloidal systems are multi-components in nature, heteroaggregation is a fundamental colloidal phenomenon and occurs frequently between components of different chemical composition, surface charge, morphology, and size.[149] Depending on the application of interest, the heteroaggregation may be an undesired process in such fields as pharmaceuticals and paint. On the other hand, aggregation is often deliberately induced as part of the manufacturing processes in several industries such as rubber-making and leather tanning.[86, 87] In addition, the coagulation of dissimilar components has been widely used in the treatment of industrial wastewater (effluents) in several industries and fields including leather, mining, power generation, and paints.[150, 151]

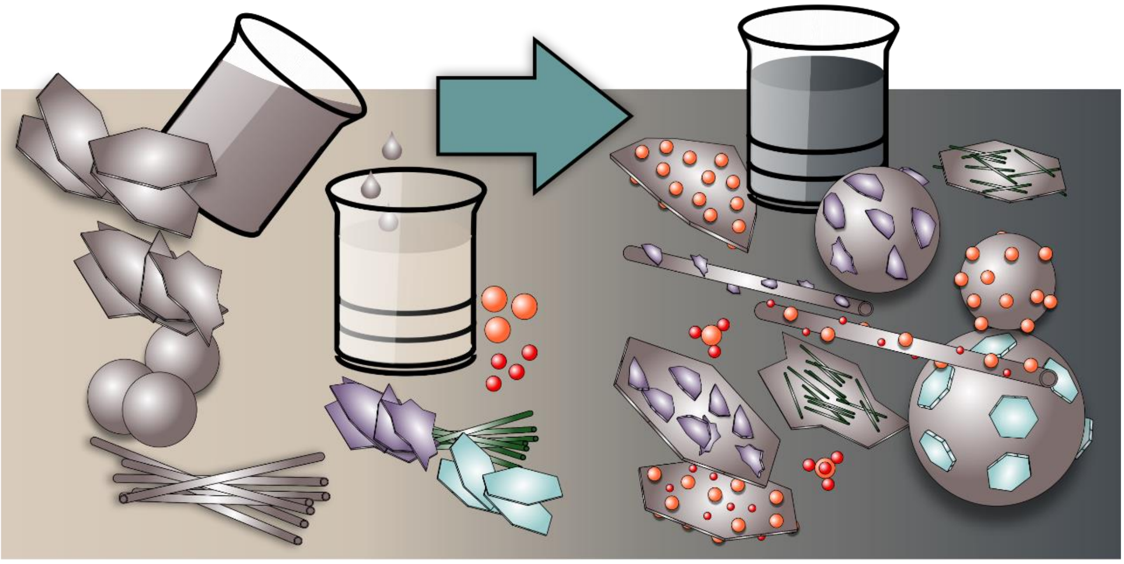

Figure 12. A Schematic illustration of heteroaggregation of particles of various sizes and shapes, where the aggregation of different particles is initiated by careful manipulation of the experimental conditions, and thus, the variation of the interparticle forces.

Most importantly, however, the controlled heteroaggregation between nanostructured materials (e.g., nanospheres, nanoplates, or nanotubes) has been used in the preparation of highly functional composite material with diverse structures and numerous applications potentials such as catalysis, drug delivery, water purification, artificial enzymes, and energy storage, among others.[152-155] Such engineered hybrid materials have been prepared via both *in situ* (by preparation of one material in the presence of another) or *ex-situ* heteroaggregation (direct aggregation of pre-synthesized particles by simple mixing of the respective dispersions). The heteroaggregation is illustrated in **Figure 12**; in both cases, the aggregation of dissimilar particles is induced by careful manipulation of experimental conditions, and thus, the optimization of the interparticle forces. Like homoaggregation, dissimilar particles form heteroaggregates via DLVO and non-DLVO forces including vdW, electrostatic, and bridging forces.[156] Several fundamental studies have probed the interactions between dissimilar particles, these include heteroaggregation of oppositely charged polystyrene latex particles, as well as heteroaggregation among metal oxides including ZnO and CuO and between SiO_2 and Al_2O_3.[157-159] Compared to homoaggregation, though, the heteroaggregation has not been studied to the same extent due to the difficulty in either theoretical or experimental approaches. For example, Lin et al. proposed an approach for distinguishing heteroaggregation and homoaggregation to determine the heteroaggregation rate constants. However, the approach is only valid for systems of particles with identical size and composition but different surface properties.[160] Thus, the heteroaggregation process remains quantitatively poorly understood due to the limitations of existing theories and their underlying assumptions.

3 Objectives

In the work pertaining to this dissertation, we aspire to deliver multi-functional composites with antioxidant potential. The composites are formed by the systematic and controlled heteroaggregation of inorganic nanozymes (Prussian blue, MnO_2, and CeO_2) with amidine- (AL) and sulfate- (SL) functionalized polystyrene latex beads. The latex-nanozyme composites are foreseen to mimic such antioxidant enzymes as SOD, CAT, and HRP enzymes. Also, the heteroaggregation is expected to occur under the influence of electrostatic and van der Waals attractive forces after systematic optimization of the experimental conditions.

Initially, the colloidal properties (the aggregation status, the particle size, and the zeta potential) of nanozymes and latex were probed at various pH, ionic strength, and concentration conditions to determine the optimal aggregation conditions, where the electrostatic attractive forces are maximized and homoaggregation is prevented to allow the effective formation of composites of robust stability and antioxidant potential.

In addition, when the particles to be heteroaggregated, i.e., latexes and nanozymes, are similarly charged at the optimal pH conditions, the surface charge on the nanozymes is modified with the adsorption of an oppositely charged polyelectrolyte prior to their heteroaggregation with the relevant latex. Here, a positively charged polyelectrolyte, named PDADMAC or poly(diallyldimethylammonium chloride), is used to surface-modify the charge of the metal oxides (MnO_2 and CeO_2). The proper dose of the PDADMAC is carefully determined by observing the colloidal properties (aggregation rate and zeta potential) at various PDADMAC doses, where the proper dose shall bring about highly positively charged metal oxide particles that are foreseen to effectively heteroaggregate with negatively charged SL.

Next, the formulation of the latex-nanozyme composite was achieved by heteroaggregation of the components under the assessed experimental conditions (pH, ionic strength, PDADMAC dose, and latex concentrations). Similar to the adsorption process, the amount of nanozyme to be immobilized on the latex is expected to largely affect the stability of the resulting composites, and thus, the aggregation rate and zeta potential of the latex-nanozyme composite is assessed at various nanozymes doses, where the optimal dose is expected to give rise to highly charged hybrid particles with high stability ratio.

Finally, standardized assays were used to examine the antioxidant activities of the formulated composites including SOD, CAT, and HRP enzymes, as well as the potential to reduce the 2,2-diphenyl-1-picrylhydrazyl (DPPH) radical.

4 Experimental Section

The current section details the experimental aspects of the measurements performed including the instrumental methods, procedures of material synthesis, procedures pertaining to nanoparticles functionalization and composite formation, qualitative and quantitative description of the enzymatic assays followed during the assessment of the enzyme-like potential of the bare nanozymes and their corresponding composites.

4.1 Reagents and precursors

Table 2 lists the details of reagents and precursors used for material synthesis as well as various measurements. The chemical grade and purity are provided when available. In addition, **Table 3** lists other accessories used throughout the experimental work.

Table 2: Reagents and precursors used during material synthesis, composite formulation, and assessment of the enzyme-like potential.

Material	Form	Grade	Purity	Supplier
Hydrochloric acid	HCl	AnalaR NORMAPUR	37% m/m	VWR™
Sodium hydroxide	$NaOH$	AnalaR NORMAPUR	≥99.3%,	VWR™
Hydrogen peroxide	H_2O_2	N/A	30% m/m	VWR™
Sodium chloride	$NaCl$	N/A	99.9%	VWR™
Ethanol	CH_3CH_2OH	AnalaR NORMAPUR	absolute	VWR™
Ammonia solution	NH_4OH	AnalaR NORMAPUR	25%	VWR™
Methanol	CH_3OH	AnalaR NORMAPUR		VWR™
Dimethyl sulfoxide	C_2H_6OS	AnalaR NORMAPUR		VWR™
Ethylene glycol	$C_2H_6O_2$	AnalaR NORMAPUR	95%	VWR™
Cerium (III) nitrate hexahydrate	$Ce(NO_3)_3\cdot 6H_2O$		99.5%	Acros Organics™
*PDADMAC	$(C_8H_{16}NCl)_n$		20% m/m	Sigma-Aldrich
*TMB	$C_{16}H_{20}N_2$		≥99%	Sigma-Aldrich
*DPPH	$C_{18}H_{12}N_5O_6$		95%	Alfa Aesar
Acetic acid	CH_3COOH	Ph.Eur./USP	glacial	VWR™
Sodium acetate trihydrate	$NaCH_3COO\cdot 3H_2O$		≥99.5%	VWR™
Disodium phosphate	Na_2HPO_4	GPR RECTAPUR®	≥99%	VWR™
Monosodium phosphate	NaH_2PO_4		99%	Acros Organics™
*TRIS	$C_4H_{11}NO_3$	AnalaR NORMAPUR		VWR™
Acetone	C_3H_6O		99.8%	VWR™
Potassium persulfate	$K_2S_2O_8$	AnalaR NORMAPUR	98%	VWR™
Potassium permanganate	$KMnO_4$	Reagent grade	99%	Acros Organics™
*NBT	$C_{40}H_{30}Cl_2N_{10}O_6$		90%	Acros Organics™
Styrene	C_8H_8		99%	Acros Organics™
Polyvinylpyrrolidone	$(C_6H_9NO)_n$			Acros Organics™
Oleic acid	$C_{18}H_{34}O_2$	Technical grade	99%	Sigma-Aldrich
Xanthine oxidase	enzyme		0.4–1.0	Sigma-Aldrich
Xanthine	$C_5H_4N_4O_2$		99%	Alfa Aesar
*AL	$(C_8H_8)_n$		4% w/v	Invitrogen™
Potassium chloride	KCl		≥99.5%	VWR™
Potassium ferricyanide	$K_3[Fe(CN)_6]$		≥99.0%	VWR™
Iron (II) chloride tetrahydrate	$FeCl_2\cdot 4H_2O$		≥99%	Acros Organics™
Guaiacol	$C_7H_8O_2$		99%	Acros Organics™

***PDADMAC**: Poly(diallyldimethylammonium chloride), **TMB**: 3,3',5,5'-Tetramethylbenzidine, **DPPH**: 2,2-diphenyl-1-picrylhydrazyl, **TRIS**: Tris(hydroxymethyl)aminomethane, **NBT**: Nitro blue tetrazolium chloride, **AL**: Amidine-functionalized polystyrene latex.

Table 3: Accessories used during material synthesis, composite formulation, and assessment of the enzyme-like potential.

Accessory	Remarks	Supplier
Helmanex	Glassware cleaning agent	Hellma
Puranity TU 3 UV/UF+ system	Ultrapure water supply	VWR™
PVDF-based syringe filters (0.1 μm)	Filtration of ultrapure water	MILLEX-VV
Spectra/Por® 6	Dialysis membrane tubing	SpectrumLabs

4.2 Instrumental methods

4.2.1 X-ray photoelectron spectroscopy

The X-ray photoelectron spectroscopy (XPS) analysis of synthesized nanozymes was carried out using the SPECS™ instrument. The Al Kα X-ray source was operated at 14 kV and 150 W. The PHOIBOS 150 MCD 9 hemispherical analyzer was run in fixed-analyzer transmission mode. The pass energies for the survey and high-resolution scanning were set at 40 eV and 20 eV, respectively. A small sample of the material under study was pressed into a piece of indium foil and loaded into the main chamber (operated under a pressure range of 10^{-9}-10^{-10} mbar) on the Au-coated sample holder. Using surface adventitious carbon (284.8 eV) for charge referencing, the XPS data were evaluated using the commercial CasaXPS software package.

4.2.2 X-ray diffraction

The X-ray diffraction (XRD) patterns were obtained for CeO_2 NPs using Bruker D8 Advance diffractometer. The Cu Kα source provides an incident monochromatic beam with a wavelength of 1.5406 Å. The XRD diffraction patterns were recorded at 5°/min over a 2θ range of 20°-80° and were further compared with the standard reference patterns of the Joint Committee on Powder Diffraction Standards (JCPDS) databases of the International Center for Diffraction Data.

4.2.3 Electrophoretic light scattering

Zeta potential values were determined via the ELS technique using the Anton Paar Litesizer™ 500 device, equipped with a 658-nm laser source (40 mW). The applied voltage was kept at 200 V throughout all ELS measurements, and the scattered light was collected in backscattering mode and analyzed using the phase analysis technique.[161] After the sample preparation, the samples were allowed to equilibrate for 120 min at room temperature before the measurement. To obtain the zeta potential, 750 μL was withdrawn from the sample under study and introduced into an omega cuvette (Anton Paar™). The zeta potential measurement was then performed at 25.0±0.2 °C and reported as an average of 6-8 runs.

4.2.4 *Dynamic light scattering*

The aggregation rates were obtained using the ALV-NIBS/HPPS Particle Sizer, equipped with a 632.8-nm laser source. Also, the hydrodynamic radii were obtained using the Anton Paar Litesizer^{TM} 500, equipped with a 658-nm laser source. The scattered light was collected at 173^{o}, and the data analysis was based on the cumulant fit.[139] The aggregation rate measurements were initiated immediately upon the addition of the desired volume of the last component in the sample under study. The final volume for all samples is 2.0 mL. Also, the aggregation rates and hydrodynamic radii were obtained at 25.0 ± 0.2 °C using disposable polystyrene cuvettes. The hydrodynamic radius results were reported as an average of 30-50 runs. On the other hand, during time-resolved DLS, the change in the hydrodynamic radius over time was recorded (containing 30-100 measurement points) to obtain k_{app}, W, and $T_{1/2}$ using equations (35), (36), and (33), respectively.

4.2.5 *Electron microscopy*

The morphology of bare nanozymes as well as the formulation of the composites were probed via scanning electron microscopy (SEM, Hitachi S-4700) and transmission electron microscopy (TEM, FEI Tecnai G^2-20-X-TWIN). During the preparation of TEM samples, small aliquots (~5 μL) were withdrawn from the dispersion of interest and introduced on a Cu-coated carbon mesh in a drop-wise fashion, with each aliquot left to adsorb for 10 seconds before the addition of more material. To ensure complete evaporation of the solvent, the samples were prepared at least 30 min before imaging. As for SEM samples, 5-μL volumes from the dispersion of interest were introduced onto the sample holder, which is comprised of a silicon wafer on a disk of aluminum, and were left to dry for at least 10 min. Since SEM requires conductive specimens, the sample holder was coated with Au thin film via the sputtering technique to enable SEM imaging.

4.2.6 *Atomic force microscopy*

The atomic force microscopy (AFM) images were obtained via the tapping mode at room temperature using a Multimode Nanoscope IIIa AFM microscope (Digital Instruments, USA). The Si-tip cantilever (Veeco Nanoprobe Tips) was operated with a resonance frequency of 275–300 kHz. Height and amplitude AFM images were simultaneously obtained at a scan rate of 1.0 Hz. The Gwyddion software was used for image analysis. As for the sample preparation, small aliquots of dispersions were deposited on a freshly cleaved mica (Ted Pella, Highest Grade V1) and were left to dry at room temperature prior to imaging.

4.2.7 Raman spectroscopy

The formation of CeO_2 NPs and their composites were confirmed via recording and comparing the Raman spectra of bare and immobilized CeO_2 NPs. The spectra were recorded with Bruker Senterra II Raman microscope, equipped with a laser source (100 mW) with a wavelength of 785 nm. The results were reported as an average of 128 spectra with 6.0 s exposure time.

4.2.8 UV-Vis spectrophotometry

The spectrophotometric technique (GENESYS^{TM} 10S, Thermo Fischer Scientific) was used to characterize nanozymes as well as observe the change in absorbance of the relevant chemical species during the assessment of the enzyme-like catalytic potential. The enzymatic assays typically involve the use of indicator compounds that change color due to significant alteration in chemical structures, these changes result in notable changes in their absorption spectra that can be indirectly used to qualitatively assess the enzyme-like catalytic potential.

4.3 Synthesis of nanozymes and latex beads

4.3.1 Synthesis of Prussian blue nanoparticles (PB NPs)

PB NPs ($Fe_4[Fe(CN)_6]_3$) were prepared by the co-precipitation of ferrous ($FeCl_2$) and ferric ($K_3[Fe(CN)_6]$) salts.[162] Using Hellmanex® III and concentrated HCl solution, the glassware was rigorously cleaned and washed with a copious amount of ultrapure water. Then, 100 mL of $K_3[Fe(CN)_6]$ solution (1.0 mM) was added dropwise to 100 mL of $FeCl_2$ solution (1.0 mM) under vigorous magnetic stirring. The color of the mixture slowly developed into dark blue as more $K_3[Fe(CN)_6]$ was added. Then, 400 mL of acetone was added to the resulting blue dispersion, and the solid PB was collected by centrifugation at 9,000 rpm for at least 30 min and washed using acetone. The centrifugation step was repeated until all material was retrieved. The solid PB was then dispersed in a proper volume of ultrapure water to obtain a 10.0-g/L stock dispersion.

4.3.2 Synthesis of manganese (IV) oxide microflakes (MnO_2 MFs)

The MnO_2 MFs were prepared by a redox procedure.[163] After a thorough cleaning of glassware, a 0.013 M $KMnO_4$ solution was prepared by dissolving 1.0 g of $KMnO_4$ in 500 mL of ultrapure water followed by vigorous stirring of the purple solution for 30 min. Then, the formation of MnO_2 MFs was initiated by the addition of 10.0 mL of oleic acid to the $KMnO_4$ solution, maintained at 28 °C, and the resulting mixture was then left under vigorous agitation for 5 h at the same temperature. After 5 h, the black MnO_2 solid was retrieved by centrifugation and subsequent washing with water and ethanol to remove unreacted components. The obtained solid precipitate was then dried at 80 °C for 10 h. After that, the prospective MnO_2 solid was dispersed in an adequate volume of ultrapure water to obtain a 10.0-g/L stock.

4.3.3 Synthesis of cerium (IV) oxide nanoparticles (CeO_2 NPs)

Initially, glassware was vigorously cleaned with Hellmanex® III and concentrated HCl solution. The CeO_2 NPs were synthesized according to the reported procedures.[164] First, 7.8 mL of 95%-ethylene glycol was added to 92 mL of ultrapure water followed by 5.16 g of $Ce(NO_3)_3.6H_2O$, and the pH of the mixture was adjusted to 9.6, by the careful addition of NH_3. The reaction was left under mild stirring at 50 °C, where the reaction mixture gradually developed a yellow color, signaling the formation of CeO_2 NPs. The yellow solid was retrieved by centrifugation and subsequent washing with ethanol and water. The solid was then left overnight at room temperature to allow the complete evaporation of the solvents. The yellow CeO_2 solid was dispersed in a proper volume of ultrapure water to obtain a 10.0-g/L stock.

4.3.4 Synthesis of functionalized polystyrene latex particles

The AL particles were commercially obtained with a mean diameter of 510 ± 2 nm. On the other hand, the SL particles were prepared by emulsifier-free emulsion polymerization.[165] Initially, 60.5 mg poly(vinylpyrrolidone) (PVP) and 12.1 g styrene were mixed in 100 mL of deionized water in a 250-mL round bottom flask, kept under N_2 atmosphere. The three-neck flask was connected to a reflux setup and was then immersed in an oil bath, maintained at 25 °C. After that, the mixture was stirred at 400 rpm for 30 min, during which the temperature was progressively increased to 70 °C. The polymerization was then initiated by the introduction of 300 mg of $K_2S_2O_8$ (dissolved in 20 mL of deionized water), where the reaction was left at 70 °C for 24 h. After that, the mixture was allowed to cool to room temperature, and the unreacted styrene and PVP were removed by repeated washing, centrifugation, and re-dispersing, where the product was washed using ultrapure water and ethanol. The product mixture was then dialyzed against water for 24 h and the final SL concentration was set at 50 g/L, obtained by properly diluting the original mixture.

4.4 Structural and colloid characterization

After synthesis, the identity and the chemical composition were initially characterized for each of the prepared nanoparticles (PB NPs, MnO_2 MFs, CeO_2 NPs) via several techniques such as XPS and XRD, as well as Raman and UV-Vis spectroscopy. The AFM, SEM, and TEM techniques were utilized to probe the morphology of the synthesized particles at the condition of interest. In addition, for nanoparticles and support materials (AL and SL), initial characterization of the surface properties is deemed necessary to obtain information on the aggregation tendencies upon introduction in aqueous media, i.e., the changes in the aggregation status with two of the most characteristic parameters of aqueous systems, the pH and the ionic strength. The obtained trends are expected to provide a vital starting point to set the optimal experimental conditions for the effective heteroaggregation of the comprising particles and subsequent formulation of robust composite materials.

4.4.1 The optimization of the pH conditions

The origin of the surface charge in metal oxides is attributed to the deprotonated surface hydroxyl and carboxyl groups. If significant surface charging occurs, the generated electrostatic repulsion prevents particle aggregation giving rise to stable systems. Hence, in the pH-dependent surface charging measurements, the dependence of hydrodynamic radius and zeta potential on the pH is probed at constant ionic strength to determine the optimal pH conditions for the SL and nanozymes. For each material, equally concentrated acidic (pH 3.0) and alkaline (pH 11.0) stock dispersions were prepared. After that, a series of secondary dispersions was prepared by systematic mixing of the two stocks so that the pH of the secondary dispersions incrementally spans the pH range of 3-11. The purpose of such a procedure is to maintain constant material concentration and ionic strength while solely changing the pH of the medium. In fact, the ionic strength is automatically fixed at 1.0 mM in the secondary dispersions since the acidic and basic stocks have identical p-values for hydroxide (pOH 3.0) and hydronium (pH 3.0) ions, respectively. The pH in the secondary dispersions was then unambiguously measured and the dispersions were left to equilibrate for 120 min prior to DLS and ELS measurements. For each secondary dispersion, the obtained hydrodynamic radius and zeta potential data were then plotted as a function of the pH. The stocks of nanozymes are prepared as follows: 100 mg/L **PB**, 125 mg/L **SL**, 50 mg/L **MnO_2**, and 50 mg/L **CeO_2**. The commercially obtained AL particles were not characterized for pH-dependent surface charging.

4.4.2 The optimization of the latex concentration

The optimal concentration of SL or AL particles is established by probing particle aggregation over time using time-resolved DLS.[166] Precisely, the change in the hydrodynamic radius over time in 2.0 mL samples was probed at different SL or AL concentrations (1-200 mg/L). The ionic strength was fixed at 1.0 M (using KCl for AL and NaCl for SL), at pH conditions determined from prior measurements. The optimal concentration of the support particles could be obtained by comparing k_{app} and $T_{1/2}$ values at the corresponding particle concentration, these two parameters can be obtained using equations (35) and (33), respectively. As established earlier, the presence of high salt levels leads to significant charge screening and weakens the electrostatic forces, resulting in diffusion-controlled homoaggregation under the influence of the vdW forces. Thus, in each of the 2.0-mL samples, 1.0 mL was withdrawn from the 2.0-M salt solution and added to a certain complementary volume of filtered water; after that, a certain volume of AL or SL dispersion was added immediately prior to running the time-resolved DLS measurements.

4.4.3 The salt-tolerance of latex and nanozyme systems

The trends in the homoaggregation of individual particles (latex and nanozymes) induced by the presence of progressively increased salt level (KCl for AL, and NaCl for SL, CeO_2 NPs, and MnO_2 MFs) was probed using ELS and time-resolved DLS to obtain the zeta potential and stability ratio values, respectively. By fixing particle concentrations and changing the ionic strength up to 1.6 M, the salt tolerance of the colloidal systems can be evaluated in a series of samples of systematically increased salt concentrations. In each of the 2.0-mL samples, a certain volume of salt was added to a certain complementary volume of filtered water, after that, the volume of particle dispersion is added immediately prior to running the time-resolved DLS measurements. Similar samples were similarly prepared and left to equilibrate for 2 hours before the ELS measurements to obtain the zeta potential values. The stability ratio and zeta potential values are graphed against the corresponding ionic strength. The final concentration of particles is set as follows: 25 mg/L **AL**, 125 mg/L **SL**, 100 mg/L **MnO_2**, and 100 mg/L **CeO_2**.

4.5 Functionalization of MnO_2 MFs or CeO_2 NPs

For MnO_2 MFs or CeO_2 NPs, the preparation of latex-nanozyme composites is achieved by heteroaggregation of negatively charged SL particles with oppositely charged MnO_2 MFs or CeO_2 NPs. Both metal oxides, however, have a negative surface charge at the optimal pH, and hence, the formation of the composites requires surface charge modification by surface functionalization with positively charged PDADMAC.

The optimal PDADMAC dose was determined by the systematic increase in the PDADMAC concentration in a series of nanozyme/PDADMAC dispersions. The pH, ionic strength, and nanozyme concentration we fixed at 9.0, 1.0 mM, and 100 mg/L, respectively. The PDADMAC dose (mg PDADMAC/g nanozyme) was gradually changed between 0.01 and 1,000 mg/g (for CeO_2 NPs) and 0.1 and 1,000 mg/g (for MnO_2 MFs). The ELS and time-resolved DLS were used to measure the zeta potential and aggregation rates of the PDADMAC-functionalized MnO_2 MFs (PMn) and PDADMAC-functionalized CeO_2 NPs (PCe). **Table 4** lists the experimental conditions for the functionalization of the metal oxides. During sample preparation, after the addition of nanozyme, salt, and a complementary volume of ultrapure water, the PDADMAC is introduced immediately prior to the time-resolved DLS measurement. For zeta potential, measurements were performed 120 min after the sample preparation. The PDADMAC doses resulting in highly positively charged PCe and PMn particles are selected for further heteroaggregation with SL.

Table 4: The experimental parameters for the functionalization of MnO_2 MFs and CeO_2 NPs at the designated experimental conditions.

System	Nanozyme	Polyelectrolyte	$C_{Nanozyme}$	pH	Ionic strength	Salt
PMn	(-)-MnO_2 MFs	(+)-PDADMAC	100 mg/L	9.0	1.0 mM	NaCl
PCe	(-)-CeO_2 NPs	(+)-PDADMAC	100 mg/L	9.0	1.0 mM	NaCl

4.6 Heteroaggregation & composite formation

Four prospective antioxidant composites were formulated via heteroaggregation of oppositely charged particles, these are listed in **Table 5** along with the comprising components as well as the pH and ionic strength conditions.

Table 5: The experimental parameters for the composite formulation at the designated experimental conditions.

Composite	Nanozyme	Latex	C_{latex}	pH	Ionic strength	Salt
AL-PB	(-)-PB NPs	(+)-AL	25 mg/L	4.0	1.0 mM	KCl
SPMn	(+)-PMn	(-)-SL	125 mg/L	9.0	1.0 mM	NaCl
SL-CeO_2	(+)-CeO_2 NPs	(-)-SL	125 mg/L	4.0	1.0 mM	NaCl
SPCe	(+)-PCe	(-)-SL	125 mg/L	9.0	1.0 mM	NaCl

For each composite, the heteroaggregation was realized by mixing proper volumes of the nanozyme and support dispersions along with a certain volume of salt solution to fix the ionic strength. The proper mass ratio of the components was established by probing the colloidal properties during and after the heteroaggregation process at various mass ratios, expressed in the nanozyme dose (in mg nanozyme/g latex). In each of the 2.0-mL samples, the latex concentration was kept constant (25 mg/L **AL** and 125 mg/L **SL**) while the nanozyme doses were changed as follows: 1) 1-1,000 mg PB/g AL, 2) 0.01-1,000 mg PMn/g SL, 3) 0.1-10,000 mg CeO_2/g SL and 4) 0.1-1,000 mg PCe/g SL. The ELS and time-resolved DLS were used to measure the zeta potential and aggregation rate, respectively, in the formulated composites. The trends in the aggregation rate were obtained during the heteroaggregation process, i.e., immediately after preparing the sample, while the zeta potential was obtained 120 min after sample preparation. During the preparation of the 2.0-mL samples, the last component to be introduced was the nanozyme (after the latex, salt, and a complementary volume of ultrapure water). The dispersions of PMn and PCe were prepared with the doses selected during the PDADMAC adsorption measurements, during which highly positively charged PCe and PMn particles were obtained.

4.7 Assessment of the enzyme-like activity

The current section details the underlying principles of the enzymatic assays including the experimental design, the reagents used, the interpretation of the results, and the assessment of the enzymatic activity using the UV-Vis spectrophotometry.

4.7.1 Assessment of the SOD-like activity (the Fridovich assay)

The SOD enzyme is an antioxidant ROS scavenger responsible for bio-catalyzing the breakdown of superoxide ($\bullet O_2^-$) to H_2O_2 and O_2. The assessment of the SOD-like activity of nanozymes is performed using the Fridovich assay.[167]

As shown in **Figure 13**, the superoxide is generated by the oxidation of xanthine, catalyzed by xanthine oxidase. The presence of superoxide is detected using the indicator compound nitro blue tetrazolium chloride (NBT), which is a yellow compound that develops a sharp purple color upon the reduction reaction with superoxide. The purple product, called formazan, exhibits a UV-Vis spectrum characterized by a strong absorption band around 565 nm. Thus, in the absence of the SOD-mimicking nanozymes, the complete NBT reduction reaction will result in strong absorption around 565 nm. However, when SOD-mimicking nanozymes are present, a proportion of the superoxide is eliminated, resulting in the incomplete reduction of the NBT. Hence, the NBT-superoxide reaction is partially inhibited as a result of the ROS scavenging action, resulting in weaker absorption and decreased purple color intensity, depending on the mimicking potential of the nanozyme.

The UV-Vis spectrophotometry is used to monitor the extent of inhibition. During the Fridovich assay, the development of the formazan absorption peak at 565 nm over time is observed at different nanozymes concentrations. Thus, in each of the 3,000-μL samples, a certain volume of nanozymes dispersion was added to 200 μL of a 3.0-mM xanthine solution followed by 100 μL of a 3.0-mM NBT solution. Then, a certain volume of a 10.0-mM phosphate buffer solution (pH 7.0± 0.1) was added to obtain 2,700-μL samples. The cuvette was then vortexed for 5 seconds to ensure a homogenous mixture. To initiate the SOD-enzymatic reaction, 300 μL of xanthine oxidase stock (1.5 g/L) was added and the cuvette was immediately vortexed for 5.0 seconds and introduced into the spectrophotometer. In this assay, all the reagents including the nanozymes were prepared using ultrapure water that is 10.0 mM in phosphate buffer. The evolution of the absorbance at 565 nm was recorded for 6.0 min. In addition, eight control samples were also prepared and measured similarly, each of which was prepared by the addition of all reagents except the nanozymes, with an additional volume of phosphate buffer solution to maintain the final sample volume.

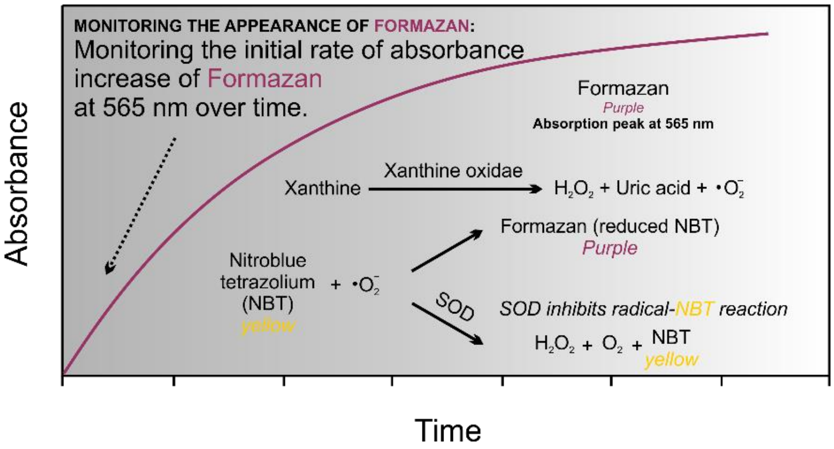

Figure 13. The SOD assay for the determination of the SOD-like activity. The $\bullet O_2^-$, generated via the oxidation of xanthine to uric acid by xanthine oxidase, can reduce the yellow NBT into a purple product, called formazan, which possesses a characteristic absorption peak at 565 nm. The SOD enzyme, nevertheless, effectively converts $\bullet O_2^-$ to H_2O_2, which leaves the NBT unchanged or partially reduced, resulting in the inhibition of the radical-NBT reaction. The extent of inhibition is studied via the UV-Vis spectrophotometry by probing the emergence of the formazan absorption peak at 565 nm over time. The inhibition curve of the radical-NBT is constructed as a function of nanozyme concentration using equation (39).

The inhibition curve is constructed by graphing the radical-NBT reaction inhibition, I, against the corresponding nanozymes concentration in the final sample. The inhibition can be calculated as follows:

$$I = \frac{\Delta A_o - \Delta A_s}{\Delta A_o} \cdot 100\% \tag{39}$$

where ΔA_S is the change in absorbance at 565 nm during the 6 min measurement time while ΔA_0 is the average change in absorbance of the eight control samples. The half maximal inhibitory concentration (IC_{50}) is the nanozyme concentration at which the NBT-radical inhibition is 50%. During the assays, while particle light scattering may contribute to the absolute absorbance value, this contribution is eliminated by taking the relative absorbance increase in the individual experiments.

4.7.2 Assessment of the HRP-like activity (the guaiacol and TMB assays)

The HRP catalyzes the breaks down of numerous peroxide compounds such as H_2O_2 and organic hydroperoxides into water and some activated donor molecules. In the presence of suitable substrates as indicators, the enzymatic reaction is typically accompanied by color changes that can be studied via spectrophotometry to assess the enzymatic activity.[168] Here, TMB and guaiacol were used as peroxidase substrates to probe the HRP-like activity of CeO_2 NPs and PB NPs, respectively. During both assays, the concentration of nanozymes and H_2O_2 were kept constant while the concentrations of substrates were varied.

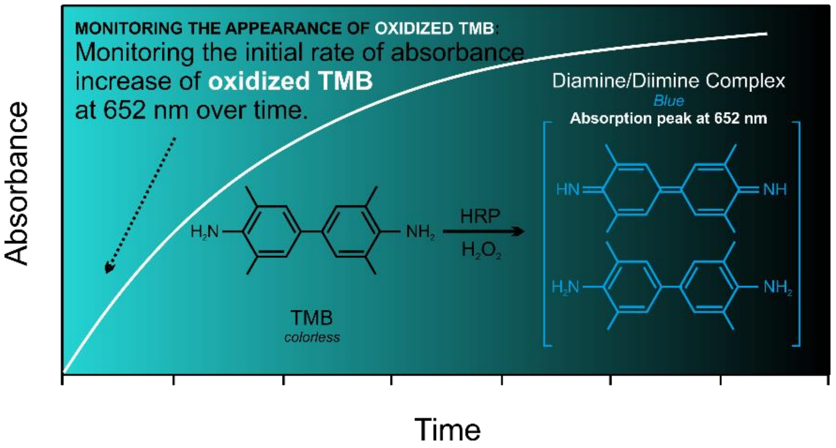

Figure 14. The TMB assay for the HRP-like activity. The colorless TMB is oxidized in the presence of H_2O_2 and HRP (or its mimetic nanozyme). The oxidized TMB, in the form of a diamine/diimine complex, is characterized by a blue color as well as a strong absorption peak at 652 nm. The increase in the absorbance of the blue complex over time at 652 nm is probed via the UV-Vis spectrophotometry. The molar absorption coefficient, ε, of oxidized TMB is 39.0 mM^{-1} cm^{-1}.

The TMB assay is based on the oxidation of the colorless TMB substrate in the presence of H_2O_2 and an HRP-mimicking nanozyme.[169] As shown in **Figure 14**, the oxidized TMB has a distinctive blue color and a characteristic absorption peak at 652 nm. The HRP-like activity of CeO_2-based composites was assessed at pH 4.0, 7.0, and pH 9.0 using acetate, phosphate, and TRIS-HCl buffers, respectively. During the TMB assay, the TMB was dissolved in dimethyl sulfoxide (DMSO) due to its poor solubility in water. Hence, with a final sample volume of 2,000 μL, a certain volume of a 5.0-mM TMB solution was mixed with 100 μL of a 500-mg/L CeO_2 stock, 500 μL of a 200-mM buffer solution, and a complimentary volume of ultrapure water to obtain 1,900-μL samples. To initiate the enzymatic reaction, 100 μL of a 100-mM H_2O_2 solution was added to the reaction mixture. The sample was then immediately homogenized before measurements, where the change in the absorption over time was monitored at 652 nm for 10 min.

On the other hand, the guaiacol assay is used to assess the HRP-like activity of PB NPs.[170] Similar to TMB's, the guaiacol assay relies on the oxidation of the colorless guaiacol in the presence of H_2O_2 and HRP-mimicking nanozymes. As shown in **Figure 15**, the oxidized guaiacol has a distinctive brown color with a characteristic absorption peak around 470 nm. The activity was assessed at pH 7.0 using phosphate buffer. Hence, with a final volume of 2,400 μL for each sample, a varied volume of a 100-mM guaiacol solution was mixed with 912 μL of a 131.6-mM buffer solution, 240 μL of a PB stock (that is 100 mg/L in PB NPs or PB content in AL-PB) followed a complimentary volume of ultrapure water to obtain 2,352-μL samples. After the cuvette was then vortexed for 10 s, the reaction was initiated by the addition of 48 μL of a 135-mM H_2O_2 solution, after which the sample is then immediately vortexed for additional 5 s before the introduction into the spectrophotometer, where the change in absorption over time was monitored at 470 nm for 10 min.

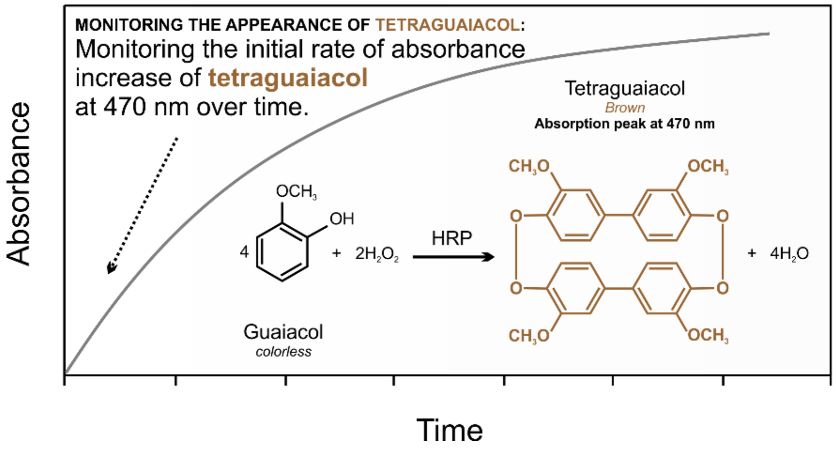

Figure 15. The Guaiacol assay for the determination of the HRP-like activity. In the presence of HRP-mimicking nanozymes and H_2O_2, the colorless guaiacol is oxidized to a brown product, called tetraguaiacol which is characterized by a strong absorption peak at 470 nm. The UV-Vis spectrophotometry is utilized to probe the emergence of such an absorption peak over time. The ε of tetraguaiacol is 26.6 mM^{-1} cm^{-1}.

In both assays, the increase in the absorbance of the oxidized substrate over time was used to obtain the reaction rate of the enzymatic reactions. The slope of the linear region in the spectra represents the reaction rate (in s^{-1}), and the molar rate (mM/s) is obtained using the Beer-Lambert law. In the current setup, the optical light path is 1.0 cm, and the molar extinction coefficients, ε, of the oxidized substrates are 39,000 $M^{-1}cm^{-1}$ (for oxidized TMB) and 26.6 $mM^{-1}cm^{-1}$ (for oxidized guaiacol). To assess the HRP-like catalytic potential, the reaction rate, v, is plotted against the corresponding substrate concentration, $[S]$, in each sample and the kinetic parameters are obtained by fitting the rate data with Michaelis-Menten model of enzyme kinetics, equation (2).

4.7.3 Assessment of the CAT-like activity (the catalase assay)

The CAT enzyme exclusively catalyzes the breakdown of H_2O_2 into water and O_2. The UV-Vis spectrum of H_2O_2 is characterized by a strong absorption peak at 240 nm. In the presence of CAT-mimicking nanozymes, the reduction in the absorbance of H_2O_2 with time at 240 nm is a measure of their CAT-like activity, as shown in **Figure 16**.

During the catalase assay, the concentration of the CAT-mimicking nanozyme is kept constant while that of H_2O_2 is varied.[163, 170] The pH in the samples was maintained at 7.0±0.1 using phosphate buffer. Hence, in each of the 2,400-μL samples, 1,000 μL of the 120-mM buffer solution was added to a certain volume of H_2O_2 followed by a volume of ultrapure water to obtain 2,200-μL samples, which was then vortexed for 5 s. To initiate the nanozyme-catalyzed breakdown of H_2O_2, 200 μL of 120 mg/L nanozyme dispersion was added, and the sample was immediately vortexed for 3 s before it was introduced into the UV-Vis spectrophotometer. The decrease in the absorption of H_2O_2 with time was recorded at 240 nm for 10 min.

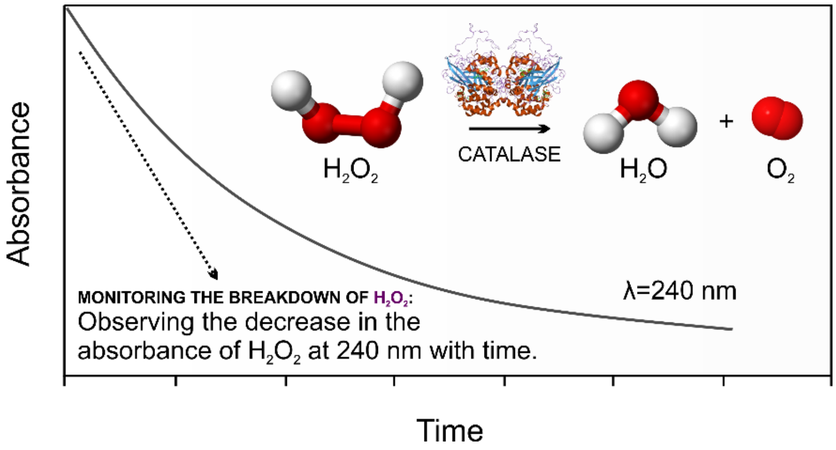

Figure 16. The catalase assay for the determination of the CAT-like activity. The CAT enzyme breaks down H_2O_2 into water and O_2. The H_2O_2 has an absorption peak at 240 nm. By monitoring the decrease in absorbance of H_2O_2 at 240 nm over time, the CAT-like activity can be assessed. The ε of H_2O_2 is 39.4 M^{-1} cm^{-1}.

The negative slopes of the initial linear portion of spectra represent the corresponding reaction rate measured in s^{-1} that is converted to mM/s using the Beer-Lambert law. In the instrumental setup, the optical light path is 1.0 cm, and the molar extinction coefficient, ε, of H_2O_2 is 39.4 M^{-1} cm^{-1}. Similar to the HRP, the CAT-like catalytic potential was quantitatively assessed by graphing the reaction rate, v, in each sample against the corresponding H_2O_2 concentration. and the kinetics of the enzymatic reaction was assessed by fitting the data with the Michaelis-Menten model, equation (2).

4.7.4 Assessment of the antioxidant potential (the DPPH assay)

The antioxidant potential of nanozymes is often evaluated by their ability to reduce the DPPH, a deep violet radical that has a strong absorption band around 517 nm. The reduction results in the formation of a yellow product (reduced DPPH) with no absorption at 517 nm.

As shown in **Figure 17**, the extent of DPPH reduction by a potential antioxidant is assessed using the DPPH assay, where the change in the absorption at 517 nm with time was recorded at various nanozyme concentrations and a fixed concentration of DPPH.[171-173] The DPPH stock is prepared in methanol due to its poor solubility in water. With a final volume of 3,000 µL, each sample was prepared by the addition of a certain volume of nanozyme dispersion to 1,800 µL of a 25-mg/L DPPH solution with an additional volume of methanol to maintain the same final volume. After the addition of all components, the sample under study was immediately vortexed before the introduction into the UV-Vis spectrophotometer. The proportion of unreacted DPPH (DPPH%) is obtained using the following equation:

$$DPPH\% = \frac{A}{A_0} 100\% \tag{40}$$

where A_0 and A are the initial and steady-state absorbance values of the sample under study, respectively. To assess the DPPH scavenging potential, the DPPH% is plotted against the corresponding nanozyme concentration, and the effective concentration (EC_{50}), a quantitative measure of the antioxidant potential, is the nanozyme concentration at which DPPH% is 50%, that is, half of the initially present DPPH radicals are reduced.

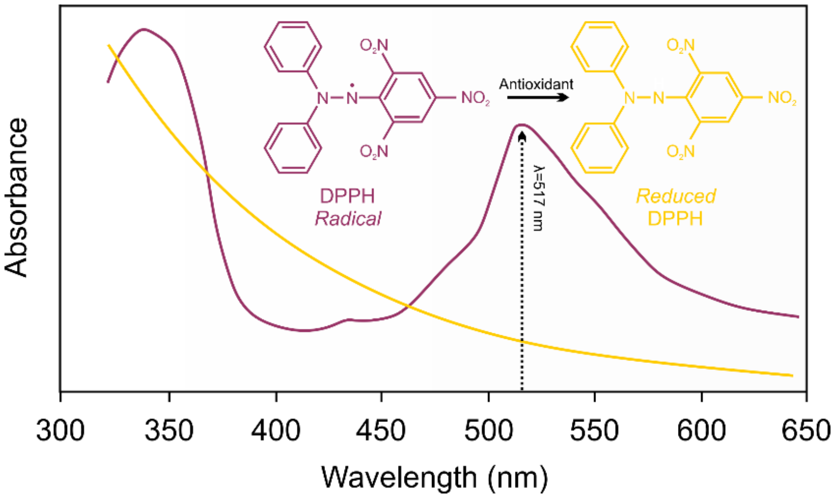

Figure 17. The DPPH assay for the assessment of the antioxidant potential. The deep violet DPPH radical has a strong absorption peak at 517 nm. The reduced DPPH, however, has no such absorption peak. The disappearance of such peak over time in the presence of some material is a measure of the antioxidant potential of the material.

5 Results & Discussion

5.1 Structural characterization

Nanozymes (PB, MnO_2, and CeO_2) were prepared according to reported protocols. An essential and crucial step is the confirmation of successful preparation, which was achieved via several instrumental techniques including XRD, XPS, as well as Raman and UV-Vis spectroscopy.

5.1.1 Characterization of PB NPs

The recorded UV-Vis spectrum of PB NPs, **Figure 18(a)**, exhibits a broad absorption band around 700 nm, which is characteristic of PB and is attributed to the charge transfer between Fe(III) and Fe(II) through the cyano groups.[174] The morphology of PB NPs was examined via electron microscopy. The TEM image, embedded in the background of **Figure 18(a)**, shows that PB NPs exhibit distinct semi-spherical morphology with a particle size of ~42.0 nm.

In addition, the surface chemical composition was probed via XPS. Shown in **Figure 18(b)**, the XPS survey scan contains characteristic peaks of Au, Fe, C, N, and O, with Au originating from the Au-plated sample holder rather than the solid PB sample. Also, the high-resolution deconvoluted XPS spectrum of Fe 2p, **Figure 18(c)**, further reveals the presence of mixed-valence Fe, indicating the formation of the PB compound. The peaks at 708.69 eV and 710.29 eV corresponds to Fe(II) $2p_{3/2}$ and Fe(III) $2p_{3/2}$, respectively, which agrees quite well with reported values in the literature.[175] The high-resolution deconvoluted spectrum of C 1s indicates that surface carbon moieties exist in four separate chemical environments, as shown in **Figure 18(d)**, with an overlap between the C-OH functionalities and the cyano groups. In addition, the deconvolution of the N 1s region (**Figure 18(e)**) gives rise to three major peaks. The peak at 397.78 eV corresponds to nitrogen in the cyanide ligands,[175, 176] while the 399.35 eV peak is attributed to charge transfer among surface moieties.[177] The peak at 402.3 eV, on the other hand, suggests the presence of positively charged nitrogen such as ammonium ions, which have been detected in PB compounds.[175] The mild heat treatment during the sample drying process presents a likely source of ammonium ions. The presence of ammonium ions can also be indirectly inferred from **Figure 18(c)**. The satellite peak of Fe(II) at 712.68 eV indicates that surface Fe(II) mostly exists in a high-spin state. However, since the cyanide is a strong field ligand, Fe(II) should exist solely in a low-spin state. In PB lattice, only the Fe(III) sites are characterized by weak ligand field, these sites can be occupied by Fe(II) in the presence of monovalent cations (such as ammonium) by the formation of an Everitt's salt-type compounds (an analog of PB) on the surface.

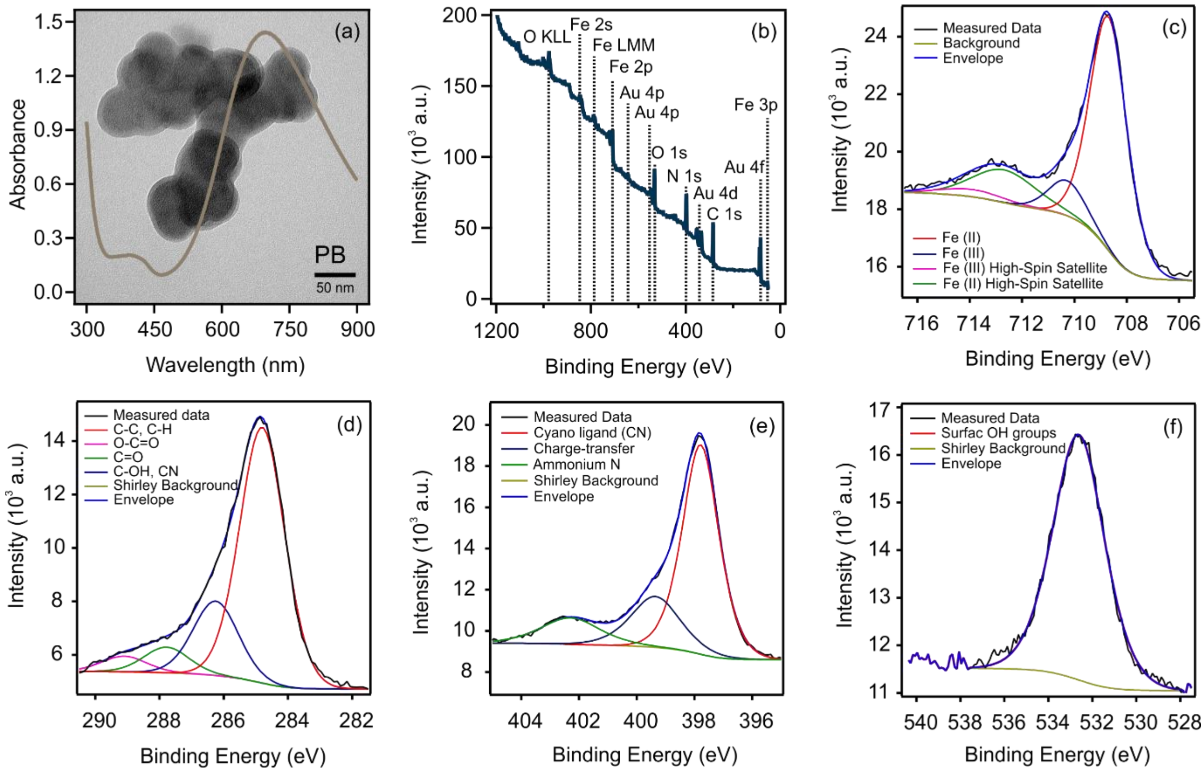

Figure 18. (a) UV-Vis absorption spectrum of PB NPs at pH 4, the TEM image of PB NPs is embedded in the background of the UV-Vis absorption spectrum. (b) The XPS survey spectrum of the PB sample. The Auger transitions within K, L, and M energy levels give rise to O KLL and Fe LMM peaks. The high-resolution XPS spectra of (c) Fe $2p_{3/2}$, (d) C 1s, (e) N 1s, and (f) O 1s of the PB sample. The Shirley background estimation serves to distinguish the background signal occurring due to energy loss as a result of inelastic scattering.

The high-resolution O 1s region in **Figure 18(f)** contains a single peak around 532.76 eV, which is attributed to surface OH groups. Based on the XPS compositional analysis, the following surface composition was obtained: 4.3% Fe, 53.1% C, 30.9% N, and 11.7% O. The detailed XPS composition information is shown in **Table S1** in **Appendix D**.

5.1.2 Characterization of MnO_2 MFs

The surface chemical composition of the as-prepared MnO_2 MFs was explored with XPS. As shown in **Figure 19(a)**, the survey scan reveals the presence of Mn, C, K, and O elements. The deconvolution of the Mn 2p region (**Figure 19(b)**) is not straightforward due to a large number of different oxidation states, the presence of mixed valence oxides, and the complex multiplet splitting within the region.[178, 179] However, the average oxidation state of Mn on the surface was initially assessed by evaluation of the peak separation in the Mn 2s region, shown in **Figure 19(c)**. The peak separation (5.1 eV) was found to be slightly lower than those of common Mn(III) compounds (5.5 eV for Mn_2O_3 or 5.4 eV for MnOOH), which indicates the possible presence of compounds of varying valence states on the sample surface. In MnO_2, the peak separation of Mn(IV) is 4.4 eV, which agrees well with the splitting of Na_xMnO_2-type compounds.[180] However, this approach is not reliable for the determination of the chemical species on the surface and requires the fitting of the Mn 2p peak.[179] The fitting of the Mn 2p peak in **Figure 19(b)** was performed by considering the multiplet splitting of the species and revealed that surface Mn is primarily present as MnO(OH) (64%) and MnO_2 (36%).

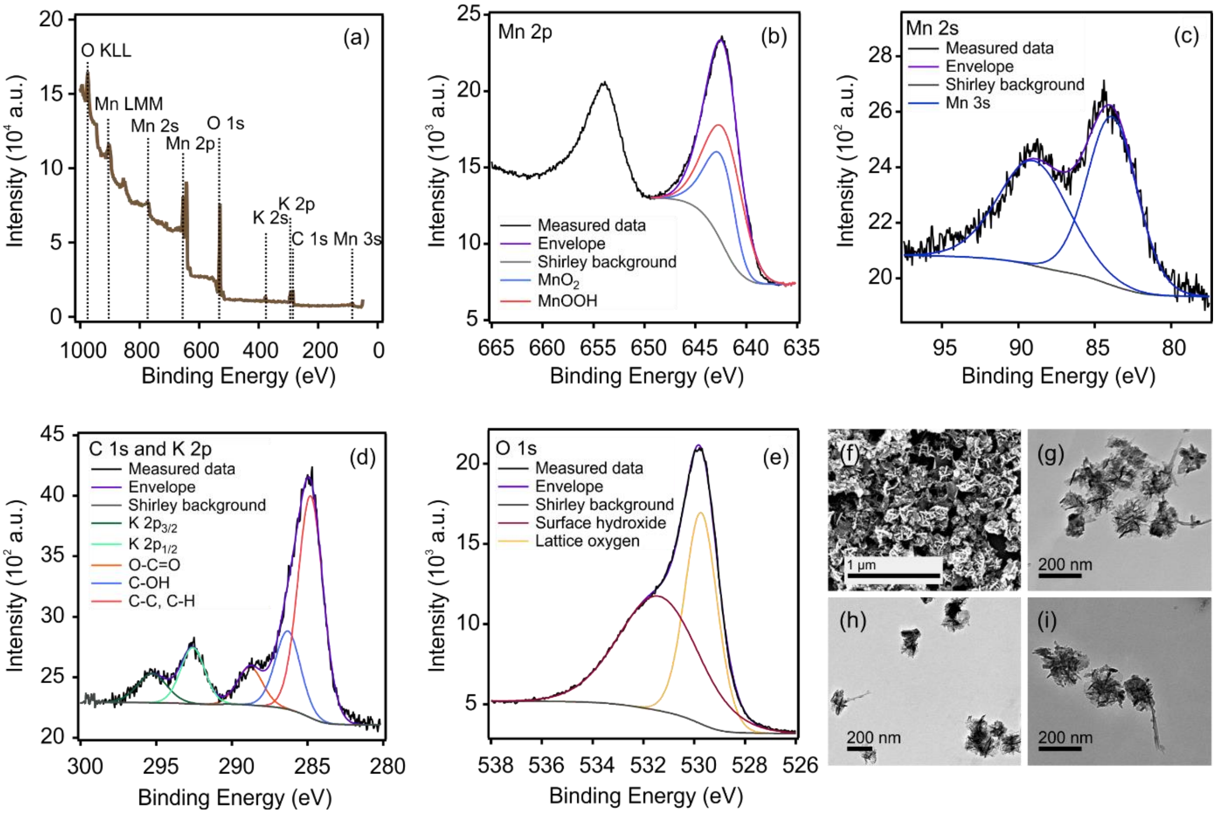

Figure 19. (a) XPS survey spectrum of the as-prepared MnO_2 MFs. The Auger transitions within K, L, and M energy levels give rise to O KLL and Mn LMM peaks. The high-resolution XPS spectra of (b) Mn 2p, (c) Mn 2s, (d) C 1s and K 2p, and (e) O 1s regions. The Shirley background estimation serves to distinguish the background signal occurring due to energy loss as a result of inelastic scattering. The (f) SEM and (g-i) TEM images of MnO_2 MFs.

The high-resolution C 1s spectrum (**Figure 19(d)**) indicates the presence of adventitious carbon. The peaks at 288.09 eV and 286.14 eV are attributed to O–C=O and C–OH functionalities, respectively, while the 284.79 eV peak is indicative of C–C and C–H states. A likely source of minimally present K^+ is the chemicals used during the synthesis. The high-resolution O 1s spectrum (**Figure 19(e)**) reveals the presence of two oxygen states originating from the lattice oxide (529.73 eV) and surface hydroxides (531.39 eV). The position and relative contribution of those peaks, however, suggest that hydroxide species are prevalent.[179] The quantitative XPS composition analysis revealed the following sample composition: 23.4 at% Mn, 19.5 at% C, 1.3 at% K, and 55.8 at% O. The morphology of MnO_2 MFs was visualized using electron microscopy. The SEM and TEM images, shown in **Figure 19(f)** and **Figure 19(g, h, and i)**, respectively, feature flake-like morphology of MnO_2, the aggregated state of the sample is attributed to the drying process during sample preparation. The MnO_2 sample is fairly polydisperse with the size of the flake-like particles ranging between 150 and 200 nm. Such morphology of MnO_2 is well reported in the literature.[181, 182]

5.1.3 Characterization of CeO_2 NPs

The successful preparation of CeO_2 NPs was verified by the X-ray diffraction (XRD) technique (**Figure 20(a)**). The XRD patterns of the CeO_2 powder show all the characteristic XRD reflections of CeO_2, within the measured 2θ range, that match those reported in the standard patterns of CeO_2 (JCPDS card no. 34–0394).[183] The sharp reflection peaks indicate that the formed CeO_2 NPs are highly crystalline. Similar XRD patterns were reported in the literature as well, and the reflections can be indexed to CeO_2 with a fluorite structure (Fm3m space group).[184]

In addition, the XPS survey scan, shown in **Figure 20(b)**, reveals the presence of Ce, O, C, and Fe elements on the surface of the sample. The Fe originates from the sample holder. Similar XPS spectra for CeO_2 are reported in the literature.[183, 185] In addition, the high-resolution Ce 3d core-level spectrum (**Figure 20(c)**) suggests the presence of two sets of multiplets. The (v^0, v’) and (u^0, u’) peaks are attributed to Ce(III), while the (v, v”, and v’”) and (u, u”, and u’”) peaks are attributed to Ce(IV), which indicate the presence of mixed-valence Ce.[184, 185] The contribution of Ce(III) to the toral composition is around 15 at%, indicating sub-stoichiometric surface composition.[186] In addition, the presence of the C 1s region is attributed to the adventitious carbon. The high-resolution deconvoluted spectrum of the C 1s region is shown in **Figure 20(d)**, the peaks at 286.37 eV and 289.07 eV refer to C–OH and O–C=O, respectively, whereas the 284.82 eV peak refers to C–C and C–H states. The high-resolution O 1s spectrum (**Figure 20(e)**) reveals two peaks at 529.62 eV (lattice oxide) and 531.62 eV (surface hydroxide). The relative contribution as well as the position of the two peaks indicate the greater presence of hydroxide species on the sample surface.[187] The quantitative XPS composition analysis revealed the following surface composition: 14.8 at% Ce, 24.8 at% C, and 60.4 at% O. The lattice oxide comprised 43.7% of the overall O 1s peak, and hence, the surface stoichiometry of the sample is $CeO_{1.8}$, which is quite close to CeO_2. Detailed binding energies for all detected surface species are listed in **Table S2** in **Appendix D**.

The Raman spectrum of CeO_2 NPs (**Figure 21(a)**) shows an intense peak at 462 cm^{-1}, which is attributed to the symmetrical stretching mode of the Ce–O. The inset graph provides a closer look at the 462-cm^{-1} peak in the Raman shift range of 350–550 cm^{-1}, such a peak is characteristic of CeO_2, as reported elsewhere.[188, 189] The UV-Vis spectrum (**Figure 21(b)**) is recorded in the range of 250–550 nm range. The characteristic broad peak around 300 nm for CeO_2 is well reported in the literature.[190, 191]

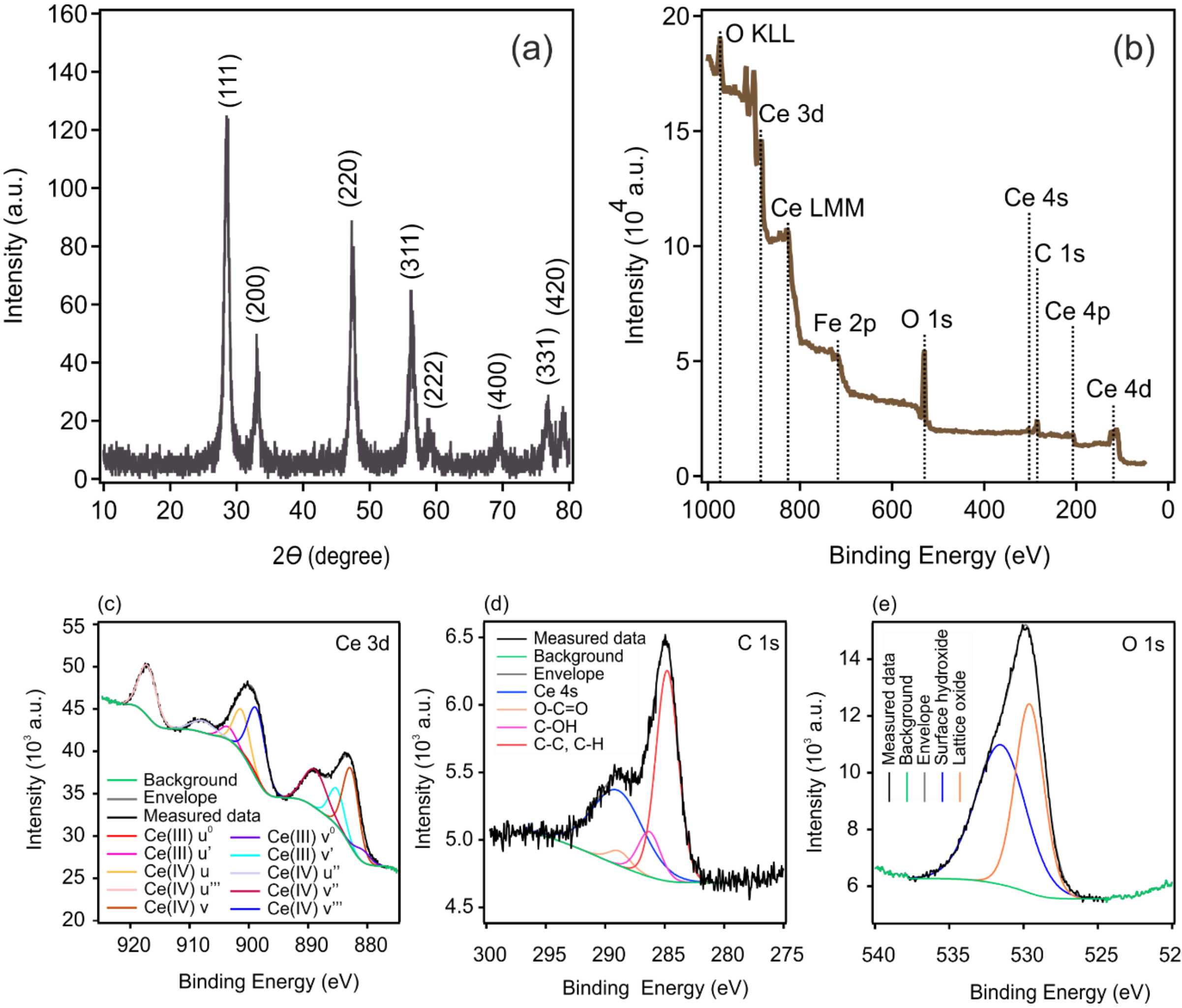

Figure 20. (a) XRD patterns and (b) XPS survey spectrum of the CeO_2 NPs. The Auger transitions within K, L, and M energy levels give rise to O KLL and Ce LMM peaks, and the presence of Fe is attributed to the sample holder. The high-resolution XPS spectra of (a) Ce 3d, (b) C 1s, and (c) O 1s regions.

The morphology of CeO_2 NPs was analyzed with TEM and high-resolution TEM (HR-TEM). The TEM image of the as-prepared CeO_2 NPs (**Figure 21(c)**) shows particles with well-established boundaries and characterized by semi-cubic morphology; the sample is quite monodisperse with particle size in the range of 10-15 nm, and the aggregated state of the sample can be attributed to the drying process during sample preparation. The HR-TEM image (**Figure 21(d)**) of CeO_2 NPs exhibits crystal fringes with varying orientations, the squared region in the HR-TEM image has a number of distinct and superimposed lattice spacings. Therefore, the fast Fourier transform (FFT) analysis was performed and resulted in the FFT pattern (**Figure 21(e)**), the *inverse* FFT analysis enabled the determination of lattice spacings, which are shown along the evaluated values in the inset images of **Figure 21(e)**. The ~0.25 nm lattice spacing corresponds to the XRD (200) peak. The ~0.36 nm is close to the lattice spacing obtained by the (111) peak, which is ~0.31 nm, but it cannot be unambiguously assigned. Similarly, the lattice spacing of ~0.75 nm corresponds to a 2θ value outside the measured 2θ range in the recorded XRD patterns, and thus, cannot be unambiguously assigned.

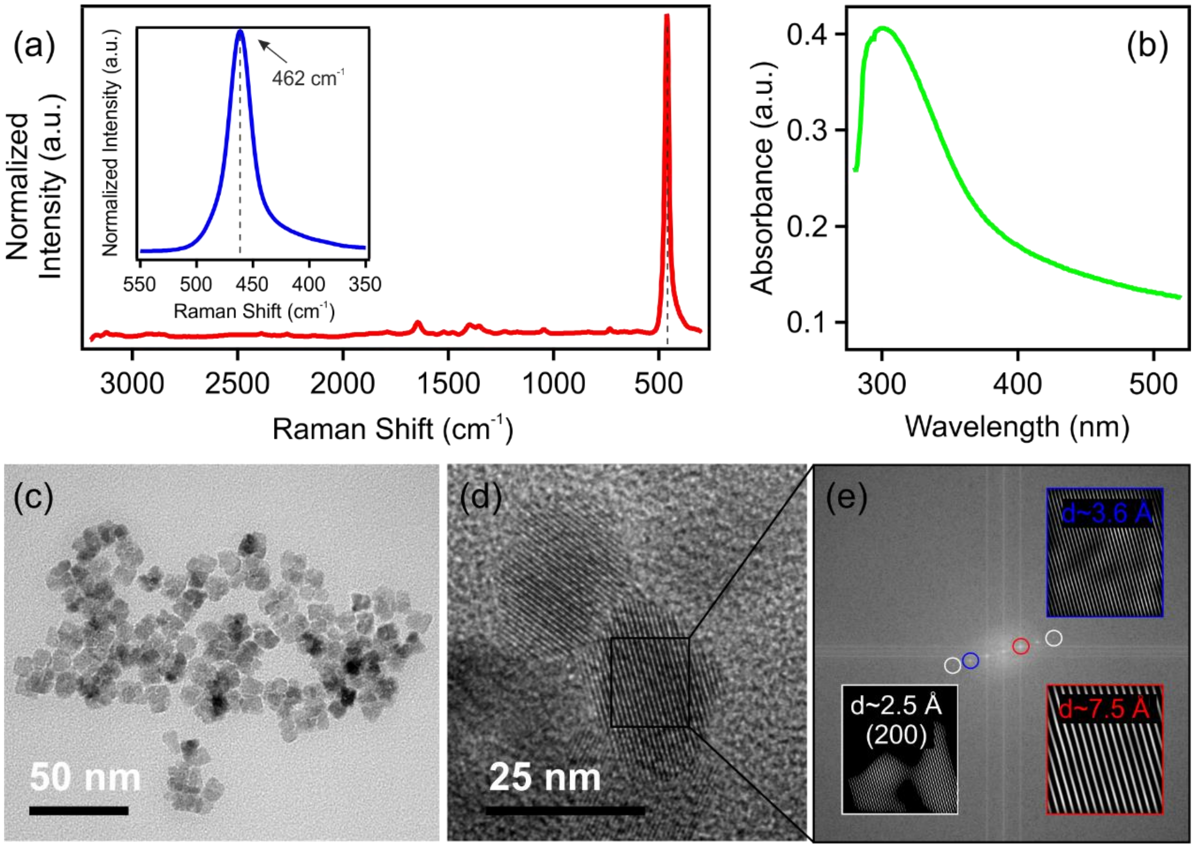

Figure 21. (a) The Raman spectrum (Inset graph: the magnified 462-cm^{-1} peak), (b) the UV-Vis absorption spectrum, (c) the TEM image, and (d) the HR-TEM image of bare CeO_2 NPs. (e) The extracted pattern, obtained by FFT analysis of the squared section in the HR-TEM image, the inset images, and lattice spacing values are obtained by inverse FFT analysis of the FFT pattern, using ImageJ software.[192]

Based on the results of the various analyses above, the preparation of the three nanozymes (PB, MnO_2, and CeO_2) was successful. For all nanozymes, the XPS data agrees very well with those reported in the literature. For CeO_2, the Raman spectrum and XRD diffractogram are also in good agreement with literature and standard databases. In addition, the TEM imaging of the nanozymes revealed a large size difference between nanozymes and the latex particles, which would enable the immobilization of a significant amount of nanozymes. Next, the colloidal properties of the individual particles are thoroughly examined at various pH and ionic strength conditions.

5.2 Colloidal characterization

The nanozymes used involve metal oxide and cyanide nanoparticles, whose effective surface charge varies with experimental conditions. Thus, for the appropriate formation of nanocomposites via electrostatic attraction, certain experimental conditions ought to be optimized such as the pH, the ionic strength, and the optimal concentration of the latex particles. The aim here is to obtain fine dispersions of non-aggregating particles with an appropriately high magnitude of surface charge.

5.2.1 The pH-dependent surface charging

The pH profile of the nanozymes and the SL particles were probed in the pH range of 3-11 at 1.0 mM ionic strength. The pH profiles of PB NPs, MnO_2 MFs, CeO_2 NPs, and SL particles were generated. On the other hand, the AL particles were commercially obtained and were not further characterized.

As shown in **Figure 22**, the PB NPs showed no extreme change in the hydrodynamic radii or electrophoretic mobility values throughout the pH range of 3-11. Around pH 4, the PB NPs possessed an average hydrodynamic radius of 58.0 ± 7.0 nm and an electrophoretic mobility value of -1.50 ± 0.20 ($\times 10^{-8}$ m^2/Vs) corresponding to a zeta potential of around -19.24 ± 2.60 mV. The origin of the negative charge is attributed to the deprotonated surface hydroxyl and carboxyl groups, where the generated electrostatic repulsion prevents particle aggregation giving rise to stable dispersions. Thus, pH 4.0 was selected for the formulation of PB-based composites.

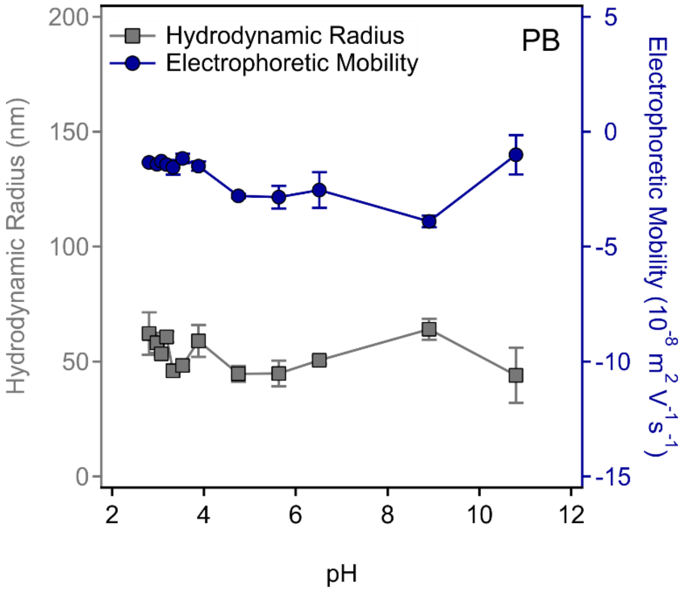

Figure 22. The pH profile of PB NPs. The ionic strength was fixed at 1.0 mM and the PB concentration was 100 mg/L.

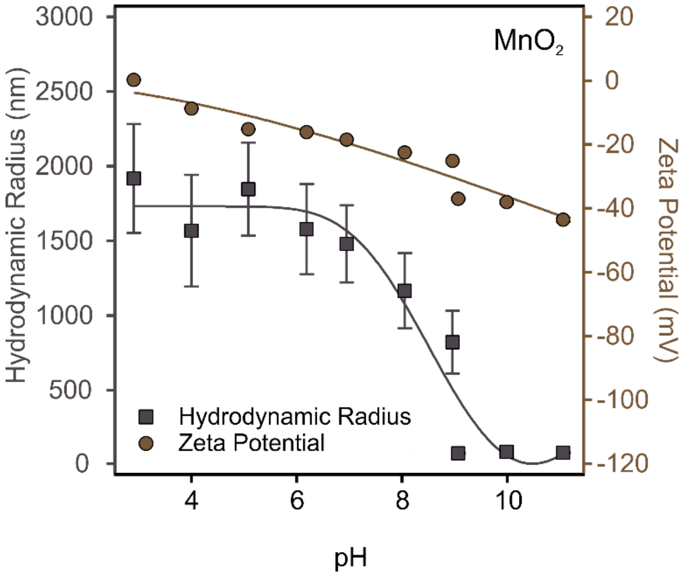

Figure 23. The pH profile of MnO_2 MFs. The ionic strength was fixed at 1.0 mM and the MnO_2 concentration was 50 mg/L. (Reproduced from Ref. 193 with permission from the Royal Society of Chemistry).

In the case of MnO_2 MFs (**Figure 23**), the size and zeta potential were found to be highly dependent on the pH of the medium. The MnO_2 MFs experienced heavy aggregation in acidic and neutral pH conditions resulting in hydrodynamic radii as high as 1.5 μm and zeta potential values well below 20 mV due to protonated surface functionalities. In these two pH regimes, the electrostatic forces are significantly weakened, and the EDL can be modeled by the Debye-Hückel approach. Hence, the vdW forces are dominant resulting in micron-sized particles, rendering acidic and neutral conditions not suitable for composite formation. As shown in **Figure 23**, when the pH is increasingly alkaline, the particles become well dispersed, and the aggregation is minimized. At pH ≥ 9.0, the particles are characterized by a hydrodynamic radius of 83.0 ± 2.0 nm and a PDI of 11.9%. In alkaline media, surface hydroxyl groups are deprotonated, and thus, MnO_2 MFs have a high negative electrophoretic mobility of −2.88 ± 0.02 ($\times 10^{-8}$ m^2/Vs), corresponding to a zeta potential value of −37.02 ± 1.4 mV, which is high enough for the prevalence of electrostatic repulsive forces. Thus, pH 9.0 was selected for the formulation of MnO_2-based composite systems.

The CeO_2 NPs exhibited a high positive charge in acidic media, due to the protonated surface OH groups. At pH 4.0, the electrophoretic mobility was 2.55 ± 0.06 ($\times 10^{-8}$ m^2/Vs), which is equivalent to 32.7 ± 0.7 mV. As shown in **Figure 24**, the extent of protonation decreased as the pH increased resulting in a gradual decrease in the zeta potential. The CeO_2 NPs exhibited an IEP at pH ~6.2, above which the particles undergo charge reversal, where the deprotonation of surface OH groups gave rise to the development of negative surface charge, whose magnitude increased as the pH became more alkaline. At pH 9.0, the electrophoretic mobility and the corresponding zeta potential were −2.28 ± 0.07 ($\times 10^{-8}$ m^2/Vs) and −29.2 ± 0.9 mV, respectively. The increase in the absolute values of the zeta potential was paralleled by a decrease in the hydrodynamic radii reaching as low as 181.2 ± 24.2 nm and 180.0 ± 31.4 nm at pH 4.0 and 9.0, respectively. Within the pH range of 5.5-8.5, the zeta potential fell in the range ±10 mV, within which surface charge provides insignificant electrostatic repulsive forces, triggering diffusion-controlled aggregation under the influence of vdW forces, as indicated by the sudden and significant rise in hydrodynamic radius, reaching 950 nm around pH 7.0. In the CeO_2 NPs system, both pH 4.0 and 9.0 are suitable for composite formation due to the non-aggregated state and the high zeta potential magnitude.

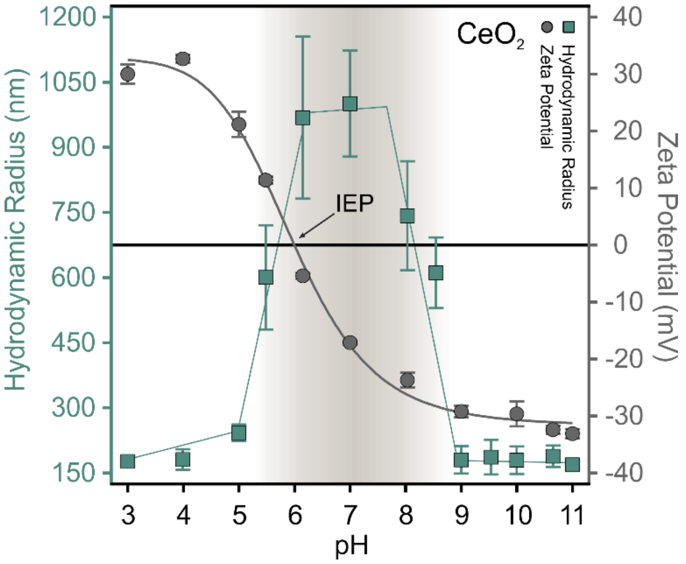

Figure 24. The pH profile of CeO_2 NPs. The ionic strength was fixed at 1.0 mM and the CeO_2 concentration was 50 mg/L.

As shown in **Figure 25**, the SL particles exhibited remarkable colloidal stability throughout the pH range of 3-11, within which they maintained an average hydrodynamic radius value of 432 ± 16 nm, indicating no effect of the pH. The zeta potential, on the other hand, was observed to gradually increase as the pH was raised due to increased deprotonation of the surface sulfate groups. At pH 9.0, the average electrophoretic mobility and the zeta potential values of SL particles were found to be −5.03 ± 0.04 ($\times 10^{-8}$ m^2/Vs) and −64.6 ± 0.5 mV, respectively. The hydrodynamic radius was 441 ± 33 nm with a PDI of 20.9%. At pH 4.0, on the other hand, the average hydrodynamic radius was 415 ± 27 nm with a PDI of 20.9%. In addition, the average electrophoretic mobility and zeta potential of SL at pH 4.0 were −3.28 ± 0.06 ($\times 10^{-8}$ m^2/Vs) and −42.1 ± 0.7 mV, respectively. Thus, the SL particles are expected to serve as an excellent support material throughout a wide pH range and maintain excellent colloidal stability. The commercial AL particles have a surface charge density of +19.7 μC/cm^2 and a mean diameter of 0.51 ± 0.02 μm with a 4.6% coefficient of size variation. The AL particles also formed stable dispersions that heavily resist the pH change, as reported in the literature.[160, 194]

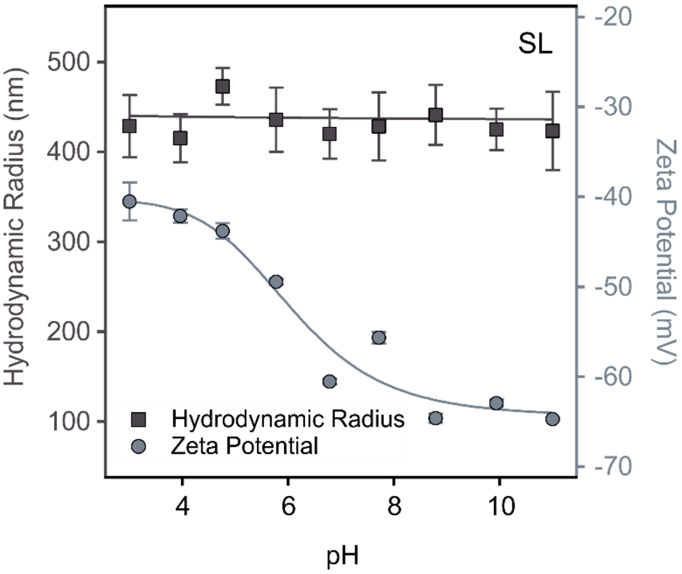

Figure 25. The pH profile of SL particles. The ionic strength was fixed at 1.0 mM and the SL concentration was 125 mg/L. (Reproduced from Ref. 193 with permission from the Royal Society of Chemistry).

The radically different response to the pH among the different nanozymes substantiates the importance of such measurements since it also enables the assignment of the latex to the proper nanozyme and allows the determination of optimal pH conditions, where the particles possess the maximum magnitude of surface charge that would maximize the electrostatic interactions during composite formation. For instance, MnO_2 MFs cannot form composites in acidic and neutral media. Similarly, CeO_2 NPs cannot form catalytic composites via heteroaggregation at a neutral pH regime, as a result of the IEP. Therefore, based on the pH profiles, the PB NPs are heteroaggregated with AL, as well as CeO_2 NPs with SL, in acidic conditions (pH 4.0). On the other hand, MnO_2 MFs and CeO_2 NPs can be heteroaggregated with SL at pH 9.

5.2.2 The diffusion-controlled aggregation

After the proper pH condition is determined, the optimal latex concentration for composite formulation must be assessed. This was achieved by systematically probing the aggregation kinetics at various particle concentrations, at the optimal pH and high ionic strength. By setting the background salt concentration at 1.0 M, all electrostatic repulsive forces are screened, and thus, particles are expected to undergo diffusion-controlled aggregation under the influence of vdW forces, according to the DLVO theory.[129] In addition, the selected optimal concentration is a compromised value, it is high enough to provide adequate scattering intensity during DLS and ELS measurements. At the same time, it is sufficiently low, so the system remains in the early-stage aggregation regime within the measurement time frame. The k_{app} and $T_{1/2}$ can be obtained for the diffusion-controlled latex aggregation, using equations (35) and (33), by probing the relative change in the hydrodynamic radii over time via time-resolved DLS.

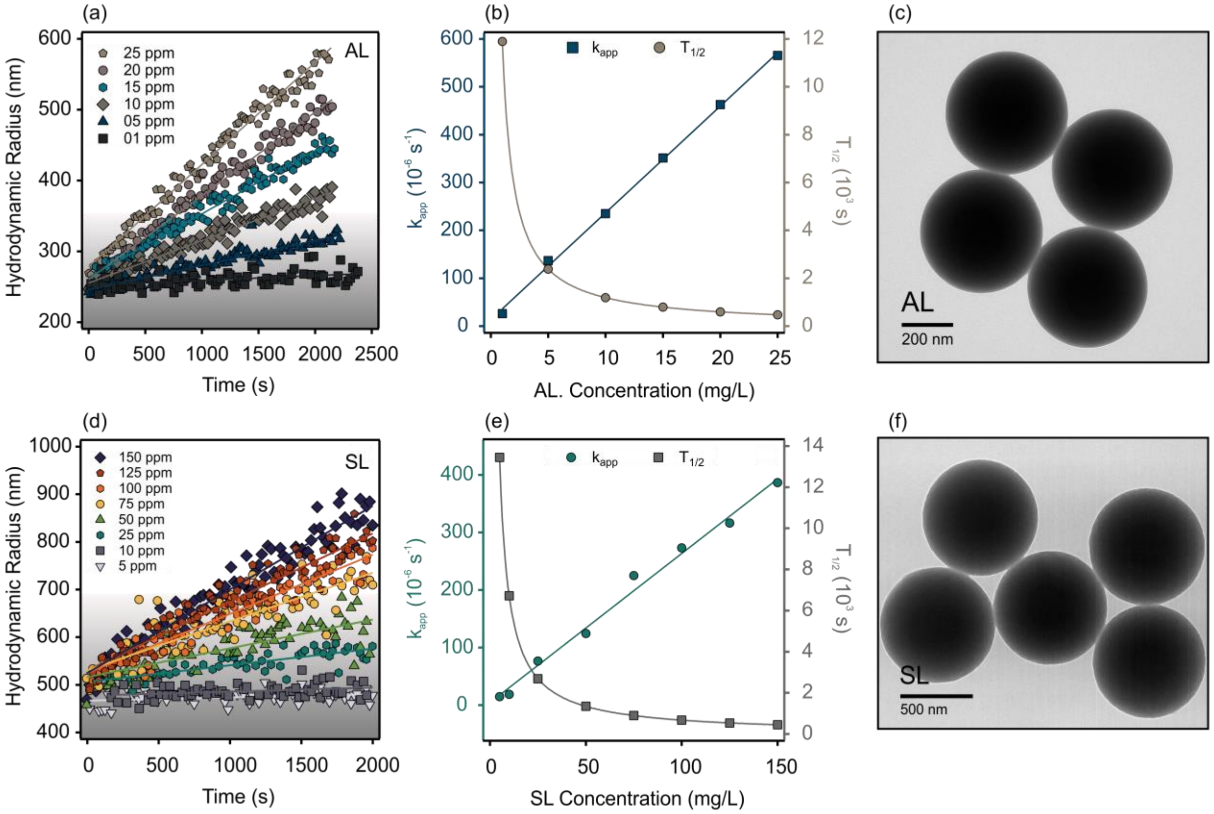

Figure 26. Time-resolved DLS measurements of (a) AL (pH 4.0) and (d) SL (pH 9.0) at various particle concentrations, N_0, and 1.0 M ionic strength. The gray-shaded regions represent the early-stage aggregation regime within the given time frame. The straight lines represent the linear fits used to calculate the k_{app} and $T_{1/2}$ of (b) AL and (e) SL at the corresponding N_0. The TEM images of (c) AL and (f) SL particles.

Figure 26(a) shows the time-resolved DLS measurements of the diffusion-controlled aggregation of AL particles at pH 4.0 in the particle concentration range of 1-25 mg/L and 1.0 M KCl. As the graph shows, the aggregation occurs faster in more concentrated dispersions, in which the collision frequency is higher, and thus, the k_{app} is expected to be proportional to the particle's concentration (**Figure 26(b)**). Simultaneously, the $T_{1/2}$ decreases with increasing particle concentration due to accelerated aggregation in concentrated samples. The TEM image of AL particles (**Figure 26(c)**) shows that the particles are characterized by distinct and uniform spherical morphology, as reported by the manufacturer as well, with an average diameter of 0.51 ± 0.02 μm. Similar aggregation trends were observed for the SL particles (**Figure 26(d)**), for which the diffusion-controlled aggregation was probed in the concentration range of 1.0-200 mg/L at pH 9.0 and 1.0 M NaCl. Like the AL system, more concentrated SL samples resulted in faster aggregation, higher k_{app}, and lower $T_{1/2}$ (**Figure 26(e)**). In addition, the morphology of SL particles is characterized by well-defined spherical morphology, as shown in the TEM image of SL in **Figure 26(f)**. Also, the average diameter of SL is 0.864 ± 0.032 μm, based on DLS measurements with a low PDI value (20.9%).

As shown in **Figure 26(e)**, the k_{app} and $T_{1/2}$ of SL particles are similar in magnitude to those of the AL system since the diffusion-controlled aggregation is mainly driven by vdW forces. As established earlier, the vdW forces are relatively independent of the experimental conditions, and hence, the diffusion-controlled aggregation of AL and SL will be more affected by the nature of the particles. Since both latex materials are based on polystyrene, the aggregation rate relative to the initial particle size, i.e., k_{app}, is not expected to differ by a large magnitude. The shaded regions in **Figure 26(a)** and **(d)** represent the early-stage aggregation regime within the measurement time frame. As detailed in **Figure 11**, the early-stage aggregation regime is the region within which dimer formation is dominant, and hence, the maximum increase in the hydrodynamic radii of spherical particles is 38%, i.e., $1.38R_{\text{monomer}}$.[139] These correspond to ~345 nm and ~690 nm for AL and SL dimers, respectively. Thus, at 1.0 M, AL and SL concentrations above 5.0 mg/L and 75.0 mg/L, respectively, lead to the formation of high aggregates and the cessation of the early-stage phase of the aggregation. The selected concentrations of AL and SL particles are 25.0 mg/L and 125.0 mg/L, respectively. At those concentrations, the systems will not exist in the early-stage aggregation at 1.0 ionic strength, within the measurement time frame. Nevertheless, in further measurements, the aggregation regimes are further explored at various salt concentrations, where it will be shown that the selected latex concentrations resulted in colloidal systems that remain in the early-stage aggregation at ionic strength values lower than 1.0 M.

5.2.3 The salt-induced aggregation

For the latex particles (SL and AL) and metal oxides (CeO_2 NPs and MnO_2 MFs), the salt-induced aggregation in the respective dispersions was examined at the designated pH by following the variation in the stability ratio and the zeta potential at various ionic strength conditions. Such measurements enable the characterization of the salt tolerance of the individual systems. Also, the surface charge density, σ, (in C/m^2) can be estimated by fitting the zeta potential data with the Grahame relation, equation (16), and the measured value of CCC are obtained using equations (37) and (38), as illustrated in **Appendix C**.

Thus, the trends in the aggregation and charging of the AL particles at 25 mg/L and pH 4.0 were assessed at various KCl concentrations. As shown in **Figure 27(a)**, the zeta potential of AL particles decreased significantly as the ionic strength (KCl concentration) in the dispersion was changed from 1.0 mM to 2,000 mM. At 1.0 M the zeta potential of AL particles approached zero, as quantitatively predicted by the PBE. The addition of salt leads to a counter-ion buildup within the EDL around charged AL particles, resulting in reduced effective surface charge. In addition, the reduction of surface charge with elevated salt level gradually weakens the repulsive electrostatic forces as the vdW forces become more significant leading to increased aggregation, and thus, decreased stability ratio. The estimated CCC occurred at 58.9 mM KCl. At the ionic strengths at and beyond the CCC, the stability ratio approaches unity, and the system is characterized by rapid and diffusion-controlled aggregation under the influence of vdW forces.

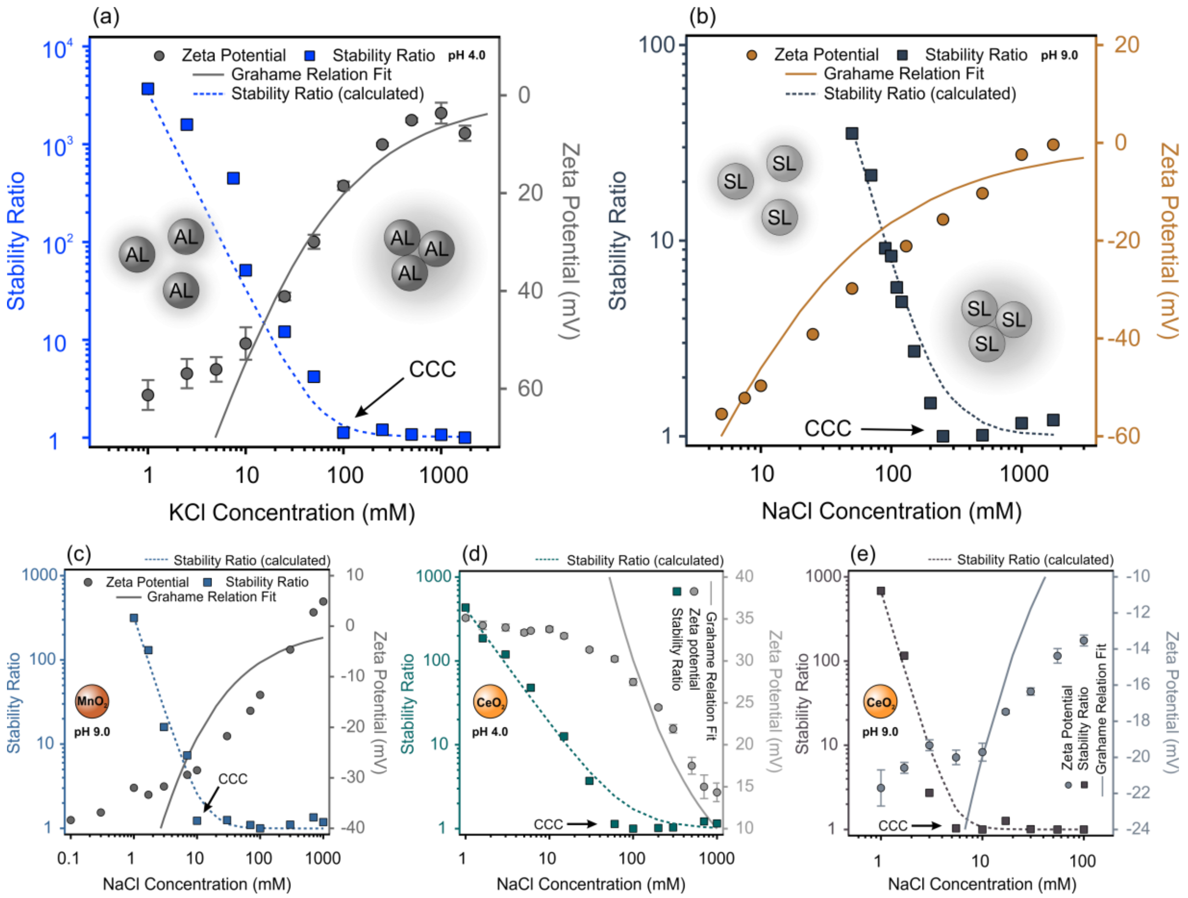

Figure 27. The salt-induced aggregation. The stability ratio (squares) and zeta potential (circles) values for (a) AL, (b) SL, (c) MnO_2 MFs, (d) CeO_2 NPs (pH 4.0), and (e) CeO_2 NPs (pH 9.0) as a function of the ionic strength, at the designated pH. The concentrations of AL and SL were fixed at 25 mg/L and 125 mg/L, respectively, while the concentrations of the CeO_2 NPs and MnO_2 MFs were fixed at 100 mg/L. The dashed lines represent the calculated stability ratios, based on equations (37) and (38), as shown in **Appendix C**. The solid lines represent the Grahame relation fit, equation (16), for the zeta potential-ionic strength data.

Similar trends were observed in the dispersions of SL particles at 125 mg/L and pH 9.0. As **Figure 27(b)** shows, the magnitude of the zeta potential of SL particles also decreased significantly as the NaCl concentration was increased, approaching zero when the NaCl concentration is around 1.0 M. Similar to the AL system, the addition of background salt shrinks the EDL, reduces the effective surface charge, and triggers rapid aggregation of the SL particles. The stability ratio decreased as the ionic strength was raised due to the increased significance of the vdW forces, as predicted by the PBE theory. The CCC occurred at 224.5 mM, after which the system is characterized by rapid aggregation with stability ratio values near unity.

Apart from the latex particles, the salt-induced aggregation was probed for the nanozymes that exhibit pH-dependent aggregation, i.e., MnO_2 MFs and CeO_2 NPs. The tendency in the salt-induced aggregation of MnO_2 MFs (100 mg/L and pH 9.0) is shown in **Figure 27(c)**. Similar to latex particles, the increase in the ionic strength gradually decreased the stability ratio and the magnitude of the zeta potential as a result of charge screening, and the subsequent predominance of the vdW forces, which led to systematically higher aggregation rates. The CCC occurred at 12.2 mM and indicates rather low stability of bare MnO_2 MFs in media of significant salt content.

Table 6: The optimal experimental conditions, as well as size and charge data together with CCC values of the prepared nanozymes (PB, MnO_2, CeO_2) and latex particles (AL, and SL).

Particle	R_h (nm)[a]	PDI (%)[a]	ζ (mV)[a]	$C_{material}$ (mg/L)[a]	pH[a]	Salt[a]	σ (mC/m^2)[a,b]	CCC (mM)[b]
PB	42	23.5	-19.7	100	4.0	KCl	-	-
MnO_2	83	11.9	-37.0	50	9.0	NaCl	-5.2	12.2
CeO_2	181.2	28.0	32.7	50	4.0	NaCl	23.0	79.1
CeO_2	180.0	28.7	-29.2	50	9.0	NaCl	-4.7	5.1
AL	249	13.4	61.2	25	4.0	KCl	15.0	58.9
SL	441	20.9	-73.1	125	9.0	NaCl	-15.0	224.5

[a]R_h: hydrodynamic radius, PDI: polydispersity index, ζ: zeta potential, σ: surface charge density. These parameters are obtained at the $C_{material}$ as well as the designated pH and 1.0 mM ionic strength, using the designated salt. [b]The σ values were obtained by fitting the Grahame relation, equation (16), with the ζ data in **Figure 27**, while the CCC values were obtained from stability ratio data in **Figure 27** using equations (37) and (38), as shown in **Appendix C**.

For CeO_2 NPs systems (100 mg/L), the salt-induced aggregation was assessed both at pH 4.0 and 9.0. In the acidic regime, where the particles are positively charged (**Figure 27(d)**), increasing the salt content gradually decreased the stability ratio of CeO_2 NPs dispersions until it reached unity at a NaCl concentration of 79.1 mM, the CCC. In addition, the CeO_2 NPs exhibited high zeta potential at low ionic strength due to deprotonated OH groups, the surface charge was increasingly screened with the increase of salt content, which is reflected in the gradual drop in the zeta potential. The trends at pH 9.0 were similar, as shown in **Figure 27(e)**.

However, the CCC occurred at 5.1 mM, indicating lower colloidal stability of CeO_2 NPs in alkaline media, which can be attributed to the lower magnitude of zeta potential, compared to pH 4. The CCC values of the latex and nanozymes system are listed in **Table 6**.

The examination of the CCC values reveals that the latex particles form more highly stable systems than the nanozymes. The significantly charged surfaces of SL and AL result in high initial zeta potential, and thus, higher salt concentration is needed to induce heavy aggregation and bring about the destabilization of the system. In addition, the fits of the Grahame relation in **Figure 27** show significant deviation from the experimentally obtained zeta potential values, especially at low ionic strength. Also, the deviation is more emphasized in nanozymes rather than in latex particles. A prime reason for such deviations is that the Grahame equation relates the *surface* charge to the *surface* potential rather than the zeta potential, and thus, a deviation is expected. The deviation is more evident for commercial AL particles, where the estimated σ was 15.0 mC/m^2, while the manufacturer reported σ is 197.0 mC/m^2. In addition, because the Debye length of the EDL is large at low ionic strength, the difference in the zeta and surface potential is expected to be substantial. Hence, the σ values in **Table 6** are a mere approximation and do not accurately reflect the actual charge status on the particles, since σ is obtained by selecting the best Grahame fit to the relevant experimental data. Nevertheless, particles with high zeta potential have high surface charge density and require higher ionic strength (higher CCC) to induce heavy aggregation.

5.3 Nanoparticle functionalization

The formulation of composites requires the heteroaggregation of negatively charged SL particles with either of the negatively charged metal oxides (MnO_2 or CeO_2). The composite formation, however, is expected to be hindered due to electrostatic repulsion. To enable the formulation under the influence of the electrostatic attraction, the metal oxide particles were surface modified with positively charged PDADMAC polyelectrolyte to induce charge reversal on the metal oxides. The PDADMAC is a water-soluble and highly charged cationic polymer, such polyelectrolytes are commonly used in water treatment, papermaking, and processing of minerals, and are known to strongly adsorb onto oppositely charged surfaces.[123, 195, 196] The proper amount of polyelectrolyte is not arbitrary, and hence, it was determined by systematically observing the aggregation rate and zeta potential of the metal oxide particles at various amounts of added PDADMAC. **Figure 28(a, b)** show the stability ratio and the zeta potential of PDADMAC-functionalized MnO_2 MFs (PMn) and PDADMAC-functionalized CeO_2 NPs (PCe) at various PDADMAC doses (expressed in mg PDADMAC/g metal oxide).

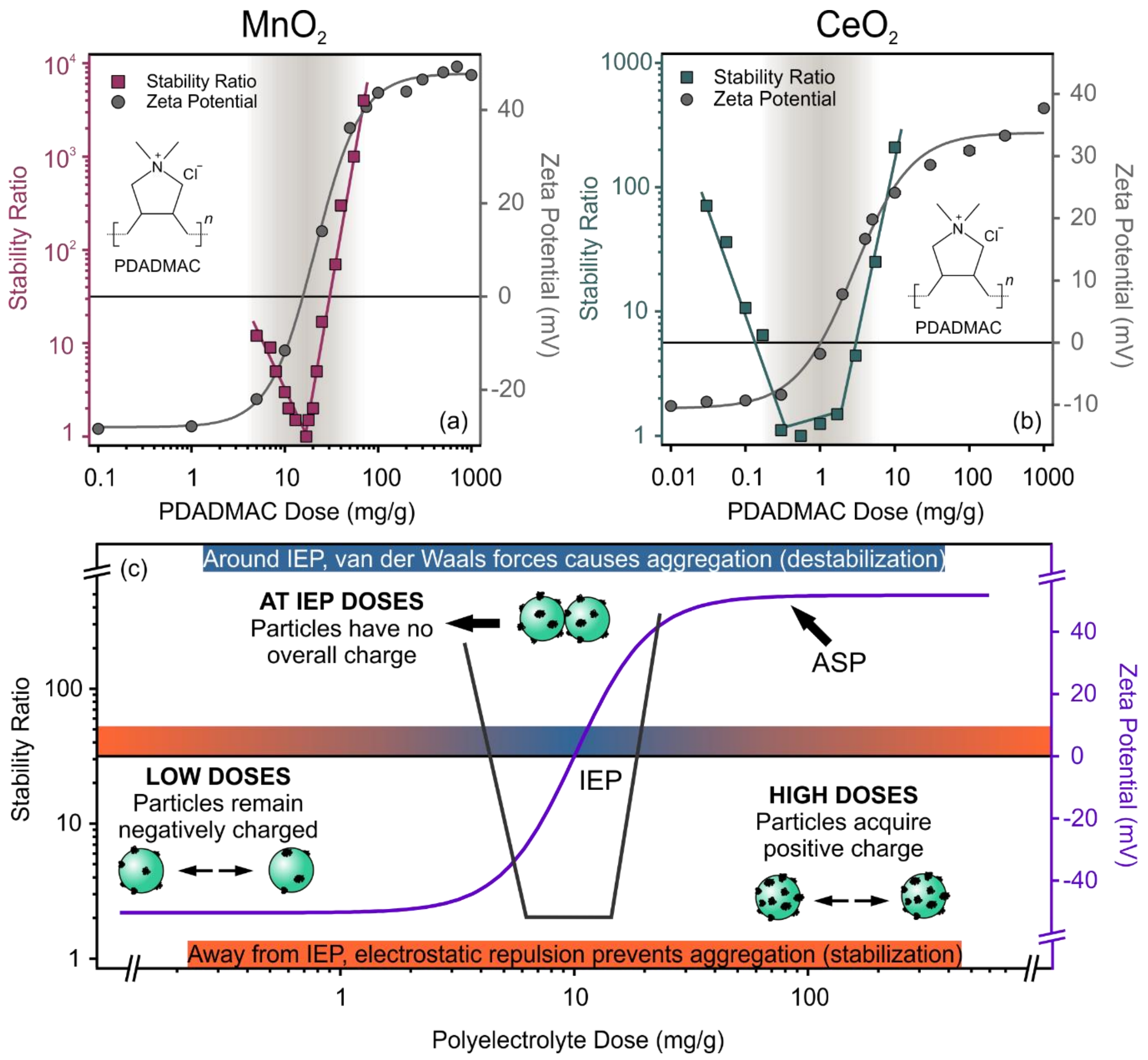

Figure 28. Stability ratio (squares) and zeta potential data (circles) of (a) MnO_2 MFs and (b) CeO_2 NPs in the presence of different amounts of PDADMAC polyelectrolyte at pH 9.0 and 1.0 mM ionic strength, using NaCl. In both systems, the metal oxide concentration was fixed at 100 mg/L. The solid lines serve as eye guidance. The polyelectrolyte concentration is expressed in mg PDADMAC/g metal oxide. (c) The general trend in the change of the stability ratio and the zeta potential for particle-polyelectrolyte systems at various polyelectrolyte concentrations.

Figure 28(c) shows the general trends in the stability ratio and zeta potential values for the obtained particle-polyelectrolyte systems. At low polyelectrolyte doses, the metal oxide particles maintained their negative charge, which gradually decreased in magnitude as higher doses of PDADMAC were introduced into the system. Both systems exhibited an IEP, at which the total positive charge of adsorbed PDADMAC is balanced by the negative surface charge of metal oxide particles, resulting in functionalized metal oxide particles with no overall charge. Higher PDADMAC doses than those around the IEP gave rise to positively charged functionalized metal oxide particles, and the magnitude of the positive charge increased with increased PDADMAC doses until the surfaces are saturated with PDADMAC, where additional

PDADMAC caused no change in the zeta potential values, as indicated by the adsorption saturation plateau (ASP). Moreover, the corresponding aggregation rates, expressed in the stability ratio, at various PDADMAC doses reflect the trends in the zeta potential. Accordingly, when metal oxide particles have a high overall charge (well below and above the IEP), the stability ratio is high, indicating stabilized dispersions. Around the IEP, however, the zeta potential of particles is significantly low, i.e., <25 mV, and thus, the systems undergo heavy aggregation resulting in low stability ratio values.

The above colloidal behavior can be interpreted by elucidating the nature of the interparticle forces involved. In such polyelectrolyte-particle systems, two regimes of forces exist. First, the forces that lead to the adsorption of PDADMAC onto metal oxides, and second, the forces that govern the interactions among the functionalized metal oxide particles. The adsorption of PDADMAC is brought about by vdW and electrostatic attraction forces (DLVO forces) between surface moieties on the metal oxides and functional groups of the charged PDADMAC. Once the particles are functionalized, the stability of the system is governed by the second forces regime of vdW and electrostatic repulsion forces, as shown in **Figure 28(c)**. The relative contribution of both forces is dependent on the PDADMAC dose. Around the IEP, the extremely low zeta potential and the subsequent heavy aggregation rate indicate that the vdW forces are dominant. However, when the overall charge is high (low and high PDADMAC doses), the high stability ratio can be attributed to electrostatic repulsion between adsorbed PDADMAC chains on the approaching particles.

The interactions of adsorbed PDADMAC chains with neighboring metal oxide particles can occur via electrostatic or electrosteric repulsion, depending on the way the PDADMAC is adsorbed. When PDADMAC is adsorbed as unfolded chains that extend into the dispersion medium, the stabilization at high or low doses is caused by electrosteric repulsion. On the other hand, when PDADMAC is adsorbed randomly as coiled chains, the resulting patches give rise to stability via electrostatic repulsion among patches of interacting particles. In addition, when the surface of particles is partially covered with PDADMAC patches, the aggregation that occurs at the IEP of the system might involve patch-charge attractions between positive PDADMAC patches as well as the negative surface on neighboring particles. In **Figure 28(a),** the lower values of stability ratio at doses below the IEP, where the MnO_2 MFs are partially covered with PDADMAC, suggest the possible involvement of patch-charge attractions that gave rise to higher aggregation rates and lower stability ratios. Schematic illustrations of these forces are shown in **Figure 8**.

The PDADMAC functionalization of MnO_2 MFs (**Figures 28(a)**) was probed at pH 9.0 in the dose range 0.1-1,000 mg PDADMAC/g MnO_2 at 1.0 mM NaCl and 100 mg/L MnO_2 MFs. The IEP and ASP of the PMn system occurred at 20 mg/g and 100 mg/g, respectively. As for CeO_2 NPs (**Figures 28(b)**), however, the functionalization was carried out within the PDADMAC dose range of 0.01-1,000 mg PDADMAC/g CeO_2 at 1.0 mM NaCl and 100 mg/L CeO_2 NPs. The IEP of the PCe system occurred at 1.0 mg/g, which is much lower than that for the MnO_2 system, while the onset of the ASP occurred at a PDADMAC dose of around 10.0 mg/g.

Similar tendencies in particle-polyelectrolyte systems have been reported in the literature. For example, Borkovec et al. probed the adsorption of PDADMAC on commercial SL particles (-10 mC/m^2). At 1.0 mM KCl, the IEP and ASP of the system occurred at around 2.3 mg/g and 4.0 mg/g, respectively, when the SL concentration was 8.0 mg/L.[131] Also, Bauer et al. studied the colloidal behavior of silica in the presence of PDADMAC among other polyelectrolytes. For 50 mg/L silica dispersion at 1.0 mM NaCl, the system exhibited similar charging trends with an IEP around a PDADMAC dose of 1.0 mg/g.[197] **Table 7** summarizes the results of the formation of several particle-polyelectrolyte systems reported in the literature. Generally, low doses of PDADMAC are required to cause charge neutralization indicating that such polyelectrolytes are highly effective in the adjustment of surface charge. However, the surface saturation with PDADMAC can vary widely, reaching two orders of magnitude in some systems such as (-)-titania and silica particles, as shown in **Table 7**.

Table 7: The characteristic parameters for polyelectrolyte adsorption for various particle-polyelectrolytes systems reported in the literature.

Particle	**Polyelectrolyte**	**$C_{particle}$ (mg/L)**	**pH**	**I^* (mM)**	**Salt**	**IEP (mg/g)***	**ASP (mg/g)***	**Ref.**
MnO_2	PDADMAC	100	9.0	1.0	NaCl	20.0	100	Present work
CeO_2	PDADMAC	100	9.0	1.0	NaCl	1.0	10.0	Present work
SL	PDADMAC	8.0	4.0	1.0	KCl	2.3	4.0	131
Silica	PDADMAC	50	4.0	1.0	NaCl	1.0	2.6	197
(+)-Titania	(-)PSS*	1.0	4.0	1.0	NaCl	5.0	50	198
(-)-Titania	PDADMAC	1.0	10	1.0	NaCl	30	150	198
(-)-Titania	PDADMAC	1.0	7.0	4.5	NaCl	~22	~42	199
(+)-LDH	(-)PSS*	10	-	10	NaCl	7.0	100	200

*The PSS refers to poly(styrene sulfonate), I refer to the ionic strength, and the mg/g unit for the IEP and ASP refers to mg polyelectrolyte/g particle.

For the PMn and PCe, systems, the selected PDADMAC dose should give rise to highly charged particles and should not occur well within the ASP, since free PDADMAC in dispersions of saturated particles could give rise to depletion interactions.[201] Thus, the selected

PDADMAC dose for PMn is 200 mg/g, at which the corresponding zeta potential of 44.0 ± 0.4 mV. Also, the selected PDADMAC dose for PCe is 40 mg/g, with a zeta potential of 32.0 ± 0.4 mV. These doses were used when the functionalized metal oxides were immobilized onto SL particles during the composite formulation.

5.4 Composite formulation

5.4.1 Nanozyme immobilization

Four different composites (AL-PB, SL-PMn, SL-CeO_2, and SL-PCe) were prepared at designated conditions (pH, ionic strength, and latex concentration). The composite formulation was achieved via heteroaggregation between latex particles (AL or SL) and the oppositely charged designated nanozymes (PB, PMn, CeO_2, or PCe) under the influence of vdW and electrostatic attractive forces. Like particle-polyelectrolyte systems, the formation of particle-particle systems exhibited trends characterized by charge neutralization followed by charge reversal when the nanozyme dose was systematically changed. The similarity between charging and aggregation trends induced by either polyelectrolytes or nanozymes is striking once **Figures 28 (c)** and **Figure 29** are compared.

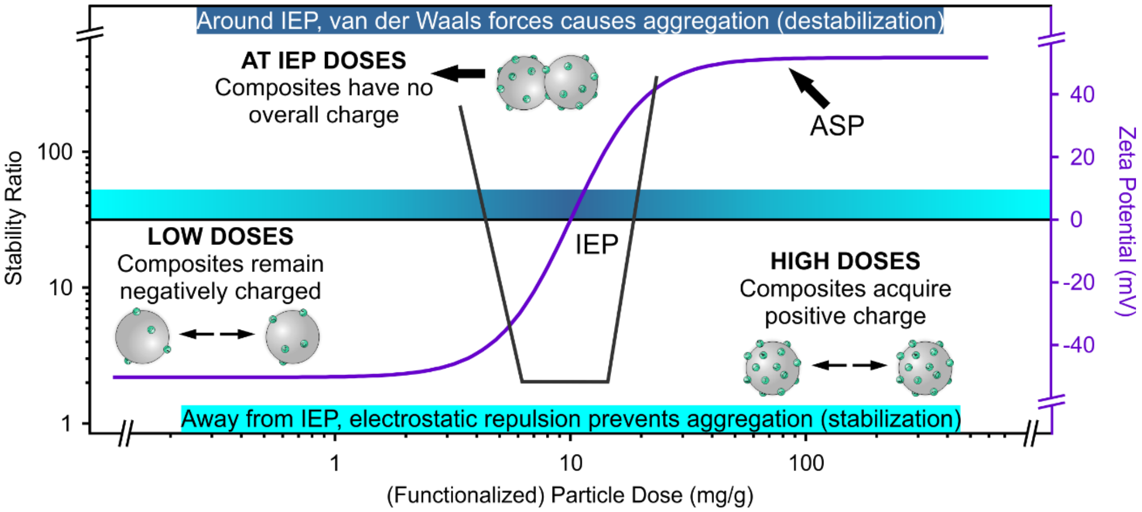

Figure 29. The typical immobilization curve (the trend in the stability ratio and zeta potential upon addition of nanozymes to latex dispersions) for the latex-nanozyme system at fixed latex concentration and ionic strength.

Hence, for a given latex concentration, the change in the stability ratio and the zeta potential is monitored at various nanozyme doses (in mg nanozyme/g latex). The obtained immobilization curve for particle-particle systems, e.g., latex-nanozyme, is shown in **Figure 29**. When the nanozyme doses are low, the latex-nanozyme composites maintained the latex's original charge that tangibly decreased in magnitude when the introduced dose of nanozyme was raised. Also, all the latex-nanozyme composites are characterized by an IEP dose, where the surface charge of the latex was balanced by that of the immobilized nanozyme, giving rise to neutrally charged hybrid particles. When the nanozyme dose was higher than those around the IEP, the latex-nanozyme system undergoes a charge reversal, where the opposite charge continues to increase in magnitude until the surface of latex particles becomes saturated with nanozymes, where the addition of further nanozymes does not lead to change in the zeta potential, resulting in a characteristic ASP. In addition, the trend in the stability ratio at the corresponding nanozyme doses was in line with that of the zeta potential. As shown in **Figure 29**, the high overall charge of latex-nanozyme particles (at low and high nanozyme doses) resulted in high stability ratio values giving rise to stable composite dispersions. On the other hand, nanozyme doses corresponding to those around the IEP led to heavily aggregating systems (low stability ratio) since the overall charge of the hybrid particles corresponds to very low zeta potential values, i.e., <25 mV.

The trend in the charge neutralization and reversal is explained by interpreting the underlying interparticle forces. Since the particles are initially highly charged, the homoaggregation is prevented or at least minimized. Like polyelectrolyte-particle systems, two regimes of interaction forces exist in the latex-nanozyme systems. First, the forces responsible for the immobilization of the nanozymes onto the respective latex, whereas the second regime refers to the forces that control the interactions among the individual latex-nanozyme hybrid particles. In the first interaction regime, DLVO-type forces of vdW and electrostatic attraction give rise to latex-nanozyme composites. The surfaces of SL and AL are functionalized with sulfate and amidine groups, respectively, which give rise to electrostatic interactions. The carbon skeletal of the polystyrene, on the other hand, contributes to attractive vdW interactions with nanozymes. As for nanozymes, both surface lattice components and (de)protonated –OH groups, as well as the adsorbed PDADMAC chains, give rise to electrostatic interactions that enable their immobilization onto latex particles.

However, once nanozymes are immobilized, the stability of the system is governed by the second regime of interactions with varying contributions of DLVO and possibly non-DLVO type forces, depending on the nanozymes dose. As shown in **Figure 29**, when the overall charge of the latex-nanozyme hybrid particles is high (low and high nanozyme doses), the observed colloidal stability (high stability ratio) is attributed to electrostatic repulsion among (PDADMAC-functionalized) nanozymes on the interacting hybrid particles. Around the IEP, however, the vdW forces dominate the total interaction resulting in rapid aggregation, as the hybrid particles have low or zero zeta potential. In addition, in partially covered systems, the parch-charge attractions, besides vdW forces, *might* contribute to the destabilization of the system at the IEP, where the attractions occur between the negatively charged SL and isolated positive PDADMAC patches on the oxide of the interacting hybrid particles.

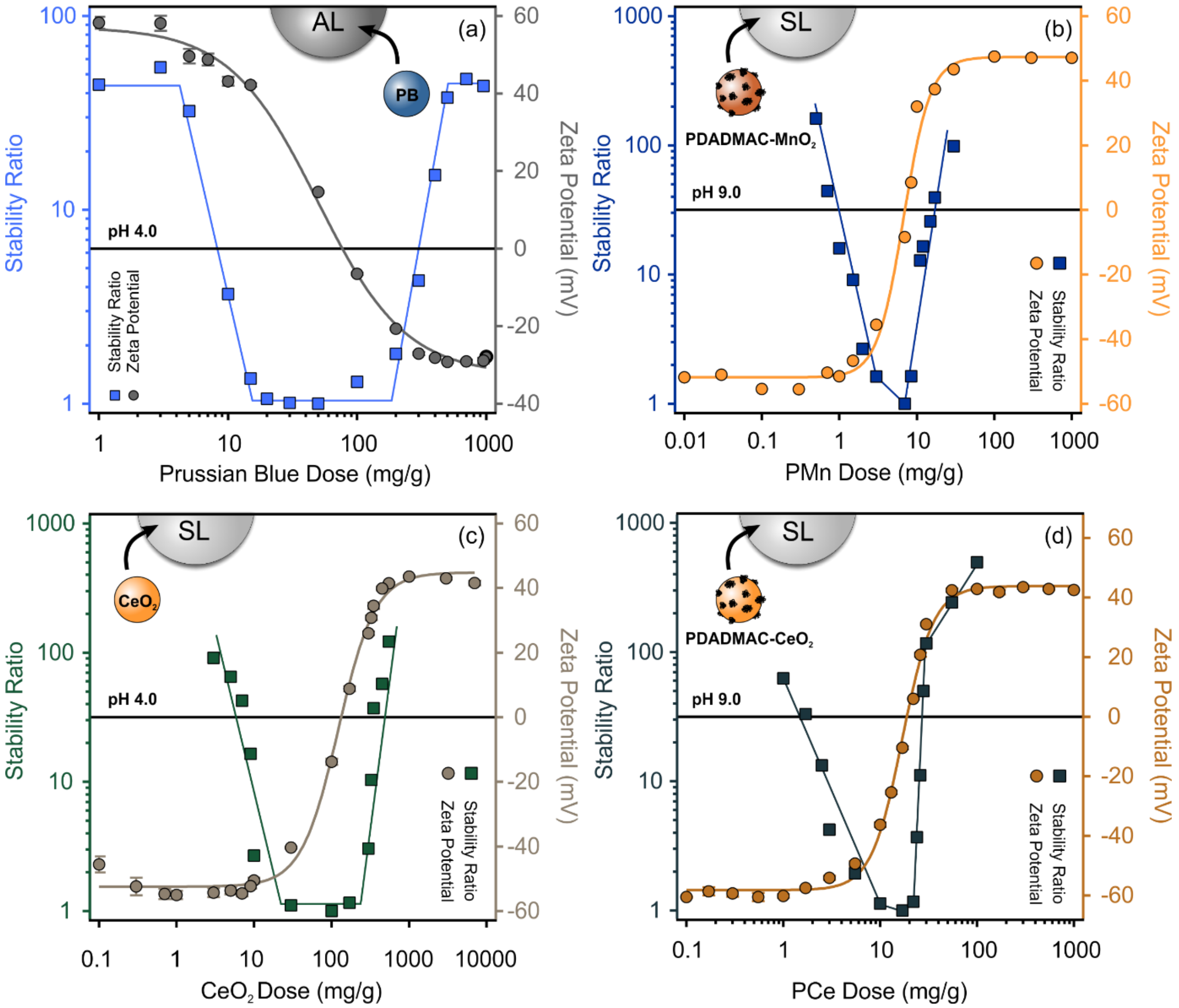

Figure 30. Trends in stability ratio (squares) and zeta potential values (circles) of (a) AL-PB (b) SPMn (c) SL-CeO$_2$ and (d) SPCe composites as a function of the nanozyme dose. The concentration of SL and AL were kept at 125 mg/L and 25 mg/L, respectively. The ionic strength was fixed at 1.0 mM in all systems. The mg/g unit refers to mg nanozyme/g latex. The solid lines are added for eye-guidance purposes only.

As shown in **Figure 30(a)**, the AL-PB system was formulated at pH 4.0 and 1.0 mM KCl with a fixed AL concentration of 25 mg/L and within the PB dose range of 1-1,000 mg PB/g AL. The IEP occurred around 76.6 mg/g and the onset of the ASP occurred at 300 mg/g. The SL-PMn (SPMn) system, **Figure 30(b)**, was formulated at pH 9.0 and 1.0 mM NaCl at constant SL concentration (125 mg/L). The PMn dose was altered between 0.01 and 1,000 mg PMn/g SL. The IEP occurred around 7.1 mg/g and the onset of the ASP occurred at 30.0 mg/g. The dose of PDADMAC in PMn was selected at 200 mg PDADMAC/g MnO$_2$, based on the

PDADMAC adsorption measurements. For the formation of SL-CeO$_2$ at pH 4.0 and 1.0 mM NaCl (**Figure 30(c)**), the CeO$_2$ NPs dose was altered in the range 0.1-10,000 mg CeO$_2$/g SL at constant SL concentration (125 mg/L). The SL-CeO$_2$ system exhibited an IEP around 100 mg/g and an ASP, whose onset occurred around 1,000 mg/g. On the other hand, the SL-PCe (SPCe) system was heteroaggregated at pH 9.0 and 1.0 mM NaCl at constant SL concentration (125 mg/L), as shown in **Figure 30(d)**, where the PCe dose was altered in the range 0.1-1,000 mg PCe/g SL. The IEP of SPCe composite occurred at 16.0 mg/g and the onset of the ASP occurred around 55.0 mg/g. The dose of PDADMAC in PCe is selected at 40.0 mg PDADMAC/g CeO$_2$, based on the PDADMAC adsorption measurements. Optimal nanozyme doses should result in highly charged hybrid particles. Thus, the selected dose for AL-PB, SPMn, SL-CeO$_2$, and SPCe were 600, 100, 1000, and 200 mg nanozyme/g latex, respectively. These doses were used when the composites with enzyme-like catalytic potential were investigated. **Table 8** summarizes the parameters leading to the latex-nanozyme composites with the desired composition.

Table 8: The optimal experimental conditions for the formulation of the latex-nanozyme composites.

System	C$_{latex}$ (mg/L)^a	pH^a	Salt^a	NZ dose (mg/g)^{a,b}	IEP (mg/g)^b	ASP (mg/g)^b	Selected dose (mg/g)^b	PNz dose (mg/g)^c
AL-PB	25	4.0	KCl	1.0-1,000	76.6	300.0	600	-
SPMn	125	9.0	NaCl	0.1-1,000	7.1	30.0	100	200
SL-CeO$_2$	125	9.0	NaCl	0.1-10,000	100	1000	200	-
SPCe	125	4.0	NaCl	0.1-1,000	16.0	55.0	100	40

^{a}The composites were formulated at the respective latex concentration (C$_{latex}$) and pH, using the designated salt, and within the given nanozyme (NZ) dose range. ^{b}The mg/g unit in the NZ dose, IEP, ASP, and the selected dose refers to mg nanozyme/g latex. The selected dose is the optimal nanozyme content, selected in the final composites. ^{c}The PNz dose refers to the PDADMAC doses in PMn and PCe, expressed in mg PDADMAC/mg nanozyme.

The examination of the trends in **Figure 30** and resulting values in **Table 8** reveals several interesting observations. First, the presence of PDADMAC led to a significant reduction in the value of the IEP and the ASP. For example, for the same SL concentration (125 mg/L), the IEP and ASP for SL-CeO$_2$ are 6.25 and 18.1 times larger than those for SPCe, respectively. Therefore, the SPCe are expected to be less decorated with functionalized CeO$_2$ NPs compared to the extent of decoration of SL-CeO$_2$ composite with bare CeO$_2$ NPs. On the other hand, SPCe and SPMn exhibited close IEP and ASP values for the given SL concentration. Also, both AL-PB and SL-CeO$_2$ exhibited higher IEP and ASP values, compared to SPCe and SPMn. Such observations indicate that the PDADMAC is highly effective not only in the charge modification of the nanozymes but also in lowering the SL capacity to accommodate more nanozyme, resulting in partially covered systems. In addition, the high stability ratios of SPCe and SPMn at low/high nanozyme doses suggest the absence of patch-charge interactions.

5.4.2 *Composite visualization*

The formulated composites were visualized with TEM, SEM, AFM, and Raman spectroscopy. **Figure 31** shows TEM and SEM images for the AL-PB composite at PB doses below, at, and above the IEP of the AL-PB composite, namely at 1.0, 30, and 600 mg PB/g AL, respectively. The images show that the amount of immobilized PB is increased as the PB dose increases. At 600 mg/g, the selected dose in **Table 8**, the PB NPs are uniformly distributed on the surface of AL, and therefore, the 600 mg/g is an ideal dose for a fully coated AL-PB composite with foreseen antioxidant potential since it also corresponds to highly charged particles.

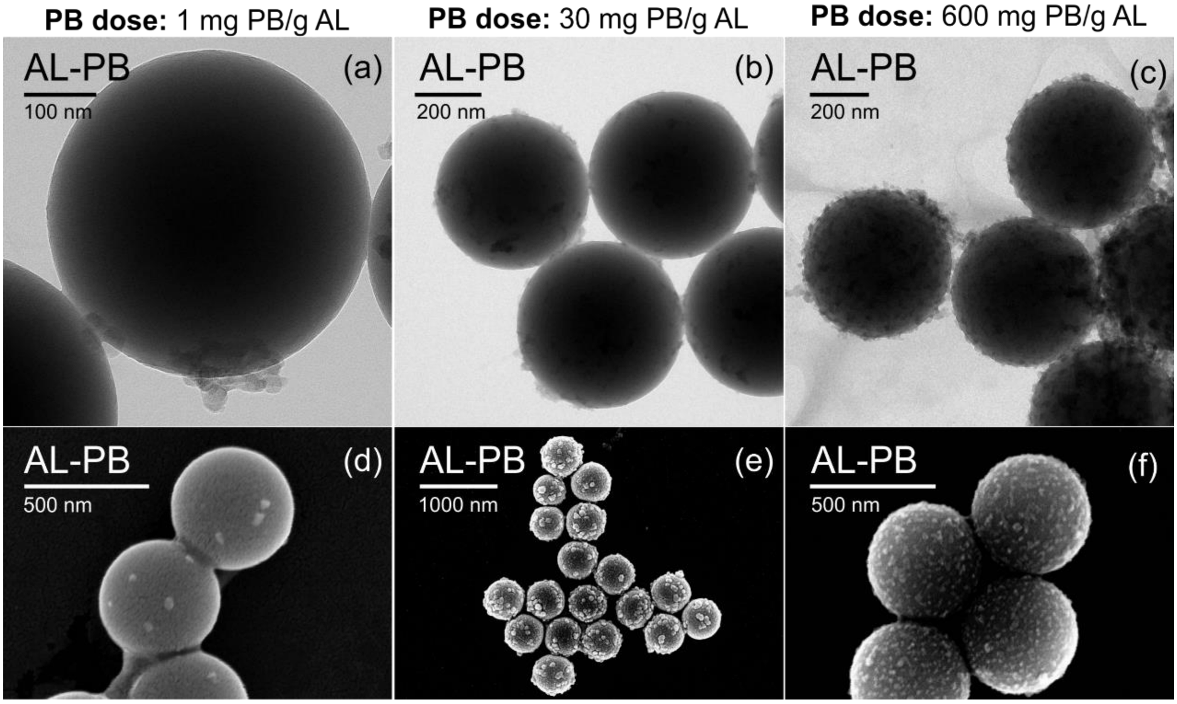

Figure 31. (a-c) SEM and (d-f) TEM images of AL-PB composites at PB doses of 1.0 mg PB/g AL, 30 mg PB/g AL, and 600 mg PB/g AL corresponding to doses (a, d) below (b, e) at, and (c, f) above the IEP of the AL-PB system, respectively.

Similarly, the TEM images of SPMn in **Figure 32(a, b, c)** were captured at PMn doses of 0.1, 10, and 100 mg PMn/g SL, corresponding to concentrations below, around, and above that of the IEP. The TEM images clearly prove the successful immobilization of PMn on SL, with a higher amount of immobilized PMn at higher PMn doses. As predicted from the immobilization curves, the SPMn particles were not covered to the same extent as AL-PB, due to the presence of PDADMAC, i.e., the neutralization of SPMn required rather few PMn particles. In addition, AFM images in **Figure 32(d, e)** also proved the formation of SPMn composites (100 mg PMn/g SL) along with the height profiles. The obtained AFM images also show the limited coverage of the SPMn composite.

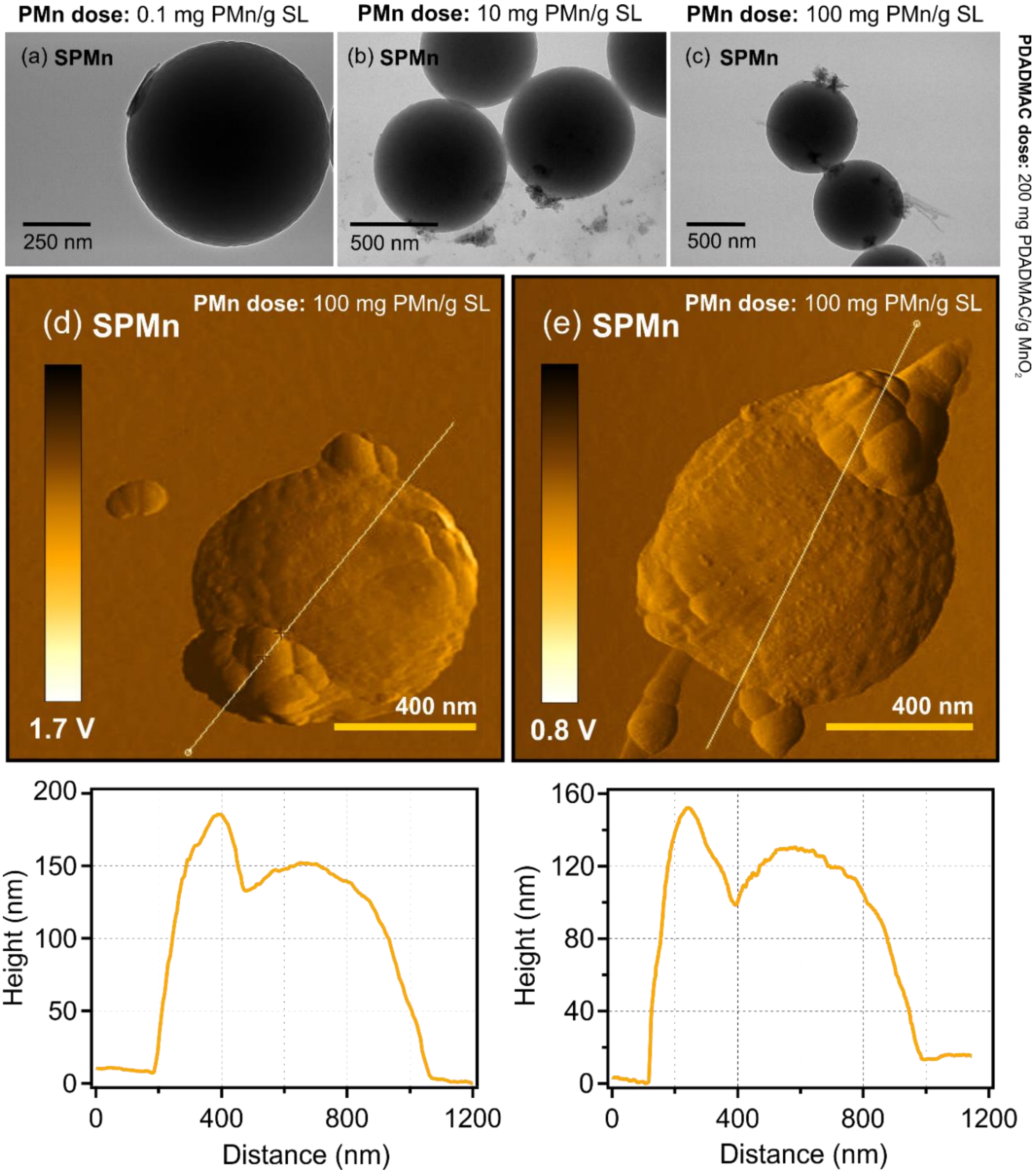

Figure 32. TEM images of SPMn composites at different PMn doses of 0.1 mg PMn/g SL, 10 mg PMn/g SL, and 100 mg PMn/g SL, corresponding to doses (a) below (b) at, and (c) above the IEP of the SPMn system, respectively. (d, e) Amplitude AFM images along with height profiles. The different samples were prepared at 125 mg/L SL, and 200 mg PDADMAC/g MnO_2 (the onset of ASP in the adsorption curve in **Figure 28(a)**).

The formulation of the SL-CeO_2 composite was successfully visualized via TEM and AFM techniques as well. The TEM images in **Figure 33(a, b)** provide direct evidence of the immobilization of CeO_2 NPs on the SL particles at 1,000 mg CeO_2 /g SL, where CeO_2 NPs are heavily and uniformly distributed on the surface of SL. Also, the examination of SL-CeO_2 composite morphology via AFM images (**Figure 33(c, d)**) reveals similar observations, the CeO_2 NPs are uniformly immobilized onto SL particles, as evidenced by the height profiles as well (**Figure 33(e)**).

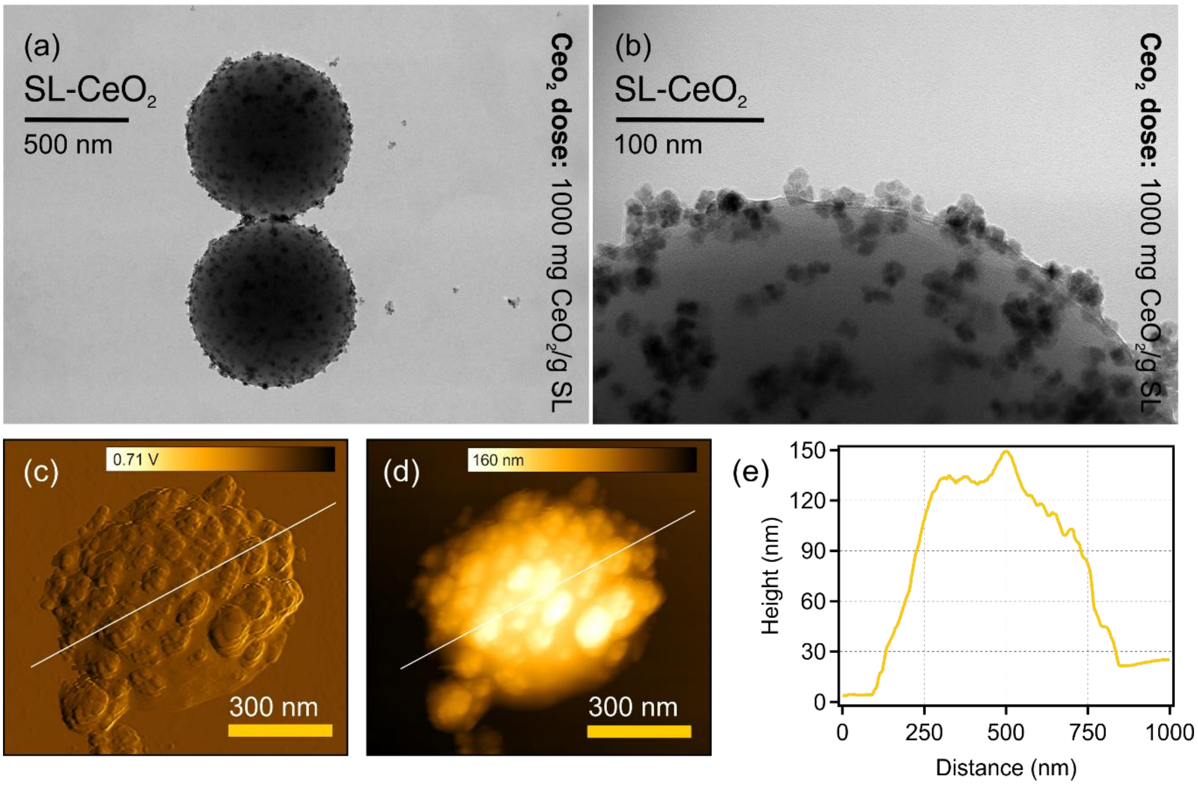

Figure 33. (a,b) TEM images, as well as (c) amplitude and (d) height AFM images, of SL-CeO_2 composite deposited on a mica substrate along with (e) the height profile, corresponding to the regions indicated by the white lines. The sample was 100 mg/L in SL with 1,000 mg CeO_2/g SL (the onset of the ASP of the immobilization curve of the SL-CeO_2 system in **Figure 30(c)**).[192]

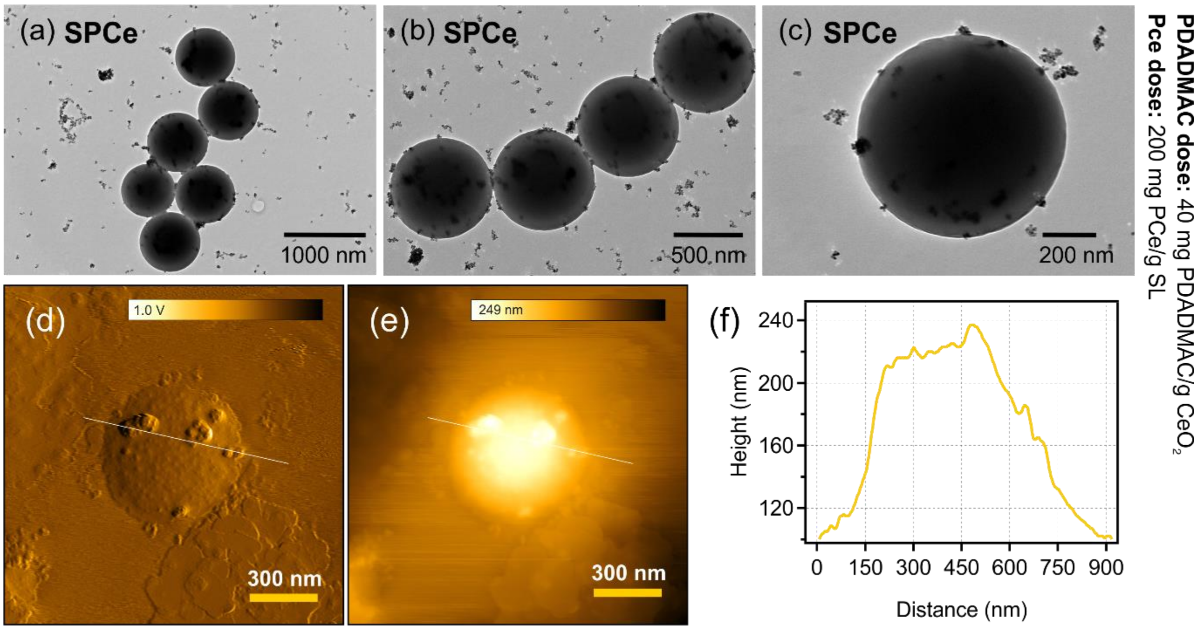

Figure 34. (a-c) TEM images of SPCe at different magnifications. (d) Amplitude and (e) height AFM images of SPCe deposited on a mica substrate along with (f) the height profile, corresponding to the regions indicated by the white lines. The SL concentration was 100 mg/L, with 40.0 mg PDADMAC/g CeO_2 (the onset of ASP in the adsorption curve in **Figure 28(b)**) and 200 mg CeO_2/g SL (the onset of ASP in the immobilization curve in **Figure 30(d)**).[192]

Finally, the formation of the SPCe composite, at pH 9.0, was visualized with TEM and AFM techniques. The TEM images in **Figure 34(a, b, c)** clearly show that the PDADMAC-functionalized CeO_2 NPs adsorbed on the latex, as shown by the amplitude and height AFM images of SPCe **Figure 34(d, e)** system along with the height profile (**Figure 34(f)**). For the SPCe system captured, the PDADMAC dose was 40.0 mg/g (the onset of the ASP in **Figure 28(b)**), and the CeO_2 NPs dose was 200 mg/g (the onset of the ASP in **Figure 30(d)**). Once again, the coverage of SL in SPCe is comparable to that in the SPMn. Also, the SPCe is not covered to the same extent as SL-CeO_2 and AL-PB composites, as predicted earlier.

Thus, the presence of the PDADAMC had a certain and significant effect on the extent of coverage of the composites. In fact, the IEP values of the SL-CeO_2 and SPCe systems occurred at 100 mg/g and 16.0 mg/g, respectively, even though the CeO_2 NPs and PCe doses used in the imaged sample correspond to doses at the onset of the ASP, where the two saturated systems had similar SL concentration (125 mg/L). Therefore, the SPCe particles were found to be less decorated with functionalized CeO_2 NPs compared to those of the SL-CeO_2 composite. Thus, the PDADMAC is indeed highly effective not only in the surface charge modification of nanozymes but also in lowering the SL capacity to accommodate a larger number of nanozyme particles, resulting in partially covered systems.

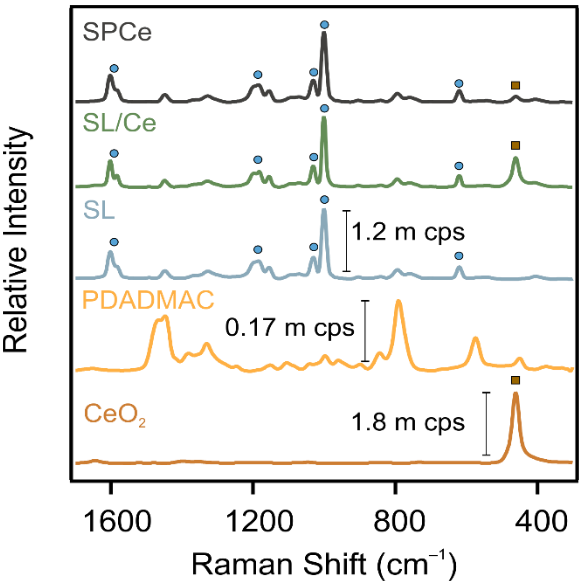

Figure 35. Raman spectra of CeO_2, SL, PDADMAC, SL-CeO_2, and SPCe. Raman peaks marked with squares refer to CeO_2, while those marked with circles refer to SL. The absolute Raman intensities (prior normalization) are shown, intensity unit "m cps" refers to 10^6 counts per second.

In addition, the formation of CeO_2-based composites was verified via Raman spectroscopy. The individual Raman spectra of CeO_2, PDADMAC, and SL were recorded. As shown in **Figure 35**,[192] the characteristic peaks in the Raman spectrum of SL at 620 cm^{-1} and 1000 cm^{-1} can be attributed to various deformation mode bands of the aromatic rings, while those at 1150–1200 cm^{-1} and 1602 cm^{-1} are attributed to stretches in the C–C and the ring skeletal, respectively. The recorded peaks agree very well with those reported elsewhere in the literature.[202] On the other hand, the Raman spectrum of PDADMAC revealed peaks identified as the N–C stretches (790 cm^{-1}) and CH_3 stretching vibration (1449 cm^{-1}).[203] The vibrational modes that give rise to Raman peaks, assigned for SL and PDADMAC, are listed in **Table S3** (**Appendix D**). In addition, the recorded spectra of SL-CeO_2 and SPCe revealed the lone peak of CeO_2 (indicated by squares) and all characteristic Raman peaks of SL (indicated by circles), as shown in **Figure 35**. Compared to the individual spectra, no observable shift in the peak positions was observed. However, the immobilization resulted in weakened peak intensities of CeO_2 but have no effect on the intensities of SL peaks. On the other hand, the absence of characteristic peaks of PDADMAC in the spectrum of SPCe is attributed to the lower Raman intensity of PDADMAC (recorded intensity values are labeled on the graph).[203]

Hence, highly stable latex-nanozyme composites were systematically formulated under controlled heteroaggregation that not only maximized the electrostatic attraction within the latex-nanozyme composites but also maximized the repulsion among the individual highly charged hybrid particles, resulting in colloids of high colloidal stability with promising antioxidant potential.

5.5 The enzyme-like activity

The enzyme-like catalytic potential of the formulated composites was examined via standardized enzyme assays. The AL-PB composite was found to have SOD-like and HRP-like activity, while SPMn mimicked both CAT and SOD enzymes. For CeO_2-based composites, HRP-like activity and radical scavenging potential were observed.

5.5.1 The SOD-like activity of PB- and MnO_2-based composites

The SOD enzyme catalyzes the dismutation of superoxide ($\bullet O_2^-$) into O_2 and H_2O_2, and thus, is an important antioxidant that plays a crucial role in cellular defense in most living cells exposed to ROS. Both AL-PB and SPMn systems showed SOD-like activity, which was confirmed via the Fridovich assay. The inhibition of the NBT-superoxide reaction, obtained using equation (39), is presented as a function of the corresponding nanozyme concentration.

Figure 36(a) shows that inhibition increased with increasing PB concentration. The NBT-radical reaction at 25 °C was completely inhibited at a bare PB concentration of 4.0 mg/L, while the AL-PB composite (600 mg PB/g AL) achieved 65% inhibition when the PB content in AL-PB was 4.0 mg/L. While the immobilization of PB did not compromise its catalytic potential, the AL-PB composite exhibited lower catalytic potential, indicating the decreased availability of the catalytic surface of PB NPs upon immobilization. **Table 9** summarizes the IC_{50} values for the bare and immobilized PB. The IC_{50} values of PB and AL-PB did not differ significantly and were found to be 1.64 mg/L and 2.55 mg/L, respectively. Similar inhibition curves for

SPMn for SOD-like enzymatic potential are shown in **Figure 36(b, c)**. The inhibition increases as the concentration of bare MnO_2 MFs or its content in SPMn was increased up to 2.0 mg/L. The IC_{50} values for SPMn and bare MnO_2 MFs at 25 °C were 0.311 mg/L and 0.274 mg/L, respectively. Hence, the functional integrity of MnO_2 MFs was preserved upon both polyelectrolyte functionalization and immobilization. In addition, the SOD-like activity of MnO_2 MFs and SPMn was evaluated after the stock dispersions were thermally incubated at 50 °C and 75 °C for 90 min. **Figure 36(b, c)** shows the inhibition curve of thermally treated MnO_2 MFs and SPMn at both temperatures. It was found that the heated samples exhibited no loss of SOD-like activity for either bare or immobilized MnO_2 MFs. The native SOD enzyme, on the other hand, was reported to lose its activity after only 20 min of incubation at 80 °C.[46] For native SOD at 25 °C, the IC_{50} value, however, was reported to be 0.07 mg/L,[204] which is lower than that of SPMn and significantly lower than that of the AL-PB composite.

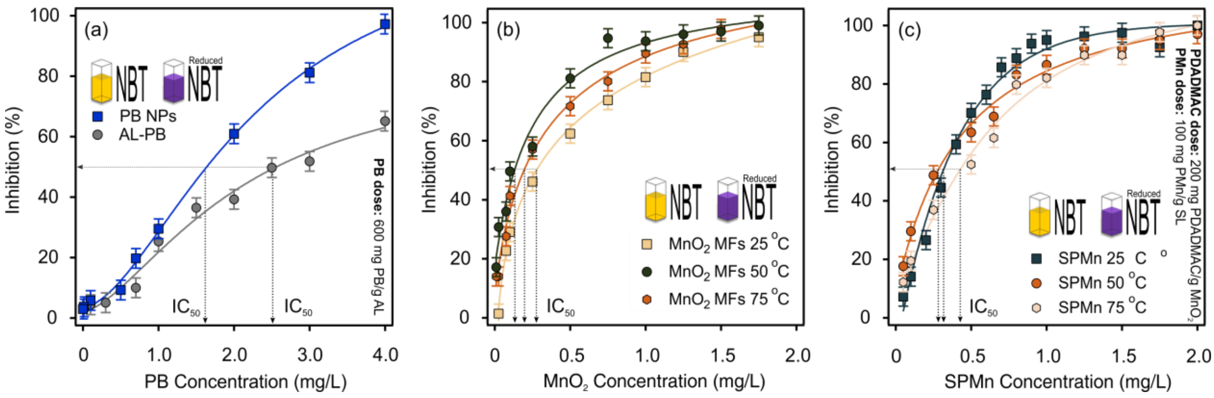

Figure 36. Inhibition of the NBT-superoxide reaction (SOD-like activity) of (a) PB NPs containing samples, (b) bare MnO_2 MFs, and (c) the SPMn composite. The solid lines are mathematical functions used to calculate the IC_{50} values, located by the dashed arrows.

A plausible explanation of the similarity in the SOD-like activity of bare and immobilized MnO_2 MFs is the limited coverage in the SPMn composite and the easier access to the catalytic surface of the immobilized MnO_2 MFs. Although the immobilization of bare MnO_2 MFs inevitably results in the decrease of the area of the available catalytic surface, the heavy aggregation of bare MnO_2 MFs also leads to a loss of some catalytic surface. Hence, the two opposing effects are balanced, resulting in similar SOD-like activity of SPMn, compared to bare MnO_2 MFs. On the other hand, bare PB NPs have high colloidal stability and do not undergo heavy aggregation; however, the full coverage of AL-PB with PB NPs results in significant hindrance of the catalytic surface upon immobilization, and hence, reduced SOD-like activity of AL-PB composite, compared to bare PB NPs. The obtained IC_{50} values suggest excellent SOD-like activity of SPMn, compared to those reported in the literature. For instance, Zhang et al. examined the enzyme-like activity of MnO_2 functionalized with Bovine serum albumin (BSA). The functionalized MnO_2 exhibited 50% inhibition at MnO_2 concentration between 5.0 and 10.0 mg/L.[205] The BSA-MnO_2 showed excellent *in vitro* biocompatibility and effectively inhibited apoptosis.

Table 9: The IC_{50} values of the SOD-like activity assay for PB- and MnO_2-based composites at room and elevated temperatures.

Nanozyme	Dose (mg/g)	IC_{50} (mg/L)
PB-25 °C	-	1.64
AL-PB-25 °C	600 mg PB/g AL	2.55
MnO_2-25 °C	-	0.274 ± 0.012
MnO_2-50 °C	-	0.132 ± 0.005
MnO_2-75 °C	-	0.192 ± 0.010
***SPMn-25 °C**	*200 mg PDADMAC/g MnO_2 100 mg PMn/g SL	0.311 ± 0.013
***SPMn-50 °C**		0.271 ± 0.012
***SPMn-75 °C**		0.417 ± 0.017
Native SOD	-	0.07[204]

Although the enzyme-like activities of MnO_2 MFs and PB NPs, along with their composites, are lower than that of the native enzyme; the composites, especially SPMn, retain high functional and colloidal stability at harsh operational conditions, where the native SOD undergoes permanent loss of activity, and thus, such composites are expected to be ideal candidates as versatile antioxidants with functional stability and economical edge over the sensitive and expensive native SOD enzyme.

5.5.2 The HRP-like activity of PB- and CeO_2-based composites

The PB- and CeO_2-based composites exhibited HRP-like activity by catalyzing the oxidation of some substrates in the presence of H_2O_2. The HRP-like activity of AL-PB and CeO_2-based composites were tested via the guaiacol and TMB assays, respectively. In such assays, the change in color of the added substrate is used to quantitatively probe the enzymatic reaction rate at various substrate concentrations in the presence of the nanozyme. Also, the rate data are fitted with the Michaelis-Menten kinetic model, equation (2).

The HRP-like activity of the PB NPs and AL-PB composite is tested using guaiacol as a substrate. As shown in **Figure 37**, the obtained reaction rate data were plotted as a function of the guaiacol concentration (1-40 mM) at a constant PB NPs concentration (10 mg/L), either in bare or immobilized form. The data was found to fit well with the Michaelis-Menten model. For bare PB, the obtained v_{max} and K_m values were 6.71 μM/s and 2.19 mM, respectively. For AL-PB (600 mg PB/g AL), the PB content corresponds to 10 mg/L in the final samples. The obtained v_{max} and K_m values were 4.09 µM/s and 2.92, respectively. The v_{max} gives the maximum reaction rate observed, after which the rate becomes independent of the substrate concentration and can be attributed to the saturation of the catalytic sites. The K_m, on the other hand, is the guaiacol concentration that corresponds to the rate half that of the v_{max}. The K_m value is inversely proportional to the affinity between the H_2O_2 and PB NPs, with lower K_m indicating a higher affinity. Since the parameters for PB NPs and AL-PB were very similar, it is evident that the immobilization of the PB NPs did not significantly affect their HRP-like activity. The decrease in v_{max}, however, can be attributed to the full coverage of the AL-PB composite, and the subsequent decrease in the availability of the catalytic surface of PB NPs hindered as a result of immobilization. For the native HRP with guaiacol as the substrate, the v_{max} and K_m are 2.80 µM/s and 3.22 mM,[206] which indicates the formulated AL-PB composite had a stronger affinity towards the substrate than the native HRP enzyme, as well as higher v_{max} values.

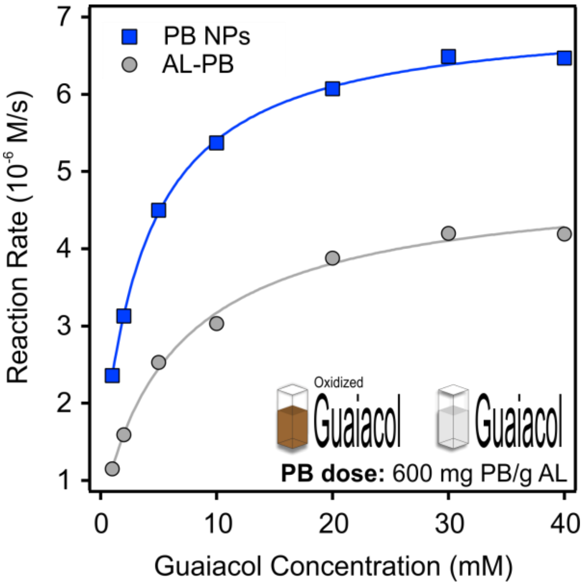

Figure 37. The guaiacol-oxidation reaction rate (HRP-like activity) at different guaiacol concentrations, catalyzed by PB NPs and AL-PB. The lines represent the Michaelis-Menten fits (equation (2)). The graphical schematic inset shows the color of oxidized guaiacol, which indicates positive HRP-like activity for PB NPs and AL-PB.

On the other hand, the HRP-like activity of the CeO_2-based composites was assessed using the TMB substrate, which undergoes oxidation in the presence of H_2O_2 and HRP. The oxidized TMB has a characteristic absorption peak at 652 nm.[207] Unlike guaiacol, however, the TMB substrate is reported to have a pH-dependent response. Thus, the activity of the TMB substrate is assessed at acidic, neutral, and alkaline conditions. **Figure 38** demonstrates the viability of TMB as a substrate for the evaluation of the HRP-like activity of bare CeO_2 NPs. At acidic (pH

4.0) conditions, neither the TMB/CeO_2 (**Figure 38(a)** inset: cuvette α) nor TMB/H_2O_2 (**Figure 38(a)** inset: cuvette β) combination resulted in an absorption peak nor a color change, indicating that no oxidation of TMB took place. For TMB/H_2O_2, the mixture exhibited a very pale blue color indicating an insignificant amount of TMB underwent oxidation, as evident from the very weak absorption peak. The uncatalyzed oxidation of TMB can be attributed to the spontaneous and slow decomposition of H_2O_2 into hydroxyl radicals that can lead to slight TMB oxidation. On the other hand, when TMB, H_2O_2, and CeO_2 NPs are jointly present, the mixture rapidly developed a deep blue color (**Figure 38(a)** inset: cuvette γ) with a strong absorption peak at 652 nm indicating significant oxidation of TMB occurred. When the same measurements are carried out at neutral and alkaline conditions, no color change was observed, and the TMB underwent no oxidation, as shown in **Figure 38(b)**. Thus, the kinetics of the HRP-like activity of CeO_2-based composites were investigated at acidic (pH 4.0) conditions.

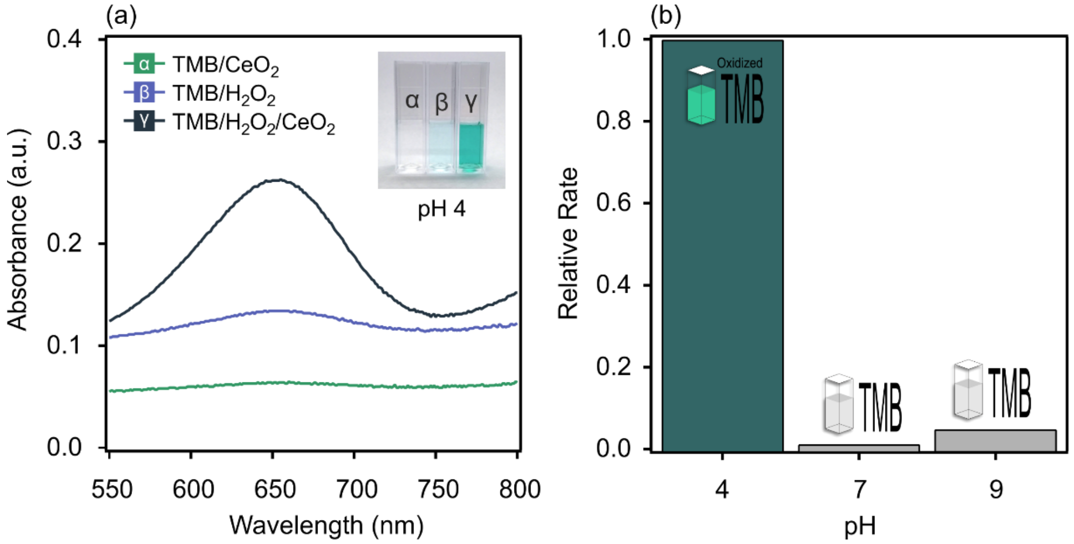

Figure 38. (a) The UV-Vis spectra of TMB/CeO_2 (green/α spectrum), TMB/H_2O_2 (blue/β spectrum), and TMB/H_2O_2/CeO_2 (black/γ spectrum). The inset graphics shows the real samples, measured at pH 4.0. (b) The relative reaction rate of TMB oxidation at acidic (pH 4.0), neutral (pH 7.0), and alkaline (pH 9.0) conditions, the samples were prepared with the following relevant concentrations: 1.0 mM TMB, 25 mg/L CeO_2 NPs, and 5.0 mM H_2O_2.

In addition, the kinetics of the CeO_2-catalyzed reaction was studied at various substrate concentrations. **Figure 39** shows the reaction rate of TMB oxidation at various TMB concentrations (0-1.5 mM) at 25 mg/L CeO_2 NPs and 5.0 mM H_2O_2. Measurements with higher TMB levels were not feasible due to the TMB's poor solubility in water and its subsequent precipitation during the measurement. The obtained rate data for bare CeO_2 NPs, SL-CeO_2, and SPCe were fitted with the Michaelis-Menten kinetic model. Interestingly, the obtained K_m for SL-CeO_2 (0.200 mM) is nearly two times lower than that for bare CeO_2 NPs (0.359 mM), indicating a stronger affinity between SL-CeO_2 and H_2O_2, compared to bare CeO_2 NPs. For SPCe, on the other hand, the K_m (0.467 mM) was slightly larger than that of bare CeO_2 NPs, indicating comparable affinities of both SPCe and bare CeO_2 NPs toward H_2O_2. Also, the v_{max} values for SL-CeO_2 and SPCe were 0.01056 μM/s and 0.01823 μM/s, respectively. For bare CeO_2 NPs, v_{max} was found to be 0.01058 μM/s. When TMB is the substrate, the native HRP was reported to have a v_{max} of 0.1 μM/s and a K_m of 0.434 mM, which indicates that both bare CeO_2 NPs and SL-CeO_2 have lower K_m than native HRP enzyme, while SPCe has comparable K_m values, indicating excellent affinity of between the composites and the substrate.[208]

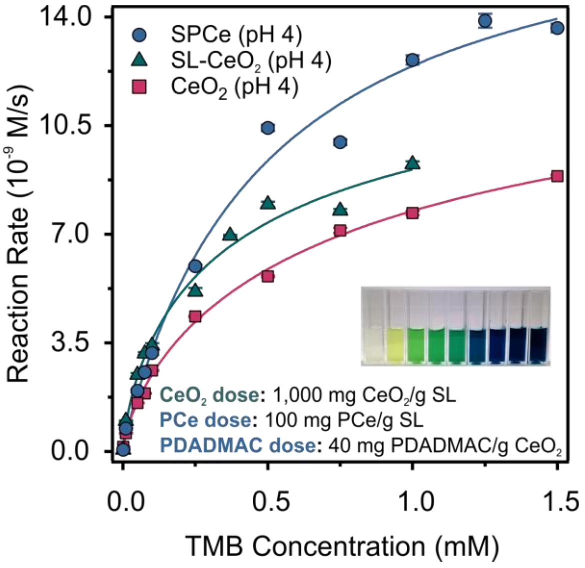

Figure 39. The TMB-oxidation reaction rate at different TMB concentrations catalyzed by CeO_2 NPs, SPCe, or SL-CeO_2 at pH 4.0. The lines represent the Michaelis-Menten fits, expressed by equation (2). The graphical inset shows that the intensity of the blue color (oxidized TMB) gradually increases with the amount of TMB.

For SPCe and SL-CeO_2, the lower surface coverage in the former led to easier access to the catalytic surface and higher v_{max}, which is attributed to the presence of PDADMAC. Unlike PB NPs, the immobilization of CeO_2 NPs enhanced or at least maintained its activity, in terms of K_m and v_{max} values. A possible explanation of such disparity in the change of activity upon immobilization of PB NPs and CeO_2 NPs is the better colloidal stability of the PB NPs at the pH of the respective assay. When stable particles (e.g., PB NPs) are immobilized, less catalytic surface is exposed, resulting in a deteriorated activity. On the other hand, with mildly aggregating particles (e.g., CeO_2 NPs), the loss of catalytic surface due to aggregation of the bare particles is more significant than the loss of catalytic surface after immobilization, resulting in better or maintained activity in the composite form. The Michaelis-Menten parameters of PB- and CeO_2-based composites, as well as several nanozyme systems reported in the literature, are summarized in **Table 10**. Hence, the immobilization and functionalization of CeO_2 NPs and

PB NPs not only enhanced the colloidal stability but also resulted in similar or better HRP-like activity, compared to the native enzymes, which renders such composites excellent antioxidant materials for industrial use.

Table 10: The parameters of the Michaelis-Menten fits for the HRP-like activity for PB- and CeO_2-based composites.

Nanozyme	$C_{\text{PB or CeO2}}$ (mg/L)	K_m (mM)	v_{max} (10^{-6} M/s)	Reference
PB-25 °C	10.0	2.19	6.71	Present work
AL-PB-25 °C	10.0	2.92	4.09	Present work
CeO_2-25 °C	25.0	0.359 ± 0.044	0.01058 ± 0.46	Present work
SL-CeO_2-25 °C	25.0	0.200 ± 0.034	0.01056 ± 0.61	Present work
SPCe-25 °C	25.0	0.467 ± 0.077	0.01823 ± 1.11	Present work
MoS_x-$Co(OH)_2$	-	0.236	0.0569	209
ZnS-MMT	-	0.055	0.0799	210
DNA-CoAl-LDH	-	1.775	0.0409	211
CoNiS-3/MMT	-	0.821	0.6831	212
BNNS@CuS	-	0.175	0.0376	213
VO_2 (fibers)	-	0.518	93	214
VO_2 (sheets)	-	0.111	168	214
VO_2 (rods)	-	0.801	399	214
CeO_2 (rods)	-	0.0753	0.0401	215
γ-Fe_2O_3-PB	-	0.307	1.06	174
Fe_3O_4	-	0.434	0.10	214
HRP (Guaiacol)	-	3.23	2.80	206
HRP (TMB)	-	0.434 ± 0.010	0.100 ± 8.83	208

5.5.3 The CAT-like activity of MnO_2-based composites

Bare MnO_2 MFs and SPMn composite exhibited CAT-like activity that was assessed via the CAT assay, in which the decrease in the absorption of H_2O_2 over time is monitored at 240 nm during the MnO_2-catalyzed breakdown of H_2O_2. The concentration of MnO_2 MFs (or its equivalent content in SPMn) was fixed at 10 mg/L during the activity assessment. In addition, the CAT activity of both MnO_2 MFs and SPMn was probed at 25 °C, and after the corresponding stock dispersions were thermally incubated at 50 °C and 75 °C for 90 min. **Figure 40** shows the reaction rate at various H_2O_2 concentrations (0-1.0 mg/L). The rate data evidently well-fit with the Michaelis–Menten model and the obtained K_m and v_{max} of MnO_2 MFs and SPMn composite at various temperatures are listed in **Table 11**.

At 25 °C, the K_m and v_{max} for bare MnO_2 MFs were found to be 0.083 mM and 30.79 μM/s, respectively, whereas for SPMn, the obtained K_m and v_{max} were to be 0.099 mM and 33.23 μM/s, respectively. The similarity in values indicates that the immobilization and functionalization of MnO_2 MFs did not affect its CAT-like activity, i.e., a similar magnitude of the catalytic surface is exposed in both cases.

Like the trend in SOD activity, the similarity in the activity of bare and immobilized MnO_2 MFs indicates that comparable loss of catalytic surface occurs 1) when bare MnO_2 MFs aggregates in aqueous media during the measurement time frame and 2) upon SPMn formulation, resulting in comparable CAT-lie activity. In addition, the thermal treatment of the bare or immobilized MnO_2 MFs exhibited minimal to no effect on the affinity of MnO_2 MFs towards the substrate as similar K_m values were obtained for both bare and immobilized MnO_2 MFs at 50 °C and 75 °C, compared to the corresponding values at 25 °C, as shown in **Table 11**. However, thermal treatment resulted in the decrease of v_{max} of both MnO_2 MFs and SPMn, compared to the untreated counterparts. The decrease was more pronounced with bare MnO_2 MFs than SPMn. Also, the magnitude of the decrease was independent of the temperature for either material, as shown in **Table 11**. Comparatively, the native CAT permanently loses its activity at 70 °C after only 30 min of thermal treatment,[216] which renders SPMn an excellent antioxidant with excellent structural stability and enzyme-like catalytic potential.

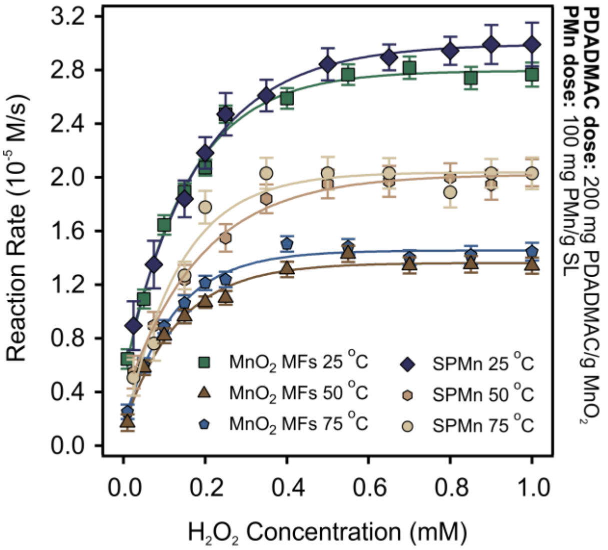

Figure 40. The CAT-like activity of bare MnO_2 MFs and SPMn at 25 °C, 50 °C, and 75 °C. The MnO_2 MFs concentration or its content in SPMn was kept at 10.0 mg/L. The solid lines represent the Michaelis–Menten fits, obtained from equation (2).

The CAT-like activity of MnO_2 is well-reported in the literature.[205, 217] Also, such CAT-like activity is observed for other nanostructured materials.[218] For example, Mu et al. examined the CAT activity of various Co_3O_4 nanostructures, the obtained K_m values (**Table 11**) indicate a significant dependence on the geometry.[62] For example, K_m for Co_3O_4 nanorods and nanocubes were 4.82 mM and 63.9 mM, respectively. In addition, Wu et al. probed the activity of native CAT and obtained relatively high v_{max} values of 224.3 and 222.6 µM/s for free and immobilized CAT, respectively. However, the reported K_m values were 25.7 mM and 27.4 mM for free and immobilized CAT, respectively.[219] Comparison of such values with those of the

MnO_2-based composites indicates that the obtained SPMn exhibits excellent affinity toward the substrates, and thus, are expected to serve as an excellent antioxidant with significant CAT-like activity that is maintained at high-temperature conditions, where native CAT is inactive.

Table 11: The Michaelis-Menten kinetic parameters of CAT-like activity determined for the MnO_2 MFs and SPMn composite at room and elevated temperatures.

Nanozyme	**C_{MnO2} (mg/L)**	**K_m (mM)**	**v_{max} (10^{-6} M/s)**	**Reference**
MnO_2-25 °C	10.0	0.083 ± 0.011	30.79 ± 1.01	Present work
MnO_2-50 °C	10.0	0.082 ± 0.008	15.17 ± 0.36	Present work
SPMn-25 °C	10.0	0.099 ± 0.010	16.09 ± 0.49	Present work
SPMn-25 °C	10.0	0.099 ± 0.010	33.23 ± 0.79	Present work
SPMn-50 °C	10.0	0.118 ± 0.017	23.14 ± 0.85	Present work
SPMn-75 °C	10.0	0.106 ± 0.025	23.77 ± 1.39	Present work
Free CAT	2.0	25.7	224.3	[219]
Immobilized CAT	2.0	27.4	222.6	[219]
Co_3O_4 (plates)	20	24.7	2.36	[62]
Co_3O_4 (rods)	20	4.82	1.89	[62]
Co_3O_4 (cubes)	20	63.9	1.23	[62]

5.5.4 *The antioxidant potential of CeO_2-based composites*

The radical-scavenging potential of the CeO_2-based composites was evaluated via the DPPH assay, in which the purple DPPH radical is reduced to a yellow product. The reduction is probed by monitoring the decrease in absorbance of the purple DPPH radical at 517 nm. The DPPH% (the percentage of unreacted DPPH, obtained using equation (40)) is recorded at various CeO_2 concentrations and constant DPPH concentration (15.0 mg/L). **Figure 41** shows the DPPH% as a function of CeO_2 NPs concentration or its content in either SPCe or SL-CeO_2. The DPPH% was found to decrease with increasing CeO_2 NPs concentration, indicating fewer radicals remain when more nanozymes are present. The SPCe exhibited the highest antioxidant activity, as indicated by the steeper decrease in the curve and the smallest EC_{50} value (46.9 mg/L). On the other hand, SL-CeO_2 possessed the most deteriorated DPPH reduction potential, the EC_{50} value was found to be 73.1 mg/L. Bare CeO_2 NPs exhibited intermediate DPPH reduction potential with an EC_{50} value of 60.3 mg/L.

A plausible interpretation of these trends can be obtained by factoring in both the extent of surface coverage and the magnitude of the loss of the catalytic surface upon immobilization. Like AL-PB, the immobilization of CeO_2 NPs into a fully covered composite (SL-CeO_2) hindered the access to the catalytic surface and lowered DPPH reduction potential. However, in the case of SPCe, the presence of PDADMAC resulted in partial coverage and enhanced access to the catalytic surface of immobilized CeO_2 NPs, resulting in better DPPH activity.

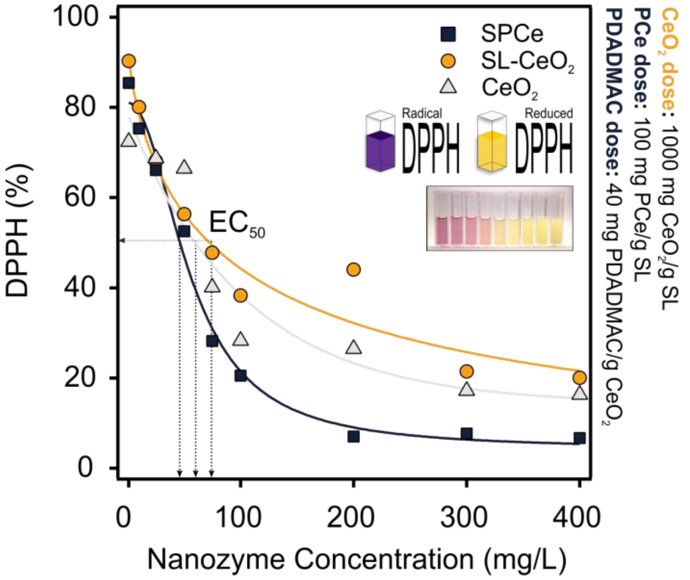

Figure 41. The DPPH radical scavenging potential of CeO_2 NPs, SL-CeO_2, and SPCe. The concentration of DPPH radical in the final samples was fixed at 15.0 mg/L. The DPPH% was calculated according to equation (40), and the data was fitted with the Hill equation to obtain the EC_{50} values. The inset image shows that the intensity of the yellow color of reduced DPPH increases with the increased nanozyme concentration.

The DPPH reduction potential is frequently reported for materials as an indication of their antioxidant potential.[67, 220] Olivera et al. probed the antioxidant potential of composites based on MgAl-LDH and bilva oil meal (BP) proteins. The EC_{50} values for bare LDH and LDH-BP composite were estimated to be 151.15 mg/L and 42.04 mg/L, respectively.[221] Also, Mao et al. probed the antioxidant potential of PtPdCu NPs, which caused a 50% reduction of DPPH radicals after 10 min when the trimetallic nanostructure concentration was 42.6 mg/L.[222] The comparison of these EC_{50} values with those of SPCe and SL-CeO_2 indicates that the formulated composites are excellent functional ROS scavengers, even in non-aqueous media.

Also, for the HRP-like activity of PB- and CeO_2-based composites, as well as the CAT-like activity of MnO_2-based composites, the obtained activities outperformed or are at least comparable to the native enzymes, as evidenced by the v_{max} and K_m values. On the other hand, for the SOD-like activity of PB- and MnO_2-based composites, the reported activities were lower than those of the corresponding native enzymes. Nevertheless, the loss of activity is often outweighed by the functional, structural, and thermal stability of such composites. For instance, the high functional, colloidal, and thermal stability of SPMn at harsh conditions (e.g., temperature), where native SOD undergoes a permanent loss of activity. Thus, the attained stability, low cost, ease of preparation, and preservation of enzyme activity of immobilized nanozymes often outweigh the partially reduced enzymatic activity, if any, given their economical edge and huge potential industrial applicability.

6 Conclusions

A colloid approach was presented for the development of antioxidant composites (AL-PB, SPMn, SL-CeO_2, and SPCe) based on inorganic nanozymes and functionalized polystyrene latex particles via controlled heteroaggregation of the oppositely charged particles.

Initial and thorough characterization of the colloidal state of the individual particles (PB, MnO_2, CeO_2, SL, AL) proved to be crucial for determining the optimal experimental conditions (pH, ionic strength, latex concentration). The optimal pH enabled the formation of highly charged particles, and hence, prevented homoaggregation. Also, for each composite, the optimal pH resulted in oppositely charged particles and strong electrostatic attraction. In addition, the assessment of the aggregation status and zeta potential of the individual particles at various ionic strengths enabled the determination of safe ionic strength conditions, at which the dispersions remain fairly stable to enable effective composite formulation.

The functionalization of negatively charged metal oxides (MnO_2 and CeO_2) with PDADMAC served to induce charge reversal and enable heteroaggregation with negatively charged SL particles via electrostatic forces. The adsorption occurred under the influence of DLVO-type forces (electrostatic and van der Waals forces). In addition, the variation in the amount of adsorbed PDADMAC highly affected the stability of the system and led to charge neutralization and reversal. For the PMn system, the parch-charge interactions are a possible contributor to the total interactions, as evidenced by the lower stability ratios at low PDADMAC doses, compared to high doses.

The formulation of antioxidant composites (AL-PB, SPMn, SL-CeO_2, and SPCe) occurred under the influence of electrostatic and vdW forces between the charged moieties on the comprising particles. The variation in the amount of immobilized nanozyme significantly altered the major force responsible for the colloidal stability of the resultant latex-nanozyme systems. The electrostatic attractive forces dominated the total interaction at low and high nanozyme doses due to the high overall charge on the particles. On the other hand, the occurrence of characteristic IEP (when the latex-nanozyme hybrid particles have no overall surface charge) indicates the significance of vdW forces. In addition, the presence of PDADMAC heavily altered the extent of surface coverage and indicates its high effectiveness in surface charge modification of both the nanozyme and latex. The PDADMAC-containing composites were found to be less decorated with nanozymes, compared to PDADMAC-free composites.

Also, the immobilization and PDADMAC functionalization of nanozymes did not compromise their antioxidant potential or enzyme-like activity. The interplay among factors such as the aggregation status of bare particles, their colloidal stability at the pH of the assay, and the extent of coverage in the final composites was found to highly affect the relative activity upon immobilization. Partially covered systems (SPCe and SPMn) exhibited better enzyme-like activity than the corresponding bare nanozymes, as well as similar fully covered composites (e.g., SL-CeO_2 and SPCe). Hence, the PDADMAC exerted a significant effect on the extent of surface coverage and the ease of access to the catalytic surface, and hence, affected the enzyme-like activity. Also, the higher the colloidal stability of the bare nanozyme, the more deteriorated its enzyme-like activity upon immobilization (e.g., AL-PB and SPMn), accounting for the relative change in the available catalytic surface prior to and after immobilization.

The composites exhibited a multi-enzymatic activity with CAT- and HRP-like activities, that are comparable to that of the native enzymes, as evidenced by the Michaelis-Menten parameters. In addition, the preservation of SOD- and CAT-like activities of SPMn after thermal treatment, where native enzymes lose activities, renders such material versatile antioxidants. These formulations also exhibit structural, colloidal, and functional stability, and are foreseen to have promising use in many industrial fields, where economically sustainable alternatives to enzymes are desired.

7 Summary

Oxidative stress presents a serious risk to biological systems and results in unwanted elevated levels of ROS. Naturally, ROS are produced by cytochrome P450 enzymes and peroxisomes, as well as during various metabolic processes such as ATP production and immune responses. In addition, certain exogenous sources such as pollution and unhealthy lifestyle can largely result in increased levels of ROS as well. The presence of ROS is inevitable as they are essential in various processes such as immune response, and the formation of cellular structures and signal molecules. However, the non-regulated presence of ROS can result in various serious and chronic health-related conditions such as cancer, cardiovascular diseases, diabetes, asthma, and neurodegenerative disorders such as Alzheimer's and Parkinson's diseases.

The biological systems naturally employ a number of defense mechanisms against oxidative stress including prevention, scavenging, and repair strategies using a vast array of antioxidants, which are highly effective substances that help regulate and eliminate excess ROS, and thus, are highly essential to the well-being of the living system. Antioxidant enzymes such as SOD and CAT are highly effective in scavenging $\bullet O_2^-$ and H_2O_2, respectively. These enzymes are also widely employed in various industries as well. However, natural enzymes are highly complex protein structures that suffer from high sensitivity to operational conditions such as pH and temperature. Hence, undesignated conditions can result in permanent loss of catalytic activity, which has rendered enzyme production and purification processes time-consuming and often considerably expensive. Nanozymes have emerged as promising artificial enzymes that circumvent the significant drawbacks of native enzymes. The preparation of nanozymes is often straightforward and economical to achieve; most importantly, nanozymes typically possess catalytic activity well outside the operational conditions of the mimicked enzyme due to large surface area, structural stability, and the tunability of their physicochemical properties. Nevertheless, since many inorganic nanoparticles are water-insoluble such as metal oxides, their colloidal stability largely depends on the experimental conditions such as temperature, pH, ionic strength, and the presence of stabilizing agents such as surfactants and polyelectrolytes. Moreover, the industrial or biological applications of these nanomaterials such as catalysis and environmental remediation may require pH or ionic strength conditions at which bare particles are heavily aggregating, and thus, versatile use of such materials requires not only a solid comprehension of their colloidal state but also the development of strategies and sustainable methods to prevent the aggregation of these nanozymes during their use.

The work pertaining to the current dissertation deals with antioxidant nanozymes (PB NPs, MnO_2 MFs, and CeO_2 NPs) and presents a systematic colloid approach to immobilize these nanozymes onto highly stable latex particles (AL and SL) via controlled and systematic heteroaggregation. The latex particles serve as excellent support material and are expected to result in structurally stable composites (AL-PB, SPMn, SL-CeO_2, SPCe) with enzyme-like catalytic potential. The composites are also foreseen to have excellent structural, functional, and colloidal stability, as well as promising enzyme-like catalytic potential that is comparable to that of the native enzymes. In the first part of the dissertation, PB NPs, MnO_2 MFs, and CeO_2 NPs were synthesized according to reported procedures and later characterized via XPS and XRD, as well as UV-vis and Raman spectroscopy. The as-prepared particles were also visualized via AFM, TEM, and SEM techniques.

In the second part of the dissertation, the colloidal state of the individual nanozymes and latex particles was thoroughly examined. First, the pH-dependent surface charging and particle size were probed in the pH range of 3-11 to determine the optimal pH for composite formation. For the individual particles comprising each composite, the optimal pH shall give rise to highly and oppositely charged particles with large size differential. For instance, for the formation of AL-PB, the optimal pH (pH~4.0) resulted in highly negative PB NPs and highly positive AL, with PB NPs significantly smaller than AL. Next, the resistance against salt-induced aggregation of the nanozymes and the latex particles was examined at the optimal pH by measuring the stability ratio and zeta potential at various salt levels. The results revealed that at 1.0 mM salt level, the particles maintain high zeta potential and do not aggregate heavily, and thus, the ionic level was fixed at 1.0 mM during composite formulation. Third, the optimal latex concentration to be used during composite formation was determined by comparing the increase in the particle size during diffusion-controlled aggregation at different particle concentrations, 1.0 M ionic strength, and the optimal pH. At such a high salt concentration, the surface charge on the particles is effectively non-existent due to charge screening resulting in diffusion-controlled aggregation under the influence of vdW forces. Optimal latex concentrations are those corresponding to early-stage aggregation. The results of these three measurements provide the optimal pH, ionic strength, and latex particle concentration for the composite formulation. In addition, the pH-dependent surface charging of MnO_2 MFs and CeO_2 NPs revealed an optimal pH of 9.0, where they have a large size differential; however, unlike PB NPs and CeO_2 NPs at pH 4.0, both oxides have similar surface charge as their respective latex, SL, which required their surface modification to induce opposite surface charge.

In the third part, MnO_2 MFs and CeO_2 NPs were surface-modified via the adsorption of the positively charged PDADMAC polyelectrolyte to induce enough positive surface charge that will allow heteroaggregation with SL via electrostatic attraction. Thus, at fixed metal oxide concentration, 1.0 mM ionic strength, and pH 9.0, the stability ratio and zeta potential at various PDADMAC doses (in mg PDADMAC/g metal oxide) were measured. The PDADMAC adsorption was enabled by electrostatic and vdW interactions, and in both cases, the system exhibited a charge neutralization-charge reversal trend. The high stability ratio and zeta potential of the PDADMAC-functionalized particles (PMn and PCe) is attributed to the electrostatic repulsion among the individual functionalized particles. The IEP of the system, on the other hand, corresponds to balanced positive (PDADMAC) and negative (metal oxide) charges resulting in functionalized particles with no overall charge, which leads to heavy aggregation and subsequent system destabilization. These measurements allowed the selection of the proper PDADMAC dose, at which the functionalized metal oxide particles are sufficiently charged for subsequent heteroaggregation with SL via electrostatic attractive forces.

In the fourth part, the formation of AL-PB and SL-CeO_2 at 4.0, as well as for SL-PMn (SPMn) and SL-PCe (SPCe) at pH 9.0 was achieved via heteroaggregation via electrostatic and vdW attraction forces. In all cases, the ionic strength was fixed at 1.0 mM and the latex concentration was fixed at the optimal concentration, determined from diffusion-controlled aggregation measurements (25.0 mg/L AL and 125.0 mg/L SL). Also, the optimal PDADMAC doses, assessed during absorption measurements, were determined to be 200 mg PDADMAC/g MnO_2 and 40.0 mg PDADMAC/g CeO_2. The formation of AL-PB, SPMn, SL-CeO_2, and SPCe composites was monitored by measuring aggregation rate and zeta potential at various PB NPs, PMn, CeO_2 NPs, and PCe doses, respectively. Similar to PDADMAC adsorption, the four latex-nanozyme systems exhibited charge neutralization-charge reversal trends. Low nanozyme doses (in mg nanozyme/g latex) resulted in minimally covered latex particles; therefore, the composites maintained their original charge resulting in high colloidal stability due to electrostatic repulsion, as evidenced by the high stability ratio and zeta potential. The IEP of latex-nanozyme systems was observed at doses resulting in balanced negative and positive charges, where the neutral hybrid particles underwent diffusion-controlled aggregation under the influence of vdW forces. Nanozyme doses higher than those around the corresponding IEP led to a reversal of the surface charge, and the generated opposite charge that gave rise to stable composites as a result of electrostatic repulsion among the individual hybrid particles.

In the fifth part, the standardized assays were followed to probe the enzyme-like catalytic potential. In general, neither the immobilization nor PDADMAC functionalization of nanozymes compromised their enzyme-like activity. Nevertheless, the change in the activity upon immobilization was different for the different nanozymes. The PB-based composites exhibited SOD- and HRP-like activities, assessed via Fridovich and Guaiacol assay, respectively. Compared to bare PB NPs, the activity of immobilized PB NPs (AL-PB) slightly deteriorated. On the other hand, the MnO_2-based composites exhibited SOD- and CAT-like activities that were assessed at 25 °C, 50 °C, and 75 °C. The CAT-like activity was assessed by monitoring the decomposition of H_2O_2 via spectrophotometry. At 25 °C, the SPMn showed similar SOD- and CAT-like activity as the bare MnO_2 MFs. At 50 °C and 75 °C, the SOD like-activity was still unaffected by the thermal treatment. However, after thermal treatment, both bare and immobilized MnO_2 MFs exhibited a reduction in the CAT-like activity, as observed by the slight reduction in the v_{max} values, obtained from the Michaelis-Menten model. Also, the CeO_2-based composites (SL-CeO_2 and SPCe) showed HRP-like activity and DPPH radical scavenging potential, assessed via the TMB and DPPH assays, respectively. The SL-CeO_2 and SPCe showed comparable HPR-like activity, compared to bare CeO_2 NPs. As for the DPPH radical scavenging, the SPCe showed better activity while SL-CeO_2 exhibited comparable reduction potential.

For a given nanozyme, the enzyme-like activity of the corresponding composite depends on several factors such as the colloidal stability of the bare nanozymes and the extent of coverage in the composites. The PB NPs form stable dispersions, and thus, the immobilization results in the decreased availability of the catalytic surface. Besides, the fully covered status of AL-PB further hiders the access to the catalytic surface, resulting in a deteriorated activity. On the other hand, bare MnO_2 MFs forms heavily aggregating dispersions, and hence, the immobilization results in no overall change in the available catalytic surface, as a result of partial coverage due to PDADMAC presence. Similarly, for CeO_2-based composites, the less decorated status of SPCe allows more efficient access to the surface of immobilized CeO_2 NPs, and thus, SPCe is expected to exhibit better enzyme-like potential than the fully covered SL-CeO_2 composite. The observed HRP- and CAT-like activity of the composites was better than the corresponding native enzymes, as evident by the parameters of the Michaelis-Menten model. Thus, the composites exhibited multi-enzymatic activity with structural, colloidal, thermal, and functional stability, which renders them versatile nanozymes in industrial applications, where economically sustainable antioxidants are desired.

8 Acknowledgment

First and foremost, I would like to express my deepest appreciation and utmost gratitude to my Ph.D. supervisor, Dr. Szilágyi István, for the unfailing support and constant guidance that carried me through my Ph.D. studies, this work could not have been concluded without him.

I am extremely grateful to Dr. Szabó Tamás for his continuing and nurturing advising throughout my graduate studies.

I am also thankful to the head of the Department of Physical Chemistry & Materials Science, Prof. Tóth Ágota, for her constant help and advice throughout my Ph.D. studies.

I am also grateful to Dr. Samu Gergely for his assistance in the XPS and XRD measurements.

Many thanks to the department secretaires, Ildikó Patakiné Sziveri and Karolina Baráthné Takács, for the long hours of administrative minutiae on our behalf.

I would also like to express gratitude to the treasured colleagues at the Biocolloids Research Group (Adél, Bojana, Dóri, Kata, Szabi, Szilard, Zoli, and Zsófi) for the fruitful and friendly working environment, as well as the great memories that will always be cherished.

I also express appreciation to my dearest friends (Elham, Alexandra G., Bence, Anni, Janice, Paras, Maitrayee, Tamás G., Vaishali, and Jelena S.) for the wonderful memories and treasured experiences.

Last, but by no means least, I am extremely grateful to my parents and siblings for their immeasurable love and endless support that carried me through my Ph.D. years.

9 References

1. Bouayed, J.; Bohn, T., Exogenous antioxidants-Double-edged swords in cellular redox state. *Oxidative Med. Cell. Longev.* **2010,** *3* (4), 228-237.
2. Birben, E.; Sahiner, U. M.; Sackesen, C.; Erzurum, S.; Kalayci, O., Oxidative stress and antioxidant defense. *WAO J.* **2012,** *5* (1), 9-19.
3. Martinelli, C.; Pucci, C.; Battaglini, M.; Marino, A.; Ciofani, G., Antioxidants and nanotechnology: Promises and limits of potentially disruptive approaches in the treatment of central nervous system diseases. *Adv. Healthc. Mater.* **2020,** *9* (3), 1901589.
4. Ighodaro, O. M.; Akinloye, O. A., First line defence antioxidants-superoxide dismutase (SOD), catalase (CAT) and glutathione peroxidase (GPX): Their fundamental role in the entire antioxidant defence grid. *Alex. J. Med.* **2018,** *54* (4), 287-293.
5. Winterbourn, C. C., Reconciling the chemistry and biology of reactive oxygen species. *Nat. Chem. Biol.* **2008,** *4* (5), 278-286.
6. Dixon, S. J.; Stockwell, B. R., The role of iron and reactive oxygen species in cell death. *Nat. Chem. Biol.* **2014,** *10* (1), 9-17.
7. Tanner, P.; Balasubramanian, V.; Palivan, C. G., Aiding nature's organelles: Artificial peroxisomes play their role. *Nano Lett.* **2013,** *13* (6), 2875-2883.
8. Ranjekar, P. K.; Hinge, A.; Hegde, M. V.; Ghate, M.; Kale, A.; Sitasawad, S.; Wagh, U. V.; Debsikdar, V. B.; Mahadik, S. P., Decreased antioxidant enzymes and membrane essential polyunsaturated fatty acids in schizophrenic and bipolar mood disorder patients. *Psychiatry Res.* **2003,** *121* (2), 109-122.
9. Valko, M.; Rhodes, C. J.; Moncol, J.; Izakovic, M.; Mazur, M., Free radicals, metals and antioxidants in oxidative stress-induced cancer. *Chem.-Biol. Interact.* **2006,** *160* (1), 1-40.
10. Lourenco, S. C.; Moldao-Martins, M.; Alves, V. D., Antioxidants of natural plant origins: From sources to food industry applications. *Molecules* **2019,** *24* (22), 4132.
11. Brieger, K.; Schiavone, S.; Miller, F. J.; Krause, K. H., Reactive oxygen species: from health to disease. *Swiss Med. Wkly.* **2012,** *142*, 13659.
12. Pisoschi, A. M.; Pop, A., The role of antioxidants in the chemistry of oxidative stress: A review. *Eur. J. Med. Chem.* **2015,** *97*, 55-74.
13. Sies, H.; Jones, D. P., Reactive oxygen species (ROS) as pleiotropic physiological signalling agents. *Nat. Rev. Mol. Cell Biol.* **2020,** *21* (7), 363-383.
14. Forman, H. J.; Zhang, H. Q., Targeting oxidative stress in disease: promise and limitations of antioxidant therapy. *Nat. Rev. Drug Discov.* **2021,** *20* (9), 689-709.
15. Ames, B. N.; Shigenaga, M. K.; Hagen, T. M., Oxidants, antioxidants, and the degenerative diseases of aging. *Proc. Natl. Acad. Sci. U. S. A.* **1993,** *90* (17), 7915-7922.
16. Zhang, L. B.; Laug, L.; Munchgesang, W.; Pippel, E.; Gosele, U.; Brandsch, M.; Knez, M., Reducing stress on cells with apoferritin-encapsulated platinum nanoparticles. *Nano Lett.* **2010,** *10* (1), 219-223.
17. Reuter, S.; Gupta, S. C.; Chaturvedi, M. M.; Aggarwal, B. B., Oxidative stress, inflammation, and cancer How are they linked? *Free Radic. Biol. Med.* **2010,** *49* (11), 1603-1616.
18. Erejuwa, O. O.; Sulaiman, S. A.; Ab Wahab, M. S., Honey: A novel antioxidant. *Molecules* **2012,** *17* (4), 4400-4423.
19. Gennaris, A.; Ezraty, B.; Henry, C.; Agrebi, R.; Vergnes, A.; Oheix, E.; Bos, J.; Leverrier, P.; Espinosa, L.; Szewczyk, J.; Vertommen, D.; Iranzo, O.; Collet, J. F.; Barras, F., Repairing oxidized proteins in the bacterial envelope using respiratory chain electrons. *Nature* **2015,** *528* (7582), 409-+.
20. Sies, H., Oxidative stress: Oxidants and antioxidants. *Exp. Physiol.* **1997,** *82* (2), 291-

295.

21. Baschieri, A.; Amorati, R., Methods to determine chain-breaking antioxidant activity of nanomaterials beyond DPPH center dot. A review. *Antioxidants* **2021,** *10* (10), 1551.
22. Nirmala, C.; Bisht, M. S.; Bajwa, H. K.; Santosh, O., Bamboo: A rich source of natural antioxidants and its applications in the food and pharmaceutical industry. *Trends Food Sci. Technol.* **2018,** *77*, 91-99.
23. Moura, F. A.; de Andrade, K. Q.; dos Santos, J. C. F.; Araujo, O. R. P.; Goulart, M. O. F., Antioxidant therapy for treatment of inflammatory bowel disease: Does it work? *Redox Biol.* **2015,** *6*, 617-639.
24. Othman, A.; Norton, L.; Finny, A. S.; Andreescu, S., Easy-to-use and inexpensive sensors for assessing the quality and traceability of cosmetic antioxidants. *Talanta* **2020,** *208*, 120473.
25. Boo, Y. C., Can plant phenolic compounds protect the skin from airborne particulate matter? *Antioxidants* **2019,** *8* (9), 379.
26. Hoang, H. T.; Moon, J. Y.; Lee, Y. C., Natural antioxidants from plant extracts in skincare cosmetics: Recent applications, challenges and perspectives. *Cosmetics* **2021,** *8* (4), 106.
27. Silva, S.; Ferreira, M.; Oliveira, A. S.; Magalhaes, C.; Sousa, M. E.; Pinto, M.; Lobo, J. M. S.; Almeida, I. F., Evolution of the use of antioxidants in anti-ageing cosmetics. *Int. J. Cosmetic Sci.* **2019,** *41* (4), 378-386.
28. Garrido-Miranda, K. A.; Rivas, B. L.; Perez-Rivera, M. A.; Sanfuentes, E. A.; Pena-Farfal, C., Antioxidant and antifungal effects of eugenol incorporated in bionanocomposites of poly(3-hydroxybutyrate)-thermoplastic starch. *LWT-Food Sci. Technol.* **2018,** *98*, 260-267.
29. Badhani, B.; Sharma, N.; Kakkar, R., Gallic acid: a versatile antioxidant with promising therapeutic and industrial applications. *RSC Adv.* **2015,** *5* (35), 27540-27557.
30. Franco, R.; Navarro, G.; Martinez-Pinilla, E., Antioxidants versus food antioxidant additives and food preservatives. *Antioxidants* **2019,** *8* (11), 542.
31. Duy, M.; Matrat, M.; Ben Amara, A.; Foucher, F.; Moreau, B.; Yu, Y.; Goussougli, M.; Fournet, R.; Sirjean, B.; Glaude, P. A., Antioxidant effect of 2-4 xylenol on fuel oxidation in liquid and gas phase over a wide temperature range. *Fuel Process. Technol.* **2022,** *236*, 107414.
32. Kirschweng, B.; Tatraaljai, D.; Foldes, E.; Pukanszky, B., Natural antioxidants as stabilizers for polymers. *Polym. Degrad. Stabil.* **2017,** *145*, 25-40.
33. Kirk, O.; Borchert, T. V.; Fuglsang, C. C., Industrial enzyme applications. *Curr. Opin. Biotechnol.* **2002,** *13* (4), 345-351.
34. Raveendran, S.; Parameswaran, B.; Ummalyma, S. B.; Abraham, A.; Mathew, A. K.; Madhavan, A.; Rebello, S.; Pandey, A., Applications of microbial enzymes in food industry. *Food Technol. Biotechnol.* **2018,** *56* (1), 16-30.
35. Bafana, A.; Dutt, S.; Kumar, S.; Ahuja, P. S., Superoxide dismutase: an industrial perspective. *Crit. Rev. Biotechnol.* **2011,** *31* (1), 65-76.
36. Xu, L. H.; Ji, X. H.; Zhao, N.; Song, C. X.; Wang, F. S.; Liu, C. H., The conjugation of Cu/Zn superoxide dismutase (SOD) to O-(2-hydroxyl) propyl-3-trimethyl ammonium chitosan chloride (O-HTCC) enhances its therapeutic potential against radiation-induced oxidative damage. *Polym. Chem.* **2016,** *7* (9), 1826-1835.
37. Mira, E.; Carmona-Rodriguez, L.; Perez-Villamil, B.; Casas, J.; Fernandez-Acenero, M. J.; Martinez-Rey, D.; Martin-Gonzalez, P.; Heras-Murillo, I.; Paz-Cabezas, M.; Tardaguilal, M.; Oury, T. D.; Martin-Puig, S.; Lacalle, R. A.; Fabrias, G.; Diaz-Rubio, E.; Manes, S., SOD3 improves the tumor response to chemotherapy by stabilizing endothelial HIF-2 alpha. *Nat. Commun.* **2018,** *9*, 575.

38. Copeland, R. A., *Enzymes - A practical introduction to structure, mechanism, and data analysis*. Wiley-VCH Inc: New York, 2000.
39. Bugg, T., *Introduction to enzyme and coenzyme chemistry*. Blackwell Publishing Ltd: Oxford, 2004.
40. Kuah, E.; Toh, S.; Yee, J.; Ma, Q.; Gao, Z. Q., Enzyme mimics: Advances and applications. *Chem.-Eur. J.* **2016,** *22* (25), 8404-8430.
41. Robinson, P. K., Enzymes: principles and biotechnological applications. In *Understanding biochemistry: Enzymes and membranes*, 2015; Vol. 59, pp 1-41.
42. Johnson, K. A.; Goody, R. S., The original Michaelis constant: Translation of the 1913 Michaelis-Menten paper. *Biochemistry* **2011,** *50* (39), 8264-8269.
43. Lin, Y. H.; Ren, J. S.; Qu, X. G., Catalytically active nanomaterials: A promising candidate for artificial enzymes. *Accounts Chem. Res.* **2014,** *47* (4), 1097-1105.
44. Zhang, R. F.; Yan, X. Y.; Fan, K. L., Nanozymes inspired by natural enzymes. *Accounts Mater. Res.* **2021,** *2* (7), 534-547.
45. Danial, E. N.; Alkhalaf, M. I., Co-immobilisation of superoxide dismutase and catalase using an in vitro encapsulation protocol. *J. King Saud Univ. Sci.* **2020,** *32* (4), 2489-2494.
46. Pavlovic, M.; Nafradi, M.; Rouster, P.; Murath, S.; Szilagyi, I., Highly stable enzyme-mimicking nanocomposite of antioxidant activity. *J. Colloid Interface Sci.* **2019,** *543*, 174-182.
47. Yang, Y. F.; Shen, D. J.; Long, Y. J.; Xie, Z. X.; Zheng, H. Z., Intrinsic peroxidase-like activity of ficin. *Sci Rep* **2017,** *7*, 8.
48. Daniel, R. M.; Dines, M.; Petach, H. H., The denaturation and degradation of stable enzymes at high temperatures. *Biochem. J.* **1996,** *317*, 1-11.
49. Carrea, G.; Riva, S., Properties and synthetic applications of enzymes in organic solvents. *Angew. Chem.-Int. Edit.* **2000,** *39* (13), 2226-2254.
50. Wei, H.; Wang, E. K., Nanomaterials with enzyme-like characteristics (nanozymes): next-generation artificial enzymes. *Chem. Soc. Rev.* **2013,** *42* (14), 6060-6093.
51. Tokuyama, H.; Yamago, S.; Nakamura, E.; Shiraki, T.; Sugiura, Y., Photoinduced biochemical-activity of fullerene carboxylic-acid. *J. Am. Chem. Soc.* **1993,** *115* (17), 7918-7919.
52. Dugan, L. L.; Gabrielsen, J. K.; Yu, S. P.; Lin, T. S.; Choi, D. W., Buckminsterfullerenol free radical scavengers reduce excitotoxic and apoptotic death of cultured cortical neurons. *Neurobiol. Dis.* **1996,** *3* (2), 129-135.
53. Kirkorian, K.; Ellis, A.; Twyman, L. J., Catalytic hyperbranched polymers as enzyme mimics; exploiting the principles of encapsulation and supramolecular chemistry. *Chem. Soc. Rev.* **2012,** *41* (18), 6138-6159.
54. Labadi, I.; Szilagyi, I.; Jakab, N. I.; Hernadi, K.; Palinko, I., Metal complexes immobilised in/on porous matrices - possible enzyme mimics. *Mater. Sci.* **2003,** *21* (2), 235-244.
55. Szilagyi, I.; Nagy, G.; Hernadi, K.; Labadi, I.; Palinko, I., Modeling copper-containing enzyme mimics. *J. Mol. Struct. THEOCHEM* **2003,** *666-667*.
56. Kofoed, J.; Reymond, J. L., Dendrimers as artificial enzymes. *Curr. Opin. Chem. Biol.* **2005,** *9* (6), 656-664.
57. Wu, J. J. X.; Wang, X. Y.; Wang, Q.; Lou, Z. P.; Li, S. R.; Zhu, Y. Y.; Qin, L.; Wei, H., Nanomaterials with enzyme-like characteristics (nanozymes): next-generation artificial enzymes (II). *Chem. Soc. Rev.* **2019,** *48* (4), 1004-1076.
58. Jiang, H.; Chen, Z. H.; Cao, H. Y.; Huang, Y. M., Peroxidase-like activity of chitosan stabilized silver nanoparticles for visual and colorimetric detection of glucose. *Analyst* **2012,** *137* (23), 5560-5564.
59. He, W. W.; Zhou, Y. T.; Warner, W. G.; Hu, X. N.; Wu, X. C.; Zheng, Z.; Boudreau,

M. D.; Yin, J. J., Intrinsic catalytic activity of Au nanoparticles with respect to hydrogen peroxide decomposition and superoxide scavenging. *Biomaterials* **2013,** *34* (3), 765-773.

60. Moglianetti, M.; De Luca, E.; Deborah, P. A.; Marotta, R.; Catelani, T.; Sartori, B.; Amenitsch, H.; Retta, S. F.; Pompa, P. P., Platinum nanozymes recover cellular ROS homeostasis in an oxidative stress-mediated disease model. *Nanoscale* **2016,** *8* (6), 3739-3752.
61. Rastogi, L.; Karunasagar, D.; Sashidhar, R. B.; Giri, A., Peroxidase-like activity of gum kondagogu reduced/stabilized palladium nanoparticles and its analytical application for colorimetric detection of glucose in biological samples. *Sens. Actuator B-Chem.* **2017,** *240*, 1182-1188.
62. Mu, J. S.; Zhang, L.; Zhao, M.; Wang, Y., Catalase mimic property of Co_3O_4 nanomaterials with different morphology and its application as a calcium sensor. *ACS Appl. Mater. Interfaces* **2014,** *6* (10), 7090-7098.
63. Murugan, C.; Murugan, N.; Sundramoorthy, A. K.; Sundaramurthy, A., Nanoceria decorated flower-like molybdenum sulphide nanoflakes: an efficient nanozyme for tumour selective ROS generation and photo thermal therapy. *Chem. Commun.* **2019,** *55* (55), 8017-8020.
64. Chen, W.; Chen, J.; Liu, A. L.; Wang, L. M.; Li, G. W.; Lin, X. H., Peroxidase-like activity of cupric oxide nanoparticle. *ChemCatChem* **2011,** *3* (7), 1151-1154.
65. Ghosh, S.; Roy, P.; Karmodak, N.; Jemmis, E. D.; Mugesh, G., Nanoisozymes: Crystal-facet-dependent enzyme-mimetic activity of V_2O_5 nanomaterials. *Angew. Chem.-Int. Edit.* **2018,** *57* (17), 4510-4515.
66. Dai, Z. H.; Liu, S. H.; Bao, J. C.; Jui, H. X., Nanostructured FeS as a Mimic Peroxidase for Biocatalysis and Biosensing. *Chem.-Eur. J.* **2009,** *15* (17), 4321-4326.
67. Chen, T. M.; Zou, H.; Wu, X. J.; Liu, C. C.; Situ, B.; Zheng, L.; Yang, G. W., Nanozymatic antioxidant system based on MoS_2 nanosheets. *ACS Appl. Mater. Interfaces* **2018,** *10* (15), 12453-12462.
68. Lin, T. R.; Zhong, L. S.; Song, Z. P.; Guo, L. Q.; Wu, H. Y.; Guo, Q. Q.; Chen, Y.; Fu, F. F.; Chen, G. N., Visual detection of blood glucose based on peroxidase-like activity of WS_2 nanosheets. *Biosens. Bioelectron.* **2014,** *62*, 302-307.
69. Wang, L. F.; Li, Y.; Zhao, L.; Qi, Z. J.; Gou, J. Y.; Zhang, S.; Zhang, J. Z., Recent advances in ultrathin two-dimensional materials and biomedical applications for reactive oxygen species generation and scavenging. *Nanoscale* **2020,** *12* (38), 19516-19535.
70. Wu, S. W.; Qiu, M.; Guo, B. C.; Zhang, L. Q.; Lvov, Y., Nanodot-loaded clay nanotubes as green and sustained radical scavengers for elastomer. *ACS Sustain. Chem. Eng.* **2017,** *5* (2), 1775-1783.
71. Qu, K. G.; Shi, P.; Ren, J. S.; Qu, X. G., Nanocomposite incorporating V_2O_5 nanowires and gold nanoparticles for mimicking an enzyme cascade reaction and its application in the detection of biomolecules. *Chem.-Eur. J.* **2014,** *20* (24), 7501-7506.
72. Tsekhmistrenko, S. I.; Bityutskyy, V. S.; Tsekhmistrenko, O. S.; Polishchuk, V. M.; Polishchuk, S. A.; Ponomarenko, N. V.; Melnychenko, Y. O.; Spivak, M. Y., Enzyme-like activity of nanomaterials. *Regul. Mech. Biosyst.* **2018,** *9* (3), 469-476.
73. Liang, M. M.; Yan, X. Y., Nanozymes: From new concepts, mechanisms, and standards to applications. *Accounts Chem. Res.* **2019,** *52* (8), 2190-2200.
74. Huang, Y. Y.; Liu, C. Q.; Pu, F.; Liu, Z.; Ren, J. S.; Qu, X. G., A GO-Se nanocomposite as an antioxidant nanozyme for cytoprotection. *Chem. Commun.* **2017,** *53* (21), 3082-3085.
75. Li, M. H.; Zhang, H.; Hou, Y. H.; Wang, X.; Xue, C. C.; Li, W.; Cai, K. Y.; Zhao, Y. L.; Luo, Z., State-of-the-art iron-based nanozymes for biocatalytic tumor therapy. *Nanoscale Horiz.* **2020,** *5* (2), 202-217.

76. Zeng, L. L.; Han, Y. X.; Chen, Z. W.; Jiang, K.; Golberg, D.; Weng, Q. H., Biodegradable and peroxidase-mimetic boron oxynitride nanozyme for breast cancer therapy. *Adv. Sci.* **2021,** *8* (16), 2101184.
77. Hong, C. Y.; Meng, X. Q.; He, J. Y.; Fan, K. L.; Yan, X. Y., Nanozyme: A promising tool from clinical diagnosis and environmental monitoring to wastewater treatment. *Particuology* **2022,** *71*, 90-107.
78. Holmberg, K., *Handbook of Applied Surface and Colloid Chemistry, Vol. 1*. John Wiley: New York, 2002.
79. Holmberg, K., *Handbook of Applied Surface and Colloid Chemistry, Vol. 2*. John Wiley: New York, 2002.
80. Shrestha, S.; Wang, B.; Dutta, P., Nanoparticle processing: Understanding and controlling aggregation. *Adv. Colloid Interface Sci.* **2020,** *279*, 102162.
81. de Gennes, P. G., Ultradivided matter. *Nature* **2001,** *412* (6845), 385-385.
82. Weir, A.; Westerhoff, P.; Fabricius, L.; Hristovski, K.; von Goetz, N., Titanium dioxide nanoparticles in food and personal care products. *Environ. Sci. Technol.* **2012,** *46* (4), 2242-2250.
83. Farrokhpay, S., A review of polymeric dispersant stabilisation of titania pigment. *Adv. Colloid Interface Sci.* **2009,** *151* (1-2), 24-32.
84. Zheng, W.; Xue, F. M.; Zhang, M.; Wu, Q. Q.; Yang, Z.; Ma, S. X.; Liang, H. T.; Wang, C. L.; Wang, Y. X.; Ai, X. K.; Yang, Y.; Yu, K. X., Charged particle (negative ion)-based cloud seeding and rain enhancement trial design and implementation. *Water* **2020,** *12* (6).
85. Buffle, J.; Wilkinson, K. J.; Stoll, S.; Filella, M.; Zhang, J. W., A generalized description of aquatic colloidal interactions: The three-colloidal component approach. *Environ. Sci. Technol.* **1998,** *32* (19), 2887-2899.
86. Martinez-Pedrero, F.; Alousque, F.; de Gaudemaris, B.; Berriot, J.; Gaboriaud, F.; Bremond, N.; Bibette, J., Making an elastomeric composite material via the heteroaggregation of a binary colloidal dispersion. *Soft Matter* **2012,** *8* (33), 8752-8757.
87. Thomas, A. W.; Foster, S. B., The colloid content of vegetable tanning extracts. *J. Ind. Eng. Chem.* **1922,** *14* (3), 191-195.
88. Zhao, H. W.; Chen, X. J.; Wang, G. Z.; Qiu, Y. F.; Guo, L., Two-dimensional amorphous nanomaterials: synthesis and applications. *2D Mater.* **2019,** *6* (3), 032002.
89. Luo, J. Y.; Cote, L. J.; Tung, V. C.; Tan, A. T. L.; Goins, P. E.; Wu, J. S.; Huang, J. X., Graphene oxide nanocolloids. *J. Am. Chem. Soc.* **2010,** *132* (50), 17667-17669.
90. Gelesky, M. A.; Umpierre, A. P.; Machado, G.; Correia, R. R. B.; Magno, W. C.; Morais, J.; Ebeling, G.; Dupont, J., Laser-induced fragmentation of transition metal nanoparticles in ionic liquids. *J. Am. Chem. Soc.* **2005,** *127* (13), 4588-4589.
91. Rao, C. N. R.; Nath, M., Inorganic nanotubes. *Dalton Trans.* **2003,** (1), 1-24.
92. Klabunde, K. J., *Nanoscale materials in chemistry*. John Wiley: New York, 2001.
93. Lin, Y. H.; Ren, J. S.; Qu, X. G., Nano-gold as artificial enzymes: Hidden talents. *Adv. Mater.* **2014,** *26* (25), 4200-4217.
94. Ott, L. S.; Finke, R. G., Transition-metal nanocluster stabilization for catalysis: A critical review of ranking methods and putative stabilizers. *Coord. Chem. Rev.* **2007,** *251* (9-10), 1075-1100.
95. Yu, Y. L.; Zhang, P.; Guo, L. M.; Chen, Z. D.; Wu, Q.; Ding, Y. H.; Zheng, W. J.; Cao, Y., The design of TiO_2 nanostructures (nanoparticle, nanotube, and nanosheet) and their photocatalytic activity. *J. Phys. Chem. C* **2014,** *118* (24), 12727-12733.
96. Zumreoglu-Karan, B.; Ay, A. N., Layered double hydroxides - multifunctional nanomaterials. *Chem. Pap.* **2012,** *66* (1), 1-10.
97. Adam, V.; Loyaux-Lawniczak, S.; Quaranta, G., Characterization of engineered TiO_2

nanomaterials in a life cycle and risk assessments perspective. *Environ. Sci. Pollut. Res.* **2015,** *22* (15), 11175-11192.

98. Li, P.; Guo, W.; Lu, Z.; Tian, J.; Li, X.; Wang, H., UV-responsive single-microcapsule self-healing material with enhanced UV-shielding SiO_2/ZnO hybrid shell for potential application in space coatings. *Prog. Org. Coat.* **2021,** *151*, 106046.
99. Moorthy, M. S.; Hoang, G.; Subramanian, B.; Bui, N. Q.; Panchanathan, M.; Mondal, S.; Tuong, V. P. T.; Kim, H.; Oh, J., Prussian Blue decorated mesoporous silica hybrid nanocarriers for photoacoustic imaging-guided synergistic chemo-photothermal combination therapy. *J. Mat. Chem. B* **2018,** *6* (32), 5220-5233.
100. Abdalla, A. M. E.; Xiao, L.; Ouyang, C. X.; Yang, G., Engineered nanoparticles: thrombotic events in cancer. *Nanoscale* **2014,** *6* (23), 14141-14152.
101. Li, C. W.; Li, L. L.; Chen, S.; Zhang, J. X.; Lu, W. L., Antioxidant nanotherapies for the treatment of inflammatory diseases. *Front. Bioeng. Biotechnol.* **2020,** *8*.
102. Damodaran, V. B.; Bhatnagar, D.; Leszczak, V.; Popat, K. C., Titania nanostructures: a biomedical perspective. *RSC Adv.* **2015,** *5* (47), 37149-37171.
103. McNamara, K.; Tofail, S. A. M., Nanoparticles in biomedical applications. *Adv. Phys.-X* **2017,** *2* (1), 54-88.
104. Zhou, W. J.; Liu, X. J.; Sang, Y. H.; Zhao, Z. H.; Zhou, K.; Liu, H.; Chen, S. W., Enhanced performance of layered titanate nanowire-based supercapacitor electrodes by nickel ion exchange. *ACS Appl. Mater. Interfaces* **2014,** *6* (6), 4578-4586.
105. Brenneisen, P.; Reichert, A. S., Nanotherapy and reactive oxygen species (ROS) in cancer: A novel perspective. *Antioxidants* **2018,** *7* (2), 31.
106. Israelachvili, J., *Intermolecular and surface forces*. 3 ed.; Academic Press: London, 2011.
107. Bevan, M. A.; Prieve, D. C., Direct measurement of retarded van der Waals attraction. *Langmuir* **1999,** *15* (23), 7925-7936.
108. Evans, D. F.; Wennerstrom, H., *The colloidal domain*. John Wiley: New York, 1999.
109. Liang, Y.; Hilal, N.; Langston, P.; Starov, V., Interaction forces between colloidal particles in liquid: Theory and experiment. *Adv. Colloid Interface Sci.* **2007,** *134-35*, 151-166.
110. Russel, W. B.; Saville, D. A.; Schowalter, W. R., *Colloidal dispersions*. Cambridge University Press: Cambridge, 1989.
111. Bergstrom, L., Hamaker constants of inorganic materials. *Adv. Colloid Interface Sci.* **1997,** *70*, 125-169.
112. Parks, G. A., The isoelectric points of solid oxides, solid hydroxides, and aqueous hydroxo complex systems. *Chem. Rev.* **1965,** *65* (2), 177-198.
113. Tombacz, E.; Libor, Z.; Illes, E.; Majzik, A.; Klumpp, E., The role of reactive surface sites and complexation by humic acids in the interaction of clay mineral and iron oxide particles. *Org. Geochem.* **2004,** *35* (3), 257-267.
114. Delgado, A. V.; Gonzalez-Caballero, F.; Hunter, R. J.; Koopal, L. K.; Lyklema, J., Measurement and interpretation of electrokinetic phenomena. *J. Colloid Interface Sci.* **2007,** *309* (2), 194-224.
115. Trefalt, G.; Szilagyi, I.; Borkovec, M., Poisson-Boltzmann description of interaction forces and aggregation rates involving charged colloidal particles in asymmetric electrolytes. *J. Colloid Interface Sci.* **2013,** *406*, 111-120.
116. Trefalt, G.; Behrens, S. H.; Borkovec, M., Charge regulation in the electrical double layer: Ion adsorption and surface interactions. *Langmuir* **2016,** *32* (2), 380-400.
117. Fritz, G.; Schadler, V.; Willenbacher, N.; Wagner, N. J., Electrosteric stabilization of colloidal dispersions. *Langmuir* **2002,** *18* (16), 6381-6390.
118. Gebbie, M. A.; Valtiner, M.; Banquy, X.; Fox, E. T.; Henderson, W. A.; Israelachvili,

J. N., Ionic liquids behave as dilute electrolyte solutions. *Proc. Natl. Acad. Sci. U. S. A.* **2013,** *110* (24), 9674-9679.

119. Pavlovic, M.; Adok-Sipiczki, M.; Horvath, E.; Szabo, T.; Forro, L.; Szilagyi, I., Dendrimer-stabilized titanate nanowire dispersions as potential nanocarriers. *J. Phys. Chem. C* **2015,** *119* (44), 24919-24926.
120. Rouster, P.; Pavlovic, M.; Horvath, E.; Forro, L.; Dey, S. K.; Szilagyi, I., Influence of protamine functionalization on the colloidal stability of 1D and 2D titanium oxide nanostructures. *Langmuir* **2017,** *33* (38), 9750-9758.
121. Bolto, B.; Gregory, J., Organic polyelectrolytes in water treatment. *Water Res.* **2007,** *41* (11), 2301-2324.
122. Kim, J.; Ryu, J.; Shin, J.; Lee, H.; Kim, I. S.; Sohn, D., Interactions between halloysite nanotubes and poly(styrene sulfonate) in solution. *Bull. Korean Chem. Soc.* **2017,** *38* (1), 107-111.
123. Szilagyi, I.; Trefalt, G.; Tiraferri, A.; Maroni, P.; Borkovec, M., Polyelectrolyte adsorption, interparticle forces, and colloidal aggregation. *Soft Matter* **2014,** *10* (15), 2479-2502.
124. Ruiz-Cabello, F. J. M.; Trefalt, G.; Oncsik, T.; Szilagyi, I.; Maroni, P.; Borkovec, M., Interaction forces and aggregation rates of colloidal latex particles in the presence of monovalent counterions. *J. Phys. Chem. B* **2015,** *119* (25), 8184-8193.
125. Diao, Y. J.; Han, M. W.; Lopez-Berganza, J. A.; Valentino, L.; Marinas, B.; Espinosa-Marzal, R. M., Reconciling DLVO and non-DLVO forces and their implications for ion rejection by a polyamide membrane. *Langmuir* **2017,** *33* (36), 8982-8992.
126. Leikin, S.; Parsegian, V. A.; Rau, D. C.; Rand, R. P., Hydration forces. *Annu. Rev. Phys. Chem.* **1993,** *44*, 369-395.
127. Israelachvili, J. N.; Pashley, R. M., Measurement of the hydrophobic interaction between 2 hydrophobic surfaces in aqueous-electrolyte solutions. *J. Colloid Interface Sci.* **1984,** *98* (2), 500-514.
128. Derjaguin, B.; Landau, L. D., Theory of the stability of strongly charged lyophobic sols and of the adhesion of strongly charged particles in solutions of electrolytes. *Acta Phys. Chim.* **1941,** *14* (6), 633-662.
129. Verwey, E. J. W.; Overbeek, J. T. G., *Theory of stability of lyophobic colloids*. Elsevier: Amsterdam, 1948.
130. Hierrezuelo, J.; Sadeghpour, A.; Szilagyi, I.; Vaccaro, A.; Borkovec, M., Electrostatic stabilization of charged colloidal particles with adsorbed polyelectrolytes of opposite charge. *Langmuir* **2010,** *26* (19), 15109-15111.
131. Hierrezuelo, J.; Vaccaro, A.; Borkovec, M., Stability of negatively charged latex particles in the presence of a strong cationic polyelectrolyte at elevated ionic strengths. *J. Colloid Interface Sci.* **2010,** *347*, 202-208.
132. Hall, S. B.; Duffield, J. R.; Williams, D. R., A reassessment of the applicability of the DLVO theory as an explanation for the Schulze-Hardy rule for colloid aggregation. *J. Colloid Interface Sci.* **1991,** *143* (2), 411-415.
133. Wu, L.; Liu, L.; Gao, B.; Munoz-Carpena, R.; Zhang, M.; Chen, H.; Zhou, Z. H.; Wang, H., Aggregation kinetics of graphene oxides in aqueous solutions: experiments, mechanisms and modeling. *Langmuir* **2013,** *29* (49), 15174-15181.
134. Cao, T. C.; Borkovec, M.; Trefalt, G., Heteroaggregation and homoaggregation of latex particles in the presence of alkyl sulfate surfactants. *Colloids Interfaces* **2020,** *4* (4), 52.
135. Trefalt, G.; Montes Ruiz-Cabello, F. J.; Borkovec, M., Interaction forces, heteroaggregation and deposition involving charged colloidal particles. *J. Phys. Chem. B* **2014,** *118*, 6346-6355.
136. Liu, W.; Zhao, X.; Cai, Z. Q.; Han, B.; Zhao, D. Y., Aggregation and stabilization of

multiwalled carbon nanotubes in aqueous suspensions: influences of carboxymethyl cellulose, starch and humic acid. *RSC Adv.* **2016,** *6* (71), 67260-67270.

137. Missana, T.; Adell, A., On the applicability of DLVO theory to the prediction of clay colloids stability. *J. Colloid Interface Sci.* **2000,** *230* (1), 150-156.
138. Xu, S. H.; Sun, Z. W., Progress in coagulation rate measurements of colloidal dispersions. *Soft Matter* **2011,** *7* (24), 11298-11308.
139. Holthoff, H.; Egelhaaf, S. U.; Borkovec, M.; Schurtenberger, P.; Sticher, H., Coagulation rate measurements of colloidal particles by simultaneous static and dynamic light scattering. *Langmuir* **1996,** *12* (23), 5541-5549.
140. Gisler, T.; Ball, R. C.; Weitz, D. A., Strain hardening of fractal colloidal gels. *Phys. Rev. Lett.* **1999,** *82*, 1064-1067.
141. Lopez-Lopez, J. M.; Schmitt, A.; Moncho-Jorda, A.; Hidalgo-Alvarez, R., Stability of binary colloids: Kinetic and structural aspects of heteroaggregation processes. *Soft Matter* **2006,** *2* (12), 1025-1042.
142. Gregory, J., Monitoring particle aggregation processes. *Adv. Colloid Interface Sci.* **2009,** *147-48*, 109-123.
143. Elimelech, M.; Gregory, J.; Jia, X.; Williams, R. A., *Particle deposition and aggregation: Measurement, modeling, and simulation*. Butterworth-Heinemann Ltd.: Oxford, 1995.
144. Gambinossi, F.; Mylon, S. E.; Ferri, J. K., Aggregation kinetics and colloidal stability of functionalized nanoparticles. *Adv. Colloid Interface Sci.* **2015,** *222*, 332-349.
145. Zaccone, A.; Wu, H.; Lattuada, M.; Morbidelli, M., Correlation between colloidal stability and surfactant adsorption/association phenomena studied by light scattering. *J. Phys. Chem. B* **2008,** *112* (7), 1976-1986.
146. Sandkuhler, P.; Sefcik, J.; Morbidelli, M., Kinetics of aggregation and gel formation in concentrated polystyrene colloids. *J. Phys. Chem. B* **2004,** *108* (52), 20105-20121.
147. Katana, B.; Takács, D.; Szerlauth, A.; Sáringer, S.; Varga, G.; Jamnik, A.; Bobbink, F. D.; Dyson, P. J.; Szilagyi, I., Aggregation of halloysite nanotubes in the presence of multivalent ions and ionic liquids. *Langmuir* **2021,** *37* (40), 11869-11879.
148. Yu, W. L.; Borkovec, M., Distinguishing heteroaggregation from homoaggregation in mixed binary particle suspensions by multiangle static and dynamic light scattering. *J. Phys. Chem. B* **2002,** *106* (51), 13106-13110.
149. Lopez-Lopez, J. M.; Schmitt, A.; Moncho-Jorda, A.; Hidalgo-Alvarez, R., Electrostatic heteroaggregation regimes in colloidal suspensions. *Adv. Colloid Interface Sci.* **2009,** *147*, 186-204.
150. Boddu, V. M.; Abburi, K.; Talbott, J. L.; Smith, E. D., Removal of hexavalent chromium from wastewater using a new composite chitosan biosorbent. *Environ. Sci. Technol.* **2003,** *37* (19), 4449-4456.
151. da Silva, L. F.; Barbosa, A. D.; de Paula, H. M.; Romualdo, L. L.; Andrade, L. S., Treatment of paint manufacturing wastewater by coagulation/electrochemical methods: Proposals for disposal and/or reuse of treated water. *Water Res.* **2016,** *101*, 467-475.
152. Zubair, M.; Daud, M.; McKay, G.; Shehzad, F.; Al-Harthi, M. A., Recent progress in layered double hydroxides (LDH)-containing hybrids as adsorbents for water remediation. *Appl. Clay Sci.* **2017,** *143*, 279-292.
153. Wang, J.; Xu, F.; Jin, H. Y.; Chen, Y. Q.; Wang, Y., Non-noble metal-based carbon composites in hydrogen evolution reaction: Fundamentals to applications. *Adv. Mater.* **2017,** *29* (14), 1605838.
154. Siedl, N.; Baumann, S. O.; Elser, M. J.; Diwald, O., Particle networks from powder mixtures: Generation of TiO_2-SnO_2 heterojunctions via surface charge-induced heteroaggregation. *J. Phys. Chem. C* **2012,** *116* (43), 22967-22973.

155. Patil, A. J.; Mann, S., Self-assembly of bio-inorganic nanohybrids using organoclay building blocks. *J. Mater. Chem.* **2008,** *18* (39), 4605-4615.

156. Wang, H. T.; Adeleye, A. S.; Huang, Y. X.; Li, F. T.; Keller, A. A., Heteroaggregation of nanoparticles with biocolloids and geocolloids. *Adv. Colloid Interface Sci.* **2015,** *226*, 24-36.

157. Parsai, T.; Kumar, A., Understanding effect of solution chemistry on heteroaggregation of zinc oxide and copper oxide nanoparticles. *Chemosphere* **2019,** *235*, 457-469.

158. Cerbelaud, A.; Videcoq, A.; Pagnoux, C.; Rossignol, F.; Ferrando, R., Heteroaggregation between Al_2O_3 submicrometer particles and SiO_2 nanoparticles: Experiment and simulation. *Langmuir* **2008,** *24* (7), 3001-3008.

159. Cao, T. C.; Sugimoto, T.; Szilagyi, I.; Trefalt, G.; Borkovec, M., Heteroaggregation of oppositely charged particles in the presence of multivalent ions. *Phys. Chem. Chem. Phys.* **2017,** *19* (23), 15160-15171.

160. Lin, W.; Kobayashi, M.; Skarba, M.; Mu, C.; Galletto, P.; Borkovec, M., Heteroaggregation in binary mixtures of oppositely charged colloidal particles. *Langmuir* **2006,** *22* (3), 1038-1047.

161. Varenne, F.; Coty, J. B.; Botton, J.; Legrand, F. X.; Hillaireau, H.; Barratt, G.; Vauthier, C., Evaluation of zeta potential of nanomaterials by electrophoretic light scattering: Fast field reversal versus Slow field reversal modes. *Talanta* **2019,** *205*, 120062.

162. Zhang, W. M.; Ma, D.; Du, J. X., Prussian Blue nanoparticles as peroxidase mimetics for sensitive colorimetric detection of hydrogen peroxide and glucose. *Talanta* **2014,** *120*, 362-367.

163. Singh, N.; Savanur, M. A.; Srivastava, S.; D'Silva, P.; Mugesh, G., A redox modulatory Mn_3O_4 nanozyme with multi-enzyme activity provides efficient cytoprotection to human cells in a Parkinson's disease model. *Angew. Chem.-Int. Edit.* **2017,** *56* (45), 14267-14271.

164. Caputo, F.; Mameli, M.; Sienkiewicz, A.; Licoccia, S.; Stellacci, F.; Ghibelli, L.; Traversa, E., A novel synthetic approach of cerium oxide nanoparticles with improved biomedical activity. *Sci Rep* **2017,** *7*, 4636.

165. Du, X.; He, J. H., Facile size-controllable syntheses of highly monodisperse polystyrene nano- and microspheres by polyvinylpyrrolidone-mediated emulsifier-free emulsion polymerization. *J. Appl. Polym. Sci.* **2008,** *108* (3), 1755-1760.

166. Trefalt, G.; Szilagyi, I.; Oncsik, T.; Sadeghpour, A.; Borkovec, M., Probing colloidal particle aggregation by light scattering. *Chimia* **2013,** *67* (11), 772-776.

167. Beaucham, C.; Fridovich, I., Superoxide dismutase - improved assays and an assay applicable to acrylamide gels. *Anal. Biochem.* **1971,** *44* (1), 276-287.

168. Veitch, N. C., Horseradish peroxidase: a modern view of a classic enzyme. *Phytochemistry* **2004,** *65* (3), 249-259.

169. Jiang, B.; Duan, D. M.; Gao, L. Z.; Zhou, M. J.; Fan, K. L.; Tang, Y.; Xi, J. Q.; Bi, Y. H.; Tong, Z.; Gao, G. F.; Xie, N.; Tango, A.; Nie, G. H.; Liang, M. M.; Yan, X. Y., Standardized assays for determining the catalytic activity and kinetics of peroxidase-like nanozymes. *Nat. Protoc.* **2018,** *13* (7), 1506-1520.

170. Maehly, A. C.; Chance, B., The assay of catalases and peroxidases. *Methods Biochem. Anal.* **1954,** *1*, 357-424.

171. Brand-Williams, W.; Cuvelier, M. E.; Berset, C., Use of a free-radical method to evaluate antioxidant activity. *Food Sci. Technol.-Lebensm.-Wiss. Technol.* **1995,** *28* (1), 25-30.

172. Burits, M.; Bucar, F., Antioxidant activity of Nigella sativa essential oil. *Phytother. Res.* **2000,** *14* (5), 323-328.

173. Huang, D. J.; Ou, B. X.; Prior, R. L., The chemistry behind antioxidant capacity assays. *J. Agric. Food Chem.* **2005,** *53* (6), 1841-1856.
174. Zhang, X. Q.; Gong, S. W.; Zhang, Y.; Yang, T.; Wang, C. Y.; Gu, N., Prussian Blue modified iron oxide magnetic nanoparticles and their high peroxidase-like activity. *J. Mater. Chem.* **2010,** *20* (24), 5110-5116.
175. He, X. W.; Tian, L. D.; Qiao, M. T.; Zhang, J. Z.; Geng, W. C.; Zhang, Q. Y., A novel highly crystalline Fe-4(Fe(CN)(6))(3) concave cube anode material for Li-ion batteries with high capacity and long life. *J. Mater. Chem. A* **2019,** *7* (18), 11478-11486.
176. Forment-Aliaga, A.; Weitz, R. T.; Sagar, A. S.; Lee, E. J. H.; Konuma, M.; Burghard, M.; Kern, K., Strong p-type doping of individual carbon nanotubes by Prussian blue functionalization. *Small* **2008,** *4* (10), 1671-1675.
177. Fluck, E.; Inoue, H.; Yanagisawa, S., Mossbauer and X-ray photoelectron spectroscopic studied of Prussian blue and its related compounds. *Z. Anorg. Allg. Chem.* **1977,** *430* (3), 241-249.
178. Biesinger, M. C.; Payne, B. P.; Grosvenor, A. P.; Lau, L. W. M.; Gerson, A. R.; Smart, R. S., Resolving surface chemical states in XPS analysis of first row transition metals, oxides and hydroxides: Cr, Mn, Fe, Co and Ni. *Appl. Surf. Sci.* **2011,** *257* (7), 2717-2730.
179. Ilton, E. S.; Post, J. E.; Heaney, P. J.; Ling, F. T.; Kerisit, S. N., XPS determination of Mn oxidation states in Mn (hydr)oxides. *Appl. Surf. Sci.* **2016,** *366*, 475-485.
180. Li, J. Y.; Wu, X. L.; Zhang, X. H.; Lu, H. Y.; Wang, G.; Guo, J. Z.; Wan, F.; Wang, R. S., Romanechite-structured Na0.31MnO1.9 nanofibers as high-performance cathode material for a sodium-ion battery. *Chem. Commun.* **2015,** *51* (80), 14848-14851.
181. Chen, W.; Yan, Y. Y.; Han, R. L.; Hu, J.; Hou, Y. F.; Tang, K. Q., Biodegradable flower-like manganese for synergistic photothermal and photodynamic therapy applications. *Photochem. Photobiol. Sci.* **2021,** *20* (1), 153-160.
182. Zhou, J. L.; Yu, L.; Sun, M.; Yang, S. Y.; Ye, F.; He, J.; Hao, Z. F., Novel synthesis of birnessite-type MnO_2 nanostructure for water treatment and electrochemical capacitor. *Ind. Eng. Chem. Res.* **2013,** *52* (28), 9586-9593.
183. Bortamuly, R.; Konwar, G.; Boruah, P. K.; Das, M. R.; Mahanta, D.; Saikia, P., CeO_2-PANI-HCl and CeO_2-PANI-PTSA composites: synthesis, characterization, and utilization as supercapacitor electrode materials. *Ionics* **2020,** *26* (11), 5747-5756.
184. Liu, X. B.; Meng, F. M.; Yu, B.; Wu, H., Self-assembly synthesis of flower-like CeO_2/MoS_2 heterojunction with enhancement of visible light photocatalytic activity for methyl orange. *J. Mater. Sci.-Mater. Electron.* **2020,** *31* (9), 6690-6697.
185. Wang, B. Y.; Zhu, B.; Yun, S. N.; Zhang, W.; Xia, C.; Afza, M.; Cai, Y. X.; Liu, Y. Y.; Wang, Y.; Wang, H., Fast ionic conduction in semiconductor CeO_2-delta electrolyte fuel cells. *NPG Asia Mater.* **2019,** *11*, 51.
186. Nottbohm, C. T.; Hess, C., Investigation of ceria by combined Raman, UV-vis and X-ray photoelectron spectroscopy. *Catal. Commun.* **2012,** *22*, 39-42.
187. Ovari, L.; Calderon, S. K.; Lykhach, Y.; Libuda, J.; Erdohelyi, A.; Papp, C.; Kiss, J.; Steinruck, H. P., Near ambient pressure XPS investigation of the interaction of ethanol with Co/CeO_2(111). *J. Catal.* **2013,** *307*, 132-139.
188. Goharshadi, E. K.; Samiee, S.; Nancarrow, P., Fabrication of cerium oxide nanoparticles: Characterization and optical properties. *J. Colloid Interface Sci.* **2011,** *356* (2), 473-480.
189. Spanier, J. E.; Robinson, R. D.; Zheng, F.; Chan, S. W.; Herman, I. P., Size-dependent properties of CeO_2-y nanoparticles as studied by Raman scattering. *Phys. Rev. B* **2001,** *64* (24), 245407.
190. Runowski, M.; Stopikowska, N.; Lis, S., UV-Vis-NIR absorption spectra of lanthanide oxides and fluorides. *Dalton Trans.* **2020,** *49* (7), 2129-2137.

191. Ji, P. F.; Zhang, J. L.; Chen, F.; Anpo, M., Ordered mesoporous CeO_2 synthesized by nanocasting from cubic Ia3d mesoporous MCM-48 silica: Formation, characterization and photocatalytic activity. *J. Phys. Chem. C* **2008,** *112* (46), 17809-17813.
192. Alsharif, N. B.; Samu, G. F.; Saringer, S.; Szerlauth, A.; Takacs, D.; Hornok, V.; Dékány, I.; Szilagyi, I., Antioxidant colloids via heteroaggregation of cerium oxide nanoparticles and latex beads. *Colloid Surf. B* **2022,** *216*, 112531.
193. Alsharif, N. B.; Bere, K.; Sáringer, S.; Samu, G. F.; Takács, D.; Hornok, V.; Szilagyi, I., Design of hybrid biocatalysts by controlled heteroaggregation of manganese oxide and sulfate latex particles to combat reactive oxygen species. *J. Mat. Chem. B* **2021,** *9* (24), 4929-4940.
194. Sadeghpour, A.; Seyrek, E.; Szilagyi, I.; Hierrezuelo, J.; Borkovec, M., Influence of the degree of ionization and molecular mass of weak polyelectrolytes on charging and stability behavior of oppositely charged colloidal particles. *Langmuir* **2011,** *27* (15), 9270-9276.
195. Fuchs, A.; Killmann, E., Adsorption of polyelectrolytes on colloidal latex particles, electrostatic interactions and stability behaviour. *Colloid Polym. Sci.* **1998,** *279* (1), 53-60.
196. Kolman, K.; Nechyporchuk, O.; Persson, M.; Holmberg, K.; Bordes, R., Preparation of silica/polyelectrolyte complexes for textile strengthening applied to painting canvas restoration. *Colloid Surf. A* **2017,** *532*, 420-427.
197. Bauer, D.; Killmann, E.; Jaeger, W., Flocculation and stabilization of colloidal silica by the adsorption of poly-diallyl-dimethyl-ammoniumchloride (PDADMAC) and of copolymers of DADMAC with N-methyl-N-vinyl acetamide (NMVA). *Colloid Polym. Sci.* **1998,** *276* (8), 698-708.
198. Saringer, S.; Rouster, P.; Szilagyi, I., Regulation of the stability of titania nanosheet dispersions with oppositely and like-charged polyelectrolytes. *Langmuir* **2019,** *35* (14), 4986-4994.
199. Rouster, P.; Pavlovic, M.; Szilagyi, I., Immobilization of Superoxide Dismutase on polyelectrolyte functionalized titania nanosheets. *ChemBiochem* **2018,** *19* (4), 404-410.
200. Somosi, Z.; Pavlovic, M.; Palinko, I.; Szilagyi, I., Effect of polyelectrolyte mono- and bilayer formation on the colloidal stability of layered double hydroxide nanoparticles. *Nanomaterials* **2018,** *8* (12), 986.
201. Seyrek, E.; Hierrezuelo, J.; Sadeghpour, A.; Szilagyi, I.; Borkovec, M., Molecular mass dependence of adsorbed amount and hydrodynamic thickness of polyelectrolyte layers. *Phys. Chem. Chem. Phys.* **2011,** *13* (28), 12716-12719.
202. Bridges, T. E.; Houlne, M. P.; Harris, J. M., Spatially resolved analysis of small particles by confocal Raman microscopy: Depth profiling and optical trapping. *Anal. Chem.* **2004,** *76* (3), 576-584.
203. Park, S. H.; Wei, S.; Mizaikoff, B.; Taylor, A. E.; Favero, C.; Huang, C. H., Degradation of amine-based water treatment polymers during chloramination as N-nitrosodimethylamine (NDMA) precursors. *Environ. Sci. Technol.* **2009,** *43* (5), 1360-1366.
204. Pavlovic, M.; Rouster, P.; Szilagyi, I., Synthesis and formulation of functional bionanomaterials with superoxide dismutase activity. *Nanoscale* **2017,** *9* (1), 369-379.
205. Zhang, Y.; Chen, L. X.; Sun, R. M.; Lv, R. J.; Du, T.; Li, Y. H.; Zhang, X. M.; Sheng, R. T.; Qi, Y. F., Multienzymatic antioxidant activity of manganese-based nanoparticles for protection against oxidative cell damage. *ACS Biomater. Sci. Eng.* **2022,** *8* (2), 638-648.
206. Pavlovic, M.; Rouster, P.; Somosi, Z.; Szilagyi, I., Horseradish peroxidase-nanoclay hybrid particles of high functional and colloidal stability. *J. Colloid Interface Sci.* **2018,**

524, 114-121.

207. Chen, C.; Wang, Y.; Yang, Z. Q.; Zhang, D., Layered double hydroxide derived ultrathin 2D Ni-V mixed metal oxide as a robust peroxidase mimic. *Chem. Eng. J.* **2019,** *369*, 161-169.
208. Li, M.; Su, H. Y.; Tu, Y.; Shang, Y. Z.; Liu, Y.; Peng, C. J.; Liu, H. L., Development and application of an efficient medium for chromogenic catalysis of tetramethylbenzidine with horseradish peroxidase. *ACS Omega* **2019,** *4* (3), 5459-5470.
209. Ding, Y. Q.; Wang, G.; Sun, F. Z.; Lin, Y. Q., Heterogeneous nanostructure design based on the epitaxial growth of spongy MoS_x on 2D Co(OH)(2) nanoflakes for triple-enzyme mimetic activity: Experimental and density functional theory studies on the dramatic activation mechanism. *ACS Appl. Mater. Interfaces* **2018,** *10* (38), 32567-32578.
210. Ding, Y. Y.; Sun, L. F.; Jiang, Y. L.; Liu, S. X.; Chen, M. X.; Chen, M. M.; Ding, Y. N.; Liu, Q. Y., A facile strategy for the preparation of ZnS nanoparticles deposited on montmorillonite and their higher catalytic activity for rapidly colorimetric detection of H2O2. *Mater. Sci. Eng. C-Mater. Biol. Appl.* **2016,** *67*, 188-194.
211. Chen, L. J.; Sun, K. F.; Li, P. P.; Fan, X. Z.; Sun, J. C.; Ai, S. Y., DNA-enhanced peroxidase-like activity of layered double hydroxide nanosheets and applications in H_2O_2 and glucose sensing. *Nanoscale* **2013,** *5* (22), 10982-10988.
212. Wu, K. L.; Yang, B. C.; Zhu, X. X.; Chen, W.; Luo, X. L.; Liu, Z. X.; Zhang, X.; Liu, Q. Y., Cobalt and nickel bimetallic sulfide nanoparticles immobilized on montmorillonite demonstrating peroxidase-like activity for H_2O_2 detection. *New J. Chem.* **2018,** *42* (23), 18749-18758.
213. Zhang, Y.; Wang, Y. N.; Sun, X. T.; Chen, L.; Xu, Z. R., Boron nitride nanosheet/CuS nanocomposites as mimetic peroxidase for sensitive colorimetric detection of cholesterol. *Sens. Actuator B-Chem.* **2017,** *246*, 118-126.
214. Tian, R.; Sun, J. H.; Qi, Y. F.; Zhang, B. Y.; Guo, S. L.; Zhao, M. M., Influence of VO_2 Nanoparticle Morphology on the Colorimetric Assay of H_2O_2 and Glucose. *Nanomaterials* **2017,** *7* (11), 347.
215. Liu, Q. Y.; Ding, Y. Y.; Yang, Y. T.; Zhang, L. Y.; Sun, L. F.; Chen, P. P.; Gao, C., Enhanced peroxidase-like activity of porphyrin functionalized ceria nanorods for sensitive and selective colorimetric detection of glucose. *Mater. Sci. Eng. C-Mater. Biol. Appl.* **2016,** *59*, 445-453.
216. Dincer, A.; Aydemir, T., Purification and characterization of catalase from chard (Beta vulgaris var. cicla). *J. Enzym. Inhib.* **2001,** *16* (2), 165-175.
217. Marin, E.; Tapeinos, C.; Lauciello, S.; Ciofani, G.; Sarasua, J. R.; Larranaga, A., Encapsulation of manganese dioxide nanoparticles into layer-by-layer polymer capsules for the fabrication of antioxidant microreactors. *Mater. Sci. Eng. C-Mater. Biol. Appl.* **2020,** *117*, 111349.
218. Bhagat, S.; Vallabani, N. V. S.; Shutthanandan, V.; Bowden, M.; Karakoti, A. S.; Singh, S., Gold core/ceria shell-based redox active nanozyme mimicking the biological multienzyme complex phenomenon. *J. Colloid Interface Sci.* **2018,** *513*, 831-842.
219. Wu, H.; Liang, Y. P.; Shi, J. F.; Wang, X. L.; Yang, D.; Jiang, Z. Y., Enhanced stability of catalase covalently immobilized on functionalized titania submicrospheres. *Mater. Sci. Eng. C-Mater. Biol. Appl.* **2013,** *33* (3), 1438-1445.
220. Liu, C.; Yan, Y. Y.; Zhang, X. W.; Mao, Y. Y.; Ren, X. Q.; Hu, C. Y.; He, W. W.; Yin, J. J., Regulating the pro- and anti-oxidant capabilities of bimetallic nanozymes for the detection of Fe^{2+} and protection of Monascus pigments. *Nanoscale* **2020,** *12* (5), 3068-3075.
221. Olivera, S.; Hu, C.; Nagananda, G. S.; Reddy, N.; Venkatesh, K.; Muralidhara, H. B.,

Multipurpose composite for heavy metal sorption, antimicrobial, and antioxidant applications. *Int. J. Environ. Sci. Technol.* **2019,** *16* (4), 2017-2030.

222. Mao, Y. Y.; Jia, F. M.; Jing, T. Y.; Li, T. T.; Jia, H. M.; He, W. W., Enhanced multiple enzymelike activity of PtPdCu trimetallic nanostructures for detection of Fe^{2+} and evaluation of antioxidant capability. *ACS Sustain. Chem. Eng.* **2021,** *9* (1), 569-579.
223. Berne, B. J.; Pecora, R., *Dynamic light scattering*. Robert E. Krieger Publishing: Malabar, 1990.
224. Jonasz, M.; Fournier, G. R., *Light scattering by particles in water*. 1 ed.; Elsevier Inc.: Oxford, 2007.
225. Schärtl, W., *Light scattering from polymer solutions and nanoparticle dispersions*. Springer: Berlin, 2007.
226. Deshiikan, S. R.; Papadopoulos, K. D., Modified Booth equation for the calculation of zeta potential. *Colloid Polym. Sci.* **1998,** *276* (2), 117-124.

10 Supplementary Information

Appendix A: Michaelis-Menten model of enzyme kinetics

Experimental studies on enzyme kinetics revealed several key observations

1. The initial rate of product formation, $v_{o,}$ is proportional to the total enzyme concentration, $[E]_o$, at a certain initial substrate concentration, $[S]_o$.
2. For a given $[E]_o$, v_o is proportional to $[S]_o$ (at low $[S]_o$) and independent of $[S]_o$ (at high $[S]_o$).

Two approaches are utilized to derive the rate expression that accounts for these observations: i) Thermodynamic equilibrium and ii) steady-state approximation. In 1913, the German biochemist Leonor Michaelis (1875–1949) and the Canadian biochemist Maud L. Menten (1879–1960) proposed a mechanism that accounts for these observations. Accordingly, the binding of the substrate, S, to the enzyme, E, forms the enzyme-substrate complex, ES, that can separate back into substrate and enzyme or proceed into the product, P, formation:

$$E + S \overset{k_1/k_{-1}}{\longleftrightarrow} ES \overset{k_2}{\rightarrow} P + E \tag{41}$$

where k_1 and k_{-1} are the rate constants for the formation of ES and its dissociation into S and E, respectively, and k_2 is the rate constant of the product formation reaction. The product formation proceeds with the following initial rate:

$$v_0 = \left(\frac{d[P]}{dt}\right)_0 = k_2[ES] \tag{42}$$

THERMODYNAMIC EQUILIBRIUM: Since [ES] is not measurable, Michaelis and Menten assumed that that $k_{-1} \gg k_2$ and that the ES formation is a rapid equilibrium process, where ES is in thermodynamic equilibrium with the substrate and enzyme.

$$K_S = \frac{k_{-1}}{k_1} = \frac{[E][S]}{[ES]} \tag{43}$$

In addition, at any time the total enzyme concentration $[E]_o$ is the sum of [ES] and the enzyme concentration, [E], and thus:

$$[E] = [E]_o - [ES] \tag{44}$$

Thus, by inserting the expression of [E] in the equilibrium constant, and solving for [ES]

$$[ES] = \frac{[E]_o[S]}{K_S + [S]} \tag{45}$$

And thus, the expression of the initial reaction rate becomes

$$v_0 = \left(\frac{d[P]}{dt}\right)_0 = \frac{k_2[E]_0[S]}{K_S + [S]} \tag{46}$$

From which,

$$v_0 = \frac{k_2}{K_S}[E]_0[S] \qquad \text{at low } [\mathrm{S}]_0 \text{ when } ([\mathrm{S}] \ll K_S)$$

$$v_0 = k_2[E]_0 \quad \text{at high } [\mathrm{S}]_0 \text{ when } ([\mathrm{S}] \gg K_S)$$

When all the enzyme molecules are bound with the substrate as ES, the measured initial rate reaches its maximum possible value, $v_{\max}$, which represents the maximum possible reaction rate, where the total enzyme concentration equals that of the enzyme-substrate complex.

$$v_{max} = k_2[E]_0 \tag{47}$$

STEADY-STATE APPROXIMATION: In 1925, British biologists George Briggs (1893–1978) and John Haldane (1892–1964), alternatively used steady-state approximation to obtain the initial rate. According to the approach, it is unnecessary to assume that the enzyme and substrate are in thermodynamic equilibrium with the enzyme-substrate complex to obtain the rate expression. Rather, the concentration of the enzyme-substrate complex will reach a constant value soon after the enzyme and substrate are mixed.

$$\frac{d[ES]}{dt} = k_1[E][S] - k_{-1}[ES] - k_2[ES] = 0 \tag{48}$$

From which

$$[ES] = \frac{k_1[E]_o[S]}{k_1[S] + k_{-1} + k_2} \tag{49}$$

$$v_0 = \left(\frac{d[P]}{dt}\right)_0 = \frac{k_2 k_1[E]_o[S]}{k_1[S] + k_{-1} + k_2} \tag{50}$$

$$= \frac{k_2[E]_o[S]}{K_m + [S]} \tag{51}$$

If $v_{max} = k_2[E]_0$ and $K_m = \frac{k_{-1}+k_2}{k_1}$, the *Michalis-Menten equation* is obtained.

$$v_0 = \frac{v_{max}[S]}{K_m + [S]} \tag{52}$$

where v_{max} represents the maximum possible reaction rate and K_{m} is the Michaelis constant and represents the [S] at which the initial rate is half that of v_{max}. Comparing the results of both approaches, both expressions have a similar dependence on substrate concentration. K_{m} *and* K_{S} are equal only when $k_{-1} \gg k_2$. In addition, both approaches have the exact definition of the maximum rate.

Appendix B: Theoretical background of light scattering techniques

Dynamic light scattering (DLS): The DLS is an instrumental technique for the determination of particle size as well as the particle size distribution, and thus, provides an insight into the stability of colloidal systems. The DLS technique involves irradiating the sample with a monochromatic source of light, e.g., a laser, and detecting the pattern of fluctuations in the intensity of scattered light at a certain angle upon interacting with the sample. These fluctuations occur due to the Brownian motion, and the velocity of particles can be related to the particle size, namely, the hydrodynamic radius, R_h, by the Stokes-Einstein equation:[223]

$$R_h = \frac{k_B T}{6\pi\eta D} \tag{53}$$

where η is the viscosity of the medium, T is the absolute temperature, k_B is the Boltzmann constant, and D is the translational diffusion coefficient, the Stokes-Einstein equation shows that R_h is readily available once D is determined. Autocorrelation of the scattered intensity is an approach used to generate the *correlation function*, which can be expressed as:[224, 225]

$$g^2(q,\tau) = \frac{\langle I(t)I(t+\tau)\rangle}{\langle I(t)\rangle^2} \tag{54}$$

where $I(t)$ is the scattered light intensity at time t, and $I(t+\tau)$ is the intensity shifted by a delay time τ. The Siegert relation:

$$g^2(q,\tau) = A[1 + \beta e^{-2\Gamma\tau}] \tag{55}$$

where A is the baseline, β is the coherence factor, and Γ is the decay rate. The diffusion coefficient can be obtained as follows:

$$D = \frac{\Gamma}{q^2} \tag{56}$$

where q is the scattering vector and can be obtained as follows:

$$q = \frac{4\pi n}{\lambda} sin\left(\frac{\theta}{2}\right) \tag{57}$$

here, n is the medium's refractive index, λ is the wavelength of the monochromatic light source, and θ is the angle at which the scattered light is collected. Once q and Γ are obtained, the Stokes-Einstein relation is used to obtain the R_h.

Electrophoretic light scattering (ELS): The ELS combines DLS and electrophoresis to obtain the electrophoretic mobility, and thus the zeta potential, of colloidal particles (under the influence of external electric field) using frequency shift or phase shift analysis of an incident laser beam.[161] The electrophoretic mobility, μ, of charged particles moving under the influence of an external electric field, E, is related to their velocity, υ, as follows:

$$\mu = \frac{\upsilon}{E} \tag{58}$$

The electrokinetic or zeta potential, ζ, is obtained from μ from various models and depends on the experimental conditions such as the medium's dynamic viscosity, η, the ionic strength (expressed in the Debye parameter, κ), and radius of the particles, R. When $\kappa R > 20$, the *Helmholtz-Smoluchowski* model is used to obtain the zeta potential:

$$\zeta = \frac{u\eta}{\varepsilon_0 \varepsilon} \tag{59}$$

When $\kappa R < 1$, the zeta potential is given by the *Hückel* model:

$$\zeta = \frac{2u\eta}{3\varepsilon_0 \varepsilon} \tag{60}$$

When $1 < \kappa R < 20$, the zeta potential is obtained using the *Henry* model:

$$\zeta = \frac{2u\eta}{3\varepsilon_0 \varepsilon} f(\kappa R) \tag{61}$$

where the value of $f(\kappa R)$ falls within 1-1.5 range.[226] A comparison of these models is shown in **Figure S1**.

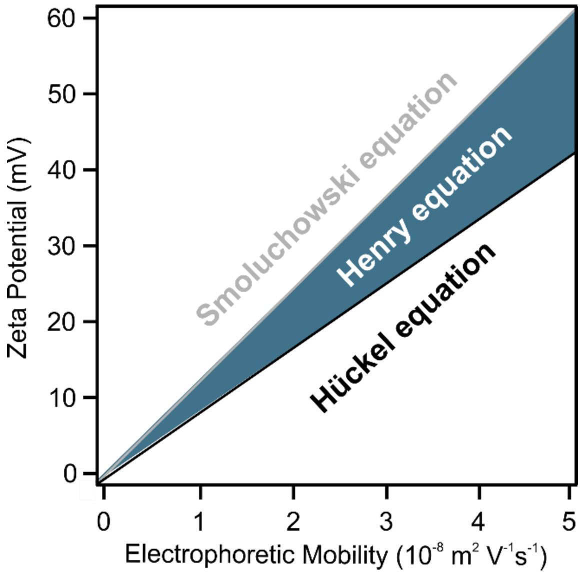

Figure S1. The Helmholtz-Smoluchowski, Hückel, and Henry models for the calculation of the zeta potential from the electrophoretic mobility.

Appendix C: Experimental determination of CCC values.

The CCC values can be estimated from measurements of stability ratio, W, as a function of the ionic strength, $c_{electrolyte}$:

1. **Estimation of the $\boldsymbol{\beta}$ value**: Using the *experimentally measured* W values (W_{exp}) at various $c_{electrolyte}$, the β value can be obtained by plotting $log(1/W_{exp})$ as a function of log($c_{electrolyte}$) for the salt concentrations at the slow aggregation regime, where β is the slope of the resulting linear graph, as shown in the following expression, Equation (37):

$$dlog(\frac{1}{W_{exp}}) = \beta dlogc_{electrolyte}$$

2. **Estimation of initially calculated $\boldsymbol{W}$ values** (W_{calc}): Since the CCC is the salt concentration at which the colloidal system transit into the rapid aggregation regime, the following expression (Equation (36)) is used to obtain W_{calc} at the corresponding $c_{electrolyte}$, using the estimated CCC, taken from the W-$c_{electrolyte}$ graph, as well as the β, obtained in step (1).

$$W_{calc} = 1 + \left[\frac{CCC}{c_{electrolyte}}\right]^{\beta}$$

3. **Estimation of $\boldsymbol{CCC}$:** The sum of the squared differences between W_{calc} and W_{exp} is used to obtain the best value for CCC using Excel's solver to find the best fit to minimize the squared difference

Appendix D: Raman and XPS compositional analysis data

Table S1: XPS composition analysis of PB NPs.

Region	**Peak species**	**Peak (at%)**[a]	**Sample (at%)**[b]
C 1s	C–C	69±2	36.0
	C–OH, CN	20±1	11.0
	C=O	7±1	4.0
	O–C=O	4±1	2.0
N 1s	CN	65±2	20
	Charge transfer	22±2	6.8
	Ammonium ion	13±2	4.01
Fe 2p	Fe(II)	87±7	3.7
	Fe(III)	13±2	0.6
O 1s	Surface –OH	11.7	11.7

[a] Atomic percentage (at%) unit is the number-based composition ratio, i.e., based on the number of atoms. The Peak (at%) is the atomic percentage of a constituent species in its deconvoluted peak. For a given region, the sum of Peak (at%) for all constituent species is 100%. [b] Sample (at%) is the atomic percentage of the species in the whole sample. The sum of Sample (at%) for all species is 100%.

Table S2: The binding energies of all transitions in the Ce 3d region of the XPS survey spectrum of the CeO_2 NPs.

Surface species	**Transition**	**Binding Energy (eV)**	**Reference value (eV)**
Ce (IV)	v	882.8	882.3
	v”	888.8	888.8
	v”’	898.7	898.2
	u	901.1	900.7
	u”	907.7	907.5
	u”’	917.0	916.6
Ce (III)	v^0	880.8	880.7
	v’	885.2	885.2
	u^0	899.4	899.3
	u’	903.5	903.8

Table S3: The Raman shift values and the corresponding vibrational mode of recorded Raman peaks of CeO_2 NPs, SL, PDADMAC, SL-CeO_2, and SPCe.

Raman shift (cm^{-1})	**Assignment**	**Sample**
462	n_{sym}(Ce-O)	CeO_2, SL-CeO_2, SPCe
573	d(C-C)	PDADMAC
620	d(ring)	CeO_2, SL, SL-CeO_2, SPCe
790	n(N-C)	PDADMAC
795	n(C-H)	SL, SL-CeO_2, SPCe
1000	d(ring)	
1032	n(C-H)	
1150-1200	n(C-C)	
1584	n(C=C)	
1602	n(ring)	
1449	d(CH_3)	PDADMAC